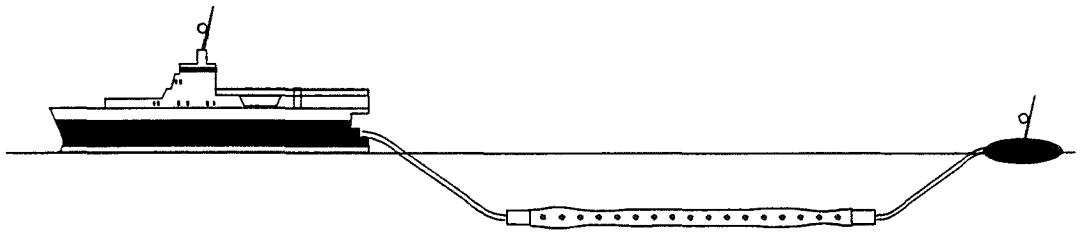

REDUCTION OF NOISE IN SEISMIC HYDROPHONE ARRAYS

MODELLING OF BREATHING WAVES AND

ADAPTIVE NOISE CANCELLING

By
Cato Bjelland

Dr.scient. thesis
University of Bergen

Final Report
Nordic Industrial Research Education NIFU-31

Preface

This report is the thesis for the Dr.Scient. degree at the University of Bergen. It is also the final report in the Nordic Industrial Research Education NIFU-31.

The work has been carried out in cooperation with Geco-Prakla/Fjord Instruments, Technical University of Denmark and University of Bergen.

I would like to thank my supervisors and project steering committee for their support:
Prof.Dr.Leif Bjørnø Technical at University of Denmark
Prof.Dr.Halvor Hobæk at University of Bergen
Siv.ing.Jan Åge Langeland at Geco-Prakla/Fjord Instruments

I would also like to thank the people both in manufacturing and engineering at Fjord Instruments, that has contributed to this project. The experimental hydrophone array section was built on short notice and shipped down to Denmark for experiments during my one year stay there. The people in administration has also supported the project with accounting and other administrative related sides of the project. The sister company Getech has built a high quality accelerometer module which makes industrial implementation of the result in this project possible. I have also received some interesting data from noise recordings on the Geco-Prakla boats during the project.

During my stay at the Department of Industrial Acoustics at Technical University of Denmark, I benefitted from the many interesting discussions with both members of the Department of Industrial Acoustics and also people in other Departments like Fluid Mechanics and Solid Mechanics. Furthermore, some vital equipment was kindly lent to me by the different departments.

The theoretical part of the Dr.scient/ NIFU-31 program has been done at the University of Bergen. Many special topics have been put together to support the project. I have experienced great flexibility in appointments for the necessary exams during the project.

I wish to thank The Nordic Fund for Technology and Industrial Development (Nordisk Industrifond) for a financial support to the project of DKK 475.000. And the fund secretariat Academy of Technical Science (ATV) for good cooperation during this project.

Finally, I take this opportunity to thank my family for their support and patience during this research education.

Revision: A2
Copy No: 67

26. march, 1993
Cato Bjelland

10.of may, 1993

Some corrections have been implemented in this edition:

1) Ref. section 3.1: The Ultrasonic Method
The complex Young's modulus E^* is replaced with complex plane wave modulus M^* in wave equation. E^* is then found by relation to M^*. The correction has no effect on other results in the report.

2) Ref. equation (5.51)
x_i is replaced by L in the end of the equation. This correction is important, but the effect on the results of modelling are negligible.

3) Ref. equation (5.32)
- replaced with + before second part, R_0^2 replaced with R_0 in the first part.

Correction 1) & 2) is based on comments by Dr.Per Lunde of Christian Michelsen Research in Bergen.

Correction of typing error in 3) pointed out by Prof.Dr.Anders Nilsson of The Royal Technical University (KTH) in Sweden.

CONTENTS

Contents

List of Symbols and Definitions

α = attenuation constant
= cross sectional area in section 3.3
= inverse of boundary layer thickness
= normalized adaption constant in LMS
β = damping factor for global mode in stress members
= factor to control averaging time in recursive power estimate
γ^2 = Coherence
ϵ = performance function (error signal)
η = displacement in chapter 3
= radial displacement in chapter 5.
λ = wavelength
λ_{max} = Largest Eigenvalue
μ = adaption constant in LMS algorithm
= Poisson's ratio
= viscosity in Navier Stokes equation
ν = kinematic viscosity
ξ = axial displacement
= mean squared error in LMS algorithm
π = Estimate of signal power
ρ = density
σ = Poisson's ratio in viscoelastic relation, chapter 5
= stress
τ = time constant
ϕ = Phase angle between real and imaginary part
ω = radial frequency $2\pi f$
a = radius of cylinder
= small numerical value in Normalized LMS
A = Amplitude
c = phase speed
d = depth in chapter 4
= attenuation factor for breathing wave mode
E = Young's modulus
E[] = Expectation
f = frequency
g = gravitation constant 9.8 m/s^2
G = shear modulus
h = thickness
H = Hankel function
I_0 = Modified Bessel function of order zero
J_0 = Bessel function of order zero
k = wavenumber
K = modified Hankel function in section 5.2
= wave number in section 5.1
= bulk modulus

List of Symbols and Definitions

l	= length
m	= mass
M	= Misadjustment
N	= Number of samples
p	= pressure perturbation
$\mathbf{P}$	= Cross correlation matrix
P	= Pressure Amplitude
Q	= Quality factor
$\mathbf{R}$	= Input correlation matrix
R_0	= Radius of tube in chapter 5
t	= time
T	= Temperature
	= Tension in tube wall
$\tan\delta$	= loss factor
u	= strain
V	= Volume
v_c	= Convection speed
v_r	= velocity component in radial direction
v_x	= velocity component in x-direction
$\mathbf{W}_k$	= Weigth vector
$\mathbf{X}_k$	= Signal vector
d_k	= desired response
y_k	= Output signal
z	= Impedance
∇	= Gradient vector

Notation: i) both i and j have been used for the imaginary unit, **ii)** functions of space and frequency (x,ω) is replaced with index (i,n) in Mcad due to matrix representation.

Streamer: Seismic cable consisting of lead-in cable, hydrophone sections and stretch sections.
Leadin: Tow cable from seismic vessel to first section.
Stretch: Elastic section.
Hydrophone section: Long oil-filled tube with hydrophones inside.
Hydrophone: A sensor converting pressure signal to an electrical signal.
H21: Hydrophone number 21 (position of hydrophone).
Accelerometer: A sensor converting acceleration to an electrical signal.
DSP: Digital Signal Processor.
FFT: Fast Fourier Transform.

ATV: Akademiet for de Tekniske Videnskaber (Academy of Technical Science)
NIFU-31: Nordisk Industriforskerutdannelse-31 (Nordic Industrial Research Education)
DTH: Danmarks Tekniske Højskole (Technical University of Denmark)
UiB: Universitetet i Bergen (University of Bergen)
FI: Fjord Instruments A/S (part of Geco-Prakla)

1.0 INTRODUKSJON

I seismisk letevirksomhet til havs mottas pulser fra seismisk kilder (luftkanoner) etter refleksjon fra sedimenter under havbunnen med lange hydrofon array som taues bak et seismisk fartøy. Vanligvis taues to 3 km lange kabler med kontrollerbar separasjon. Den seismiske kabelen omtales ofte som streamer eller hydrofon array.

Det genereres vibrasjoner i kabelen på grunn av tauing og bølge-aktivitet. Vibrasjoner som genereres hovedsaklig i fronten og bak på kabelen, dempes ved hjelp av mekaniske filtre som elastiske seksjoner og masse-elementer. Den seismiske kabelen (streameren) består vanligvis av 100 meter lange oljefyllte seksjoner med hydrofoner innvendig. Et indre skjelett består av strekkavlastere og avstandstykker. Hydrofonene er konfigurert for direktivitet og koblet til plugger i hver ende av seksjonen. Vibrasjoner i strekkavlasterne vekselvirker med pluggene og det oljefyllte skinnet. Det genereres lokale pustebølger som forplanter seg i streameren. Trykkvariasjonen registreres av hydrofonene og kommer i tillegg til det seismiske signalet.

Når streameren taues gjennom vannet oppstår det trykkfluktuasjoner på utsiden av skinnet. Strømningstøyen som registreres av hydrofonene skyldes hovedsaklig to mekanismer: direkte forplanting av trykkfluktuasjon fra det turbulente sjiktet inn til hydrofon og eksitasjon av pustebølger.

Videre kan instrumenter som er festet til streameren som f.eks. dybdekontrollere og kompasser generere turbulens og vibrasjoner.

Denne rapporten omhandler modeller for beskrivelse av støymekanismene, hovedsaklig støy på grunn av pustebølger i streamer seksjonene. Videre blir en metode for adaptiv støykansellering som er utviklet i dette prosjektet beskrevet.

I akustisk design av seismiske streamere er målet å redusere egengenerert støy og værgenerert støy. Dette kan gjøres passivt med konstruksjon og/eller v.h.a. signalbehandling.

Egengenerert støy kan reduseres passivt v.h.a. en konstruksjon som i seg selv er diskriminerende. Det vil si v.h.a. hydrofon arrangement, fysisk overgang til omgivelsene og utvelgelse av materialer i konstruksjonen. Hovedparameterene er: tykkelse av skinn, skinnets viskoelastiske egenskaper, fyllingsmateriale mellom hydrofoner og skinn og hydrofon størrelse.

Hydrofon-posisjon, plassering av oljeblokkering og plugger har innvirkning på støynivået. Dette kan til en hvis grad studeres i teoretiske modeller.

En serie av eksperimenter med segmenter av streamer skinn er utført i dette prosjektet for å finne de dynamisk viskoelastiske egenskapene. Eksperimentene og resultatene er beskrevet i kapittel 3. Bakgrunnsteorien for viskoelastisitet er presentert i kapittel 2.

I kapittel 4 er det tatt med en introduksjon til strømningstøy mekanismen.

En modell for pustebølge moden er beskrevet i kapitel 5. Modellen er basert på grunnleggende kontinuumsmekanikk. Ligninger for bevaring av masse og massefart i væsken er tilpasset til de viskoelastiske relasjonene i streamer skinnet gjennom felles grensebetingelser på innsiden av skinnveggen. Målinger av viskoelastiske egenskaper fra eksperimentene tas inn i denne modellen. Man kommer da frem til en realistisk dispersjon relasjon og en frekvensavhengig dempning for pustebølge moden.

Disse funksjonene brukes deretter i hydrofon array konfigurasjoner for å prediktere overføringsfunksjoner mellom referanse sensorer og hydrofoner i streamer seksjoner. Overføringsfunksjonen kan brukes som et startkriterie i en adaptiv støykansellerings algoritme. Overføringsfunksjonen kan også brukes i hastighets filtre (F-K-filtre).

Den predikterte overføringfunksjonen (fra modell) for pustebølgemoden er sammenlignet med målinger av samme overføringsfunksjon i seismisk seksjon. Eksperimenter med en 12 meter streamer seksjon hengende vertikalt er beskrevet i kapittel 6. Pustebølger genereres v.h.a. en vibrator koblet til den nederste enden av seksjonen og målingene sammenlignes med modell.

Den samme 12 meter seksjonen ble tauet i en 250 meter lang vanntank. I kapitel 7 er det tatt med en del innledende analyse og resultater.

Den adaptive signalbehandlings metoden er basert på måling av et referanse støysignal. Bakgrunnsteorien er beskrevet i kapittel 8. Teorien leder opp til en normalisert LMS algoritme med rekursiv effekt-estimat som brukes i det adaptive støykansellerings systemet. Videre blir lærekurver, signal/støy forhold og forvrengning beskrevet i kapittel 8. Implementering av det adaptive støykansellerings systemet på et digital signal prosessor kort (DSP32C) er beskrevet i kapittel 9.

Eksperimenter med det adaptive støykansellerings systemet er beskrevet i kapittel 10. Systemet er testet for flere tilfeller: 1) Pustebølger generert med vibrator fra enden av 12 meter streamer seksjon. 2) Samme som ovenfor pluss ekstern kilde for å simulere primær signal. 3) Data fra tidligere sjøtester "Stad Girl" og "Rauberg". 4) Støymålinger ved tauing av 12 meter seksjon i lang vanntank.

Konklusjoner fra modeller og eksperimenter er beskrevet i kapittel 11.

1.0 INTRODUCTION

In seismic surveys offshore the pulses from seismic sources are received, after reflection from sediments below the sea-bed, by long hydrophone arrays towed behind a seismic vessel. Usually two 3 km long cables are towed with a controllable separation behind the vessel.

Vibrations are generated in the cable due to towing and wave activity. The vibrations generated in the front of the streamer are reduced by mechanical filters, such as elastic sections and mass elements. The seismic cable (streamer) is made up by 100 meter long sections. The streamer section consists of hydrophones inside an oil-filled skin. Stress-wires and spacers make up the internal skeleton. The hydrophones are configured for directivity, and wired to connectors at each end of the streamer section. Vibrations in the stress-wires are interacting with the connectors and oil-filled skin. Breathing waves are generated and propagates down the streamer. The pressure variation is detected by the hydrophones, and adds to the seismic signal.

When the streamer moves through water, boundary layer turbulence cause pressure fluctuations at the outer skin wall. The flow noise detected by the hydrophones is mainly due to two mechanisms: Direct propagation of pressure fluctuations from turbulent layer and excitation of breathing waves.

Additional instruments clamped onto the cable, like depth controllers and compasses can also cause turbulence and vibrations.

This report includes models for description of noise mechanism, mainly noise due to breathing waves in the streamer sections. A method for adaptive noise cancelling that has been developed in this project will also be described.

In streamer acoustic design, the goal is to reduce the influence of self noise and weather generated noise. This can be done passively by design and/or by signal processing.

The streamer self-noise can be reduced passively by an inherent noise discriminating design. That is by hydrophone arrangement, arrangement of physical interface to the environment and selection of materials in the streamer assembly. The main parameters are: thickness and viscoelastic properties of the streamer skin, filling material between hydrophone and skin, and size of hydrophone.

Hydrophone position, oilblocks and connectors also have an effect on the noise level, which can be studied in theoretical models.

A series of experiments with segments of streamer skin have been done in this project to find the dynamic viscoelastic properties. The experiments and results are presented in chapter 3. Some background theory for viscoelasticity is presented in chapter 2.

Some introduction to the flow noise mechanism is given in chapter 4.

A model for the breathing wave mode in an seismic hydrophone section is presented in chapter 5. The model is based on fundamental continuum mechanics. Equations for mass- and momentum-conservation in the fluid, is matched to the viscoelastic relations in the streamer skin through common boundary conditions on the inside surface of the streamer skin. The viscoelastic properties as a function of frequency from the experiments with real streamer skin is taken into this model. A realistic dispersion relation and frequency dependent damping for the breathing wave mode is then found.

These functions are then used in specific array configurations to predict transfer functions between reference transducer and hydrophones in the streamer section. The transfer function (or impulse response) can be used as the initial guess in an adaptive noise canceling algorithm. The transfer function can also be used in velocity filters (F-K-filters).

The predicted transfer function for the breathing wave mode has been compared with measurements of the same transfer function in seismic sections. The experiments with a 12 meter hydrophone section hanging vertically are described in chapter 6. Breathing waves have been generated by means of a vibrator connected to the lower end of the section, and measurements are compared to modelling.

The same 12 meter section was towed in a 250 meter long water tank. Some initial analysis and results are described in chapter 7.

The adaptive signal processing method is based on measurements of a reference noise signal. The background theory for adaptive noise cancelling is described in chapter 8. The theory leads up to the normalized LMS algorithm with recursive power estimate that has been used in the adaptive noise cancelling system, The learning curve, signal to noise ratio and distortion are also described in chapter 8. The implementation of the adaptive noise cancelling system is described in chapter 9.

Experiments with the adaptive noise cancelling system are described in chapter 10. The system has been tested for different cases: 1) Breathing waves generated by a vibrator from the end of the 12 meter section. 2) Same as above plus an external source to simulate the primary signal. 3) Data recorded during sea test "Stad Girl" and "Rauberg" 4) Noise recorded during towing of 12 meter section in ship tank.

The conclusions on modelling and results of experiments are described in chapter 11.

1.1 PROJECT BACKGROUND

The current project on reduction of acoustic self-noise in seismic streamers is partly based on the results from a major test by Geco in 1986 called the Stad Girl Test ref.[11]. The main purpose of this test was to get detailed knowledge of acoustic noise generation and propagation in towing system and streamers.

A special 75 m long streamer section with single hydrophones was used in this test. The distance between individual hydrophones was 0.5 meter. Normally the hydrophones are grouped (e.g. 12 hydrophones in parallel). The special section decreased the spatial sampling interval and a more detailed picture of the noise was seen. Accelerometers were also used in the streamer. The main purpose at the time was to investigate the connection between vibrations in stress-members (wires) and towing configuration. This was called the global wave propagation in the Stad Girl report. A transmission line model was developed to describe this wave propagation.

The vibrations from the towing system was explained from theory of vortex induced vibrations. The alternating vortex generation results in an alternating flow around the wire, which again results in vibrations of the wire. The oscillation frequency is known from experiments to have a predominant peak at: $f=\alpha v_n/D$.

The Strouhal number: $\alpha=0.2$ for circular cylinder. v_n is the speed component normal to the surface. An oscillation frequency of 3.4 Hz is calculated for a diameter of D=52mm, speed 5 knots and tow angle 20°. The longitudinal vibrations by the front connector will be twice this frequency due to conversion (transversal to longitudinal). Fig.3.24 in the "Stad Girl" report (enclosed in Appendix A1), shows such a noise spectrum with harmonics of the fundamental at 6 Hz.

The Local Wave Propagation is clearly seen in the RMS offset trace-plot of the special section with single hydrophones. This is shown in fig.4.6 and 4.7 in the "Stad Girl" report. From these measurements it was possible to find the propagation speed of the envelope and the attenuation of average rms level with distance. The speed was found to be approximately 30 m/s and the damping coefficient was found to be 0.25 in active sections. Though this is only rough calculations from the speed of the envelope and attenuation in rms level, the measurements have been used for comparison in later modelling.

An attempt to model the local wave propagation in the oil filled streamer section was also made in the Stad Girl report. The sources of these waves were identified to be the connectors. The waves were termed breathing waves. The model was developed from lossless acoustic wave equation and elastic equations.

The local wave model developed in Stad Girl report can not be used to describe the breathing wave mode. Later in this report it will be shown that: the distensibility is more important than compressibility, and the theory must be developed from more fundamental continuum mechanical equations that include losses.

An alternative model was also presented in the Stad Girl report. This was the low frequency, lossless model originally given in "Methods of Theoretical Physics" by Morse & Feshback part II. The expression for propagation speed found from that model is nondispersive. It is identical to the speed found for frequency $\omega=0$ in the new breathing wave model presented in Chapter 5. This was seen to approximately match the speed of the envelope in measurements of local wave propagation in the Stad Girl Test.

In spite of the limitations in the model given in Morse & Feshback, it showed roughly how the speed depends on parameters like: density of oil-filling, thickness of skin, static modulus in skin and radius of section. This was sufficient to start the process of establishing a qualitatively rough picture of the breathing wave mode. There was no model for the attenuation of the breathing wave mode, although the damping coefficient of the envelope was known from measurements. From a noise cancelling point of view, a model including attenuation is of vital importance.

The analysis of the results from the Stad Girl test and further development suffered some due to other priorities and cutdown in seismic activity for some years after the Stad Girl Test. During the recent years the activity on streamer acoustic noise reduction have been increased somewhat. The identification of the sources together with the measured speed and damping was used to arrange positions of sources (connectors) to cancel the noise generated by each other. There are some obvious problems with this, and the research has been continued to develop more detailed models and systems for noise cancelling by signal processing and design.

In 1991 a project was established in cooperation with: Prof.Dr.Halvor Hobæk at the University of Bergen and Prof.Dr.Leif Bjørnø at the Technical University of Denmark. The project is supported by The Nordic Fund for Technology and Industrial Development. The project was established to cover the fundamental problems of modelling and development of a system for noise cancelling, mainly of the breathing wave mode.

2.0 VISCOELASTICITY

In seismic streamer design, viscoelastic materials form an important class of materials. The development of a model for the wave modes in a streamer section, has shown that the viscoelastic behavior of streamer skin is an important factor. The streamer oil can be made viscoelastic by addition polymerization ("Gel-like" filling materials). A brief review of viscoelastic behavior of materials based on ref.[13],[14] & [19], will be given in this chapter.

2.1 Chemical Structure and Physical Properties

The streamer skin being used in the streamer design today is thermoplastic polyurethane elastomers (TPU). The material is essentially formed from inter-reaction of three components. Long chain diols and short chain diols react with diisocyanates through polyaddition to form linear (single chain) polyurethane. A linear polymer may also become cross-linked, which is the binding together of polymer chains at various places by means of strong covalent bonds. Another type of linking is chain entanglement. Polyaddition is a polymerization process which involves breaking down of double covalent bonds and redistribution of these bonds as single bonds between whole series of carbon atoms. Thermoplastic means that the polymer shows a glass transition, which will be discussed more later.

The polyols (e.g. polyether) form the flexible component of the elastomer. The combination of diisocyanates with short chain diols produces the rigid components (segments). The modulus of elasticity for the polymer will essentially be controlled by the ratio of rigid to flexible segments. Higher levels of rigid segments will result in a higher modulus. It is also observed that increasing diisocyanate content progressively raises the glass transition temperature (T_g). As will be shown later, the mechanical loss factor has a maximum at T_g. The maximum in mechanical loss can then in principle be controlled by the diisocyanate content in the processing of polyrethane. This is only correct to a certain extent (low frequency) due to the fact that the mechanical loss factor is dependent on both frequency and temperature.

This knowledge can be used in streamer design. For example the streamer skin material Elastollan 1180A ref.[10] has a T_g at -30 °C with a mechanical loss factor of 0.55 at this temperature. At 10 °C the loss factor is 0.1 and this is 5 times lower. That is, if we would like to have a high damping factor for noise like breathing waves in the section, we could do this by shifting the T_g from -30 °C to 10 °C, and thereby increasing the loss at this operational temperature. One of the problems with this is that the modulus would also increase. This results in a stiffer streamer skin, that can cause operational problems. The phase speed of breathing waves would also increase considerably. But some increase in stiffness will be tolerable and this means that the material 1190A seems to be a better choice than 1180A with regards to damping of breathing wave noise.

2.2 Viscoelasticity

Elastic solids and viscous fluids differ widely in deformation characteristics. Elastically deformed bodies return back to undeformed state when the applied load is removed. Viscous fluids do not possess the same property of deformational recovery.

The classical theory of elasticity deals with mechanical properties of **elastic** solids. For which, in accordance with Hooke's law stress is always directly proportional to strain in small deformations, but independent of the rate of strain.

The classical theory of hydrodynamics deal with the properties of **viscous** liquids, for which in accordance with Newton's law, the stress is always directly proportional to rate of strain, but independent of the strain itself.

These categories are idealizations. Still, the behavior of many solids approach Hooke's law for infinitesimal strains, and the behavior of many liquids approach Newton's law for infinitesimal rates of strain. Material behavior which incorporates a blend of both elastic and viscous characteristics, is referred to as viscoelastic behavior.

A body that is not quite a solid does not maintain a constant deformation under constant stress but continues to slowly deform with time, or creeps. When such a body is constrained at constant deformation, the stress required to hold diminishes gradually or relaxes. A body that is not quite a liquid may store some of the energy instead of dissipating it all as heat. It may recover part of it's deformation when the stress is removed (elastic recoil). When such bodies are subjected to sinusoidally oscillating stress, the strain is not in phase with the stress. Some energy is stored and recovered in each cycle, and some is dissipated as heat. If both strain and rate of strain is infinitesimal, the behavior is **linear viscoelastic**, and in a given experiment the ratio of stress to strain is a function of time (frequency) alone, and not of stress magnitude.

In deformation of solids, the atoms are displaced from equilibrium positions in a force-field which is quite local in character. The elastic constants can then be calculated from interatomic potentials. Viscous flow in ordinary liquids reflects the change (with time) of distribution of molecules surrounding a given molecule. Forces are quite local in character and viscosity can in principle be calculated.

In a polymer, the molecules pervades a volume much greater than atomic dimensions. Many different kinds of movements are possible for the macromolecule: i)Elastic changes of bond angles and bond distances, ii) changes in conformation of side groups and smaller parts of the main chain, iii) changes in the shape of molecule's contour by internal rotations around the bond angles of its main chain iv) and changes of relative position of neighboring macromolcules relative to each other.

Rearrangements on a local scale, involving smaller parts of the molecule, occur relatively fast and contribute little to the deformability of the material under stress. The movement is slower when larger parts of the molecule is involved in the movement. This explains the huge scale of characteristic times occurring in movements of the macromolecules covering several orders of magnitude in time, and also the enormous changes in modulus covering over 10 orders of magnitude.

Experimental measurements of mechanical properties are usually made by observing external forces and changes in external dimensions of bodies with a simple shape e.g. cube.

The strain tensor and the stress tensor is given respectively in Appendix B1 and B2.

It might be easier to understand viscoelastic behavior by looking at the stress relaxation experiment and the Creep experiment for a viscoelastic material given in Appendix B3. Viscoelastic properties is often qualitatively described by mechanical models, enclosed in appendix B4.

2.3 Periodic Experiments

The relaxation and creep experiments described in appendix B3 are not periodic and only supply information at long times (very low frequency). Periodic experiments supply information corresponding to short time and higher frequency than relax/creep experiments. For audible and seismic cases the periodic experiments are the most relevant.

The stress may be varied periodically with a sinusoidal alternation at a frequency f(Hz) or ω (radians/sec). A periodic experiment at frequency ω is qualitatively equivalent to a transient experiment at time $t=1/\omega$. If the viscoelastic behavior is linear, the strain will alternate sinusoidally but out of phase with the stress. The relation can be shown from the constitutive equation in Appendix B2.

The periodic strain for simple shear:

$$u_{21} = u_{21}^{0} \sin\omega t \qquad (2,1)$$

Application of the constitutive equation in Appendix B2 give the following relation:

$$\sigma_{21}(t) = u_{21}^{0}(G'(\omega)\sin\omega t + G''(\omega)\cos\omega t) \tag{2.2}$$

Where G' and G'' is:

$$\begin{aligned} G' &= \omega\int_0^\infty G(s)\sin(\omega s)\,ds \\ G'' &= \omega\int_0^\infty G(s)\cos(\omega s)\,ds \quad , s = t - t' \end{aligned} \tag{2.3}$$

The amplitude $\sigma_{21}{}^{0}$ of the stress and the phase angle δ between stress and strain:

$$\sigma_{21} = \sigma_{21}^{0}\sin(\omega t+\delta) = \sigma_{21}^{0}(\cos\delta\sin\omega t + \sin\delta\cos\omega t) \tag{2.4}$$

Each periodic measurement at a given frequency provides two independent quantities: the storage modulus $G' = (\sigma_{21}{}^{0}/u_{21}{}^{0})\cdot\cos\delta$ and the loss modulus $G'' = (\sigma_{21}{}^{0}/u_{21}{}^{0})\cdot\sin\delta$. The ratio $G''/G' = \tan\delta$ is called the internal damping or loss factor.

The sinusoidally varying stress can be expressed as a complex quantity, and the ratio :

$$\frac{\sigma_{21}^{*}}{u^{0}_{21}} = G^{*}(\omega) = G'(\omega) + jG''(\omega) \tag{2.5}$$

Where G^{*} is the complex modulus. The data from periodic experiments can also be expressed in terms of a complex compliance $J^{*} = 1/G^{*}$.

There is no change in volume in simple shear. The general constitutive equation for combined change in volume and shape includes all components of the stress tensor ref.[19]:

$$\sigma_{ij} = \int_{-\infty}^{t} [G(t-t')(\dot{u}_{ij} - \frac{1}{3}\sum \dot{u}_{kk}) + \frac{3}{2}K(t-t')(\frac{1}{3}\sum \dot{u}_{kk}\delta_{ij})]\,dt' \qquad (2.6)$$

G(t-t') is the shear relaxation modulus and K(t-t') is the volumetric relaxation modulus.

In a bulk compression experiment, the dimensions of a cubical element increases or decreases uniformly. The stress components $\sigma_{11}=\sigma_{22}=\sigma_{33}=$ -P and all other stress components are zero. The strain components are equal. If we put this into equation (2.6), we get the result: $P(t)=-(\delta V/V)\cdot K(t)$. The volumetric strain $(\delta V/V)=(3/2)u_{11}$. The complex dynamic modulus K^* is defined in the same way as for shear.

2.4 Simple Extension

The experiment is called simple extension, if an isotropic cubic element is elongated in one direction and the dimensional change of the mutually perpendicular directions are equal. That is $u_{11}>0$, $u_{22}=u_{33}\leq 0$. Again by using equation (2.6) we get (after calculation):

$$\sigma_{11}(t) = \epsilon \frac{9G(t)K(t)}{G(t)+3K(t)} \qquad (2.7)$$

Where $\epsilon=\partial u_1/\partial x_1=1/2u_{11}$ is the tensile stain. The fraction is denoted E(t) and called tensile relaxation modulus. For equilibrium deformation in a solid E=9GK/(G+3K) is called Youngs modulus. The complex tensile modulus is defined $E^*=E'+jE''$.

The relation between G and E can be written in terms of a dimensionless variable, Poisson's ratio: $\mu=(1-(1/V)(\partial V/\partial \epsilon))/2$. This corresponds to degree of lateral contraction accompanying a longitudinal extension. Poisson's ratio is also complex: $\mu^*=\mu'+j\mu''$.

The ratio of imaginary part to the real part is called the loss modulus: $(\tan\delta)_\mu$. The loss modulus is defined in a similar way for simple shear and simple extension.

The relations between the different complex moduli, complex compliances and complex Poisson's ratio obey the same equations which are valid for linear elastic materials. The relation between E^*,G^* and μ^* is:

$$E^* = 2G^*(1+\mu^*) \tag{2.8}$$

It can be shown that $(\tan\delta)_c \leq (\tan\delta)_s$. In general $(\tan\delta)_\mu$ is small and the difference between shear and extension damping is insignificant.

2.5 The Time, Frequency and Temperature dependence

There is little information available from the manufacturers about the frequency dependence of viscoelastic parameters for seismic streamer skin materials. Data for mechanical properties like shear modulus and mechanical loss factor is given as a function of temperature. Appendix B5 shows the shear modulus and loss factor for the material Elastollan 1185A. Note the distinct transition in modulus around -30°C. The material has a maximum loss close to this temperature. The term transition is used to signify dramatic changes of macroscopic material properties. The glass transition temperature T_g can be defined as the point of maximum slope on the modulus-temperature plot.

The time-temperature shift superposition principle states that a change in temperature shifts the position of creep compliance plot along log time axis without any change in shape. This is an approximate description and only valid if one single molecular process dominates. This principle can be used in experiments to determine e.g. modulus or compliance over a wide time-frequency scale by applying the time-temperature shift equation to measurements in a smaller frequency spectrum made at different temperatures.

For the glass-rubber transition of amorphous polymers, the Williams-Landel-Ferry (WLF) shift equation is used for a large number of polymers:

$$\log a(T,T_s) = \frac{-c_1(T-T_s)}{c_2+T-T_s} \tag{2.9}$$

Where the reduced time is given by: $t/a(T,T_s)$. The constants c_1 and c_2 are the WLF constants and depend on definition of reference temperature T_s. The temperature T_s is defined to be the temperature where the creep compliance after 16 seconds passes half the step height of the transition.

The creep time t_g (s) of the logarithmic midpoint of the glass-rubber transition is then from the definition of softening temperature: log $t_g(T_s)$=log(16)=1.2. The position of the logarithmic midpoint of the glass-rubber transition at an arbitrary temperature T is given by:

$$\log t_g(T) = 1.2 + \log a(T,T_s) \tag{2.10}$$

A typical temperature-frequency relation for complex modulus in polymers can be seen in fig.2.1. Note how the maximum in the lossfactor E_2/E_1 is a function of both temperature and frequency (time).

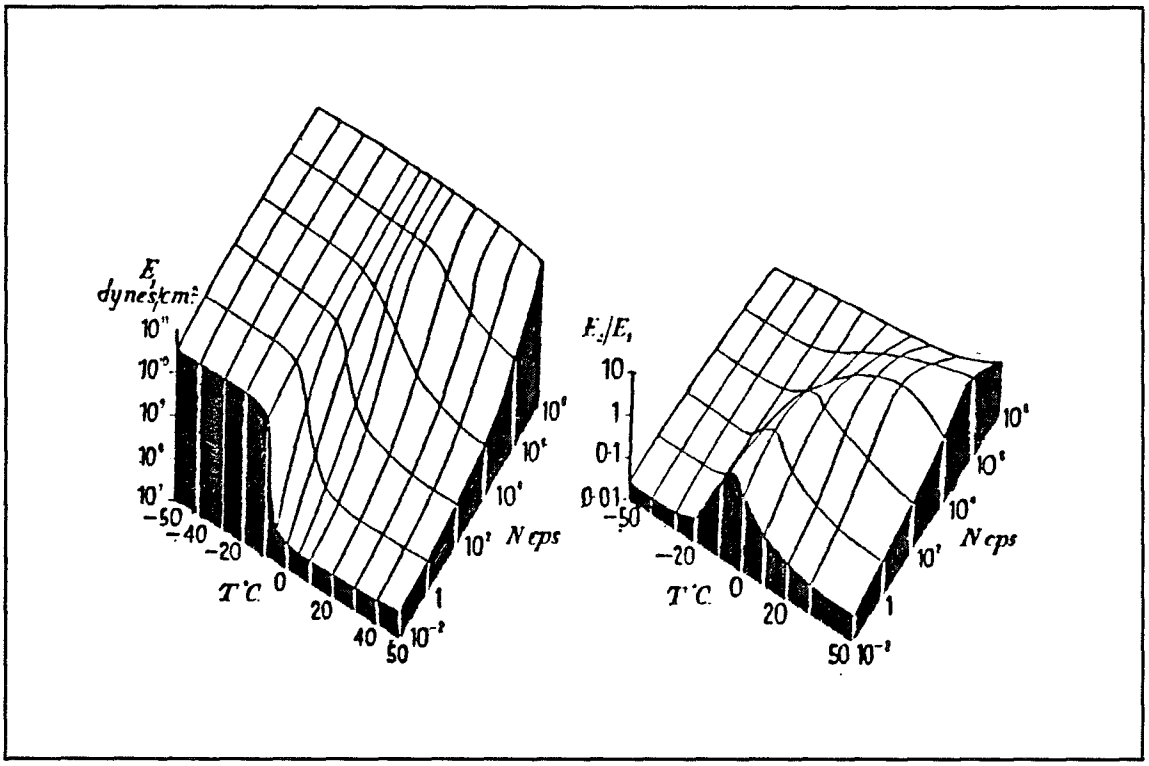

Figure 2.1 Approximate temperature-frequency relation for complex modulus in polymers

3.0 MEASUREMENTS OF VISCOELASTIC BEHAVIOR

In this chapter the results of three methods for measuring viscoelastic behavior in seismic streamer skin will be presented. It will be seen in chapter 5 that the viscoelastic behavior of streamer skin, represented by the complex frequency dependent Young's modulus, is an important parameter in the theoretical model for bulge waves in streamer sections. From the theory of viscoelasticity we recall that different experiments cover different time/frequency intervals. In the present work, three fundamentally different experimental methods have been applied on samples of streamer skin. The methods are: i) Ultrasonic wave propagation method, ii) Resonance method (bending waves) iii) Transfer function method (a simple extension experiment).

3.1 The Ultrasonic Method

The ultrasonic method is a wave propagation method. The method is used for determination of stiffness and loss factor for materials. The method involves measurement of wave propagation velocity and attenuation. The measurement setup is shown in fig.3.1. For measurements directly on long samples of streamer tube, the wave propagation is transversal to the tube axis. The dimension of the sample in the transducer plane normal to wave propagation is much greater than the wavelength. Calculations of nearfield distance shows that the waves can be regarded as plane in the present measurements. The wave propagation will therefore be modelled as plane wave propagation in an infinite media, as described in ref.[36]. Diffraction effects are not included in the theory here.

The speed and attenuation in the measurements are directly related to the complex plane wave modulus $M^*=M'+jM''$. The plane wave modulus M^* can be expressed by the Lame coefficients: $M^* = \lambda^*+2\mu^*$. The complex Young's modulus E^*, which is needed later in the breathing wave model in chapter 5, can be found from relations between E^* and M^*. The equation of motion in terms of compressional displacement is ref [36]:

$$M^*\nabla^2\Delta = \rho\frac{\partial^2\Delta}{\partial t^2}, \qquad \Delta = \epsilon_{kk} \tag{3.1}$$

where ρ is density and Δ is compressional displacement.
The propagation speed is approximately: $c=(M'/\rho)^{1/2}$

The solution to the wave equation is:

$$\Delta = \Delta_0 e^{j(\omega t-kx)} \tag{3.2}$$

The propagation constant:

$$k = k - j\alpha = \omega/c - j\alpha = \omega[\rho/(M' + jM'')]^{\frac{1}{2}} \tag{3.3}$$

Equation (3.2) can now be written:

$$\Delta = \Delta_0 e^{-\alpha x} e^{-jkx} e^{j\omega t} \tag{3.4}$$

Where α is the attenuation constant and $k=\omega/c$ is the real wavenumber. Equation (3.3) can be solved for relations between α, k, M' and M'' ref.[17]:

$$\alpha^2 = \frac{(F-1)\rho\omega^2}{2F^2M'} \tag{3.5}$$

$$k^2 = \frac{(F+1)\rho\omega^2}{2F^2M'} \tag{3.6}$$

$$F = \sqrt{1+(M''/M')} \tag{3.7}$$

For the complex plane wave modulus M^* we find:

$$M'' = 2S\alpha\frac{c}{\omega} \quad , \quad M' = S(1-(\alpha c/\omega)^2) \tag{3.8}$$

Where S is:

$$S = \frac{\rho c^2}{[1+(\alpha\frac{c}{\omega})^2]^2} \tag{3.9}$$

The Young's modulus can now be found from relation to the plane wave modulus ref [36]:

$$E' = \frac{M'(1-\sigma-2\sigma^2)}{(1-\sigma)} \quad , \quad E'' = \frac{M''(1-\sigma-2\sigma^2)}{(1-\sigma)} \tag{3.10}$$

Where Poisson's ratio σ is regarded as real.

From measurements of propagation velocity c and attenuation α, the complex Young's modulus can be found.

The loss factor is: $\tan\delta_M = M''/M' = \tan\delta_E = E''/E' = 1/Q$

Results of Experiments:

The measurements were done on approximately 2 meter long samples of streamer skin. Results from measurements on 3 mm and 4 mm thick streamer skin, made of the material Elastollan 1185a Polyurethane will be presented here. The measurement setup is shown in fig.3.1.

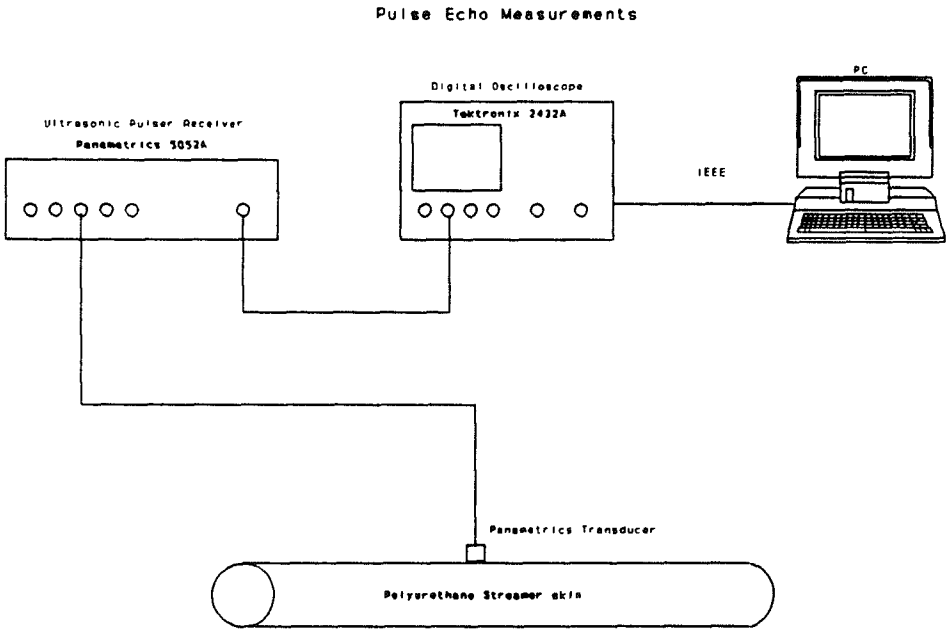

Figure 3.1 Experimental setup for Ultrasonic Pulse Echo method

The ultrasonic transducer is placed on the empty streamer skin, using ultrasound gel as contact medium. The ultrasonic analyzer Panametrics 5052UA was applied in pulse-echo mode. The same transducer is then applied for both transmitting and receiving the signal. The short transmitted pulse is superposed on the multiple received pulses. The transmitted and received pulses can be tuned to optimize signal to noise ratio. The signals are digitized by the Digital Scope Tektronix 2432A and transferred to a PC for graphical presentation and calculations.

Three different Panametric transducers have been used for these measurements. The transducers have a resonance frequency respectively at : 0.5 MHz, 2.25 MHz and 5 MHz. The diameter of the transducers are respectively: 30 mm, 15 mm and 30 mm. The measurements with 0.5 MHz are not reliable due to long wavelength. The wavelength is approximately 3 mm at 0.5 MHz. With a two-way travelling path at 6mm for a 3mm skin, the received signal is interfering with the transmitted signal, even if the transmitted signal is tuned to a single period. The transducer with a resonance frequency of 2.25 MHz gave the best results.

The measurements are repeatable for different positions on the streamer skin. Measurements at 5 different positions with 5 cm spacing along the streamer skin show negligible difference in speed and attenuation. Comparison of measurements with same transducer on 3 mm and 4 mm streamer skin shows more than 10 % higher speed in the 4 mm skin at 2.25 MHz. This kind of variance is not surprising when dealing with polymers of different thickness and originating from different production (processing) series of same material. But there is also a possibility that this is due to effects from the measurement method.

Fig.3.2 shows a plot of first, second and third reflection in pulse echo measurement on 3 mm skin with 2.25 MHz transducer.

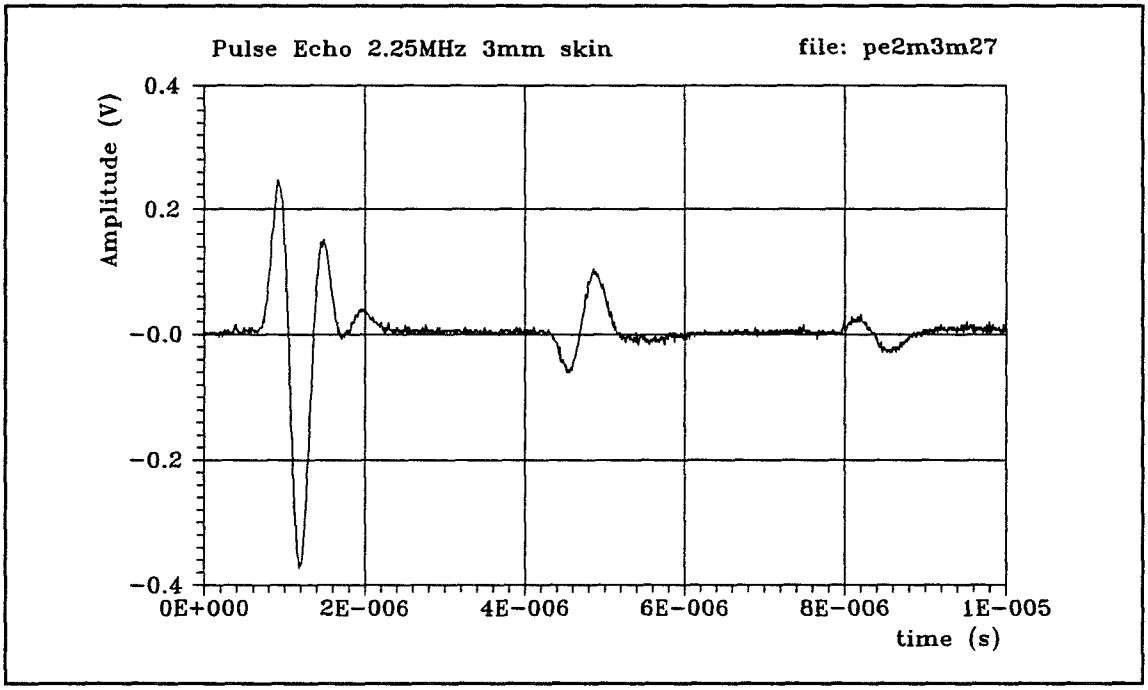

Figure 3.2 Ultrasonic 2.25 MHz Pulse Echo, 3 mm streamer skin

Fig.3.3 shows the same multiple reflections for measurements with 4 mm skin.

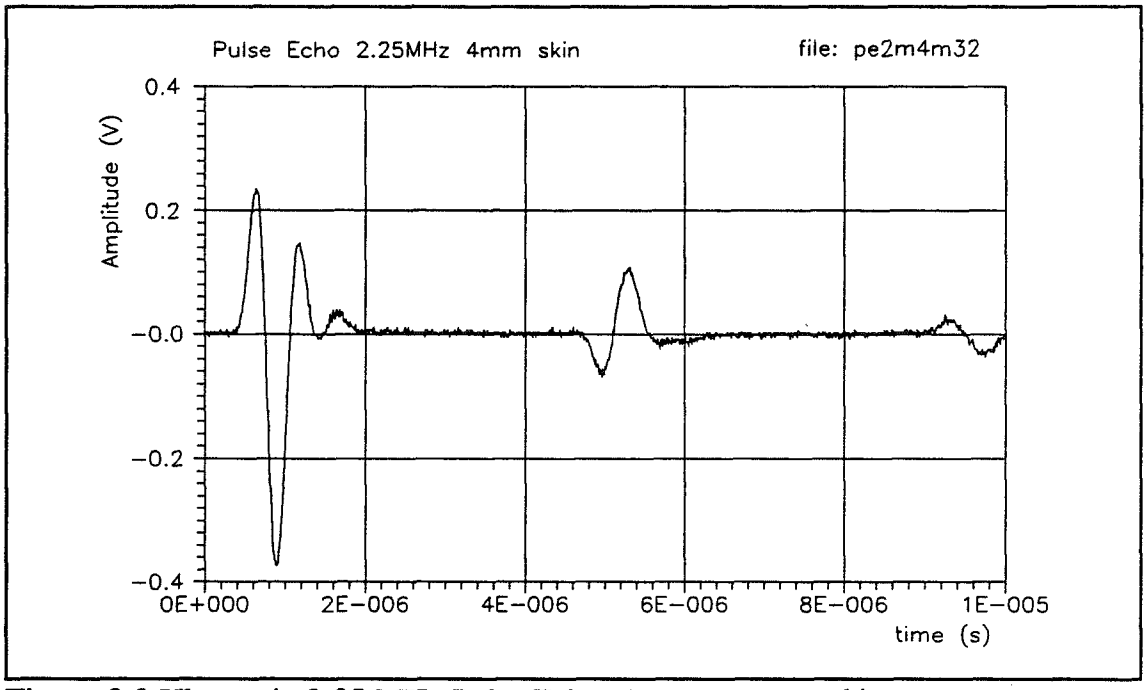

Figure 3.3 Ultrasonic 2.25 MHz Pulse Echo, 4 mm streamer skin

Based on these measurements, the above theory can be applied to calculate the complex Young's modulus. An example of this calculation from the measurements in fig.3.2 is shown in Appendix C1.

A summary of measurements with different transducers and material thickness h is shown in table 3.1. below: (α is attenuation factor and α_{2h} is total attenuation for a pulse travelling forward and backward through the skin)

f[MHz]	α[dB/cm]	α_{2h}[dB]	c [m/s]	E'[GPa]	E''[GPa]	tanδ	h[mm]
0.5	25.1	15.1	809	0.28	0.049	0.171	3
2.25	18.7	11.2	1648	0.93	0.046	0.050	3
2.25	14.7	11.7	1848	1.14	0.049	0.044	4
5	31.6	19	1653	0.93	0.034	0.038	3

The calculated Young's modulus is about 100 times bigger than the low frequency modulus. This is expected according to the viscoelastic theory. It is also interesting to note that the loss factor is much lower at these high frequencies, than in the low frequency measurements that will be shown in the next two sections. The loss factor increases with frequency up to the transition in modulus and decreases after this for increasing frequencies (only one major transition for E1185a). From previous calculations in chapter 2 on viscoelasticity, the transition frequency at room temperature should be in the order of 100 kHz. The measurements at 2.25 MHz is considerably higher than this frequency, and it is therefore reasonable that the lossfactor is quite low at 2.25 MHz and 5 MHz.

The accuracy of this method is dependent on measurement of wave propagation velocity and damping. The uncertainty in the measurements of speed and damping are approximately 2 %. The calculations are based on plane wave propagation in the sample. The thickness of the sample should be several wavelengths thick when using this method. The wavelength when using the 2.25 MHz transducer is approximately 1 mm. The accuracy of the measurements with the 0.5 MHz transducer is therefore not too good. Other factors like excitation of shear waves, variation in thickness and mechanical contact between transducer and skin etc., makes the estimate of total inaccuracy complicated. A total uncertainty of about 10 % can be expected in the calculations of Young's modulus and damping factor, when using the 2.25 MHz transducer.

3.2 The Resonance Method

The Resonance Method is used as a term for the measurements with B&K Complex Modulus Apparatus type 3930. This method is based on the industrial standard DIN 53440. The clamping apparatus, exciter, pickup and analyzer is shown in fig.3.4. The sample is clamped firmly in one end or both ends. The apparatus can be used for excitation of both transverse vibration and longitudinal vibration. In the present work, this system was used to excite transverse vibrations. A system for extensional vibrations will be presented in the next section 3.3.

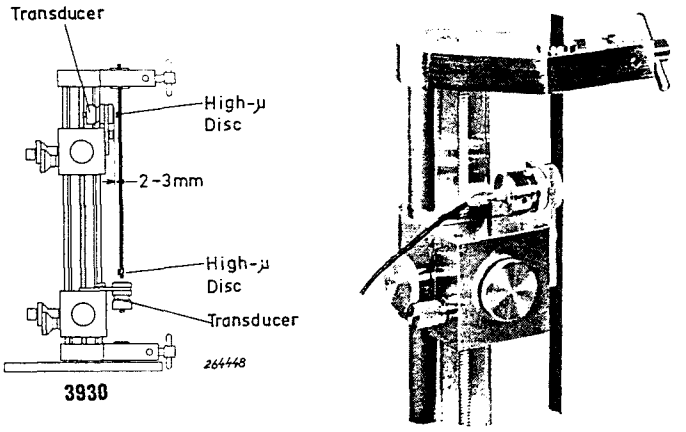

Fig. 3.1. Sketch showing the method of mounting samples and transducers.

Figure 3.4 Setup For Measurements with Complex Modulus Apparatus

An electromagnetic transducer is used for excitation of transversal vibration. The transducer is positioned relative to the sample in a distance of approximately 2mm (not touching). The pickup is either another electromagnetic pickup or a capacitive sensor. The capacitive sensor is a displacement sensitive sensor, and the electromagnetic sensor is velocity sensitive.

A small accelerometer B&K 4374 was placed on the sample in some of the measurements. The weight of this accelerometer is 0.65 g.

The samples were cut out from processed streamer skin of type elastollan polyurethane 1185. Samples were prepared with different width 6mm,8mm,10mm and from both 3mm and 4mm thickness. The samples were cut out as segments along the horizontal tube axis of the streamer skin. The segments were taken from the same tube samples that were used in the ultrasonic measurements. The cutting was done as precisely as possible with a numerically controlled cutting machine at the Laboratory of Plastics Technology at DTH. High-μ disc's were glued to the material at the sensor position. This is necessary when a nonmagnetic material is tested.

The theory described in the instruction and application handbook from B&K is the same as described in the original standard DIN 53440. The theory is based on classical mechanical theory for transversal vibrations in a clamped bar. The method has several limitations e.g. the setup with a long membrane/bar makes the polyurethane skin behave more like a membrane, especially at low frequency.

The equation for real Young's modulus given in the instruction manual may not be recognized immediately. The equation can however be verified by separating the same constants in a standard presentation on transversal vibrations in a bar.

The equation for real Youngs modulus in the manual is:

$$E' = 48\pi^2\rho \frac{l^4}{h^2}\frac{f_n^2}{k_n^2} \tag{3.1}$$

Where:

	ρ	is density (Kg/m^3)
	l	is active length (m)
	h	is thickness in the plane of vibration (m)
	k_n	factor dependent on boundary conditions
	f_n	frequency of n'th resonance

for clamped-clamped case: $k_1=22.4, k_2=61.7, k_3=121, k_4=200, k_5=299, \ldots$

The complex Young's modulus is: $E^*(\omega) = E'(\omega)+jE''(\omega) = E'(1+jd)$

$d = E''/E' = \tan\delta = 1/Q$ is called the loss factor. The lossfactor is found at each resonance peak as the inverse of Q-factor. The complex Young's modulus is then found at the discrete frequencies where there is a resonance top in the spectrum. In theory intermediate values can be found by measuring with different lengths between clamps.

Expectations to Measurements:

It is possible to constitute an approximate low frequency modulus and loss modulus based on the material data given from the manufacturer. The background for this is discussed in chapter 2 on viscoelasticity. The shear modulus as a function of temperature can according to the time-temperature correspondence principle be used to approximate low frequency Young's modulus at a fixed temperature as a function of frequency.

From the material data for Elastollan 1185a ref.[10]. Real Young's modulus:
$E = 30\ N/mm^2$ ($0.3 \cdot 10^7\ N/m^2$). Loss-factor $\tan\delta \approx 0.1$ at 3 Hz and room temperature.
From the temperature characteristic: Young's modulus should be increasing monotonously with increasing frequency up to the maximum in lossfactor.

From the theory for bending waves in a bar clamped at both ends, we know that the resonance frequencies are not harmonically related. The second resonance frequency is 2.76 times the first and so on: $f_2 = 2.76 * f_1$, $f_3 = 5.4 * f_1$, $f_4 = 8.93 * f_1$, $f_5 = 13.34 * f_1$.

Experimental setup:

The material sample which is clamped at both ends is excited with the electromagnetic transducer. In present work a B&K 2032 FFT analyzer was used to record the spectrum. The excitation signal was also generated by built-in analyzer. A pseudo random signal in the frequency range 3Hz to 1.6 kHz was used in these measurements. Some measurements were also executed with manual excitation "plucking".

The polyurethane material is quite soft and do not hang perfectly straight down if only clamped at upper end. The measurements were therefore conducted with both ends clamped. Different distances between upper and lower clamp were applied to generate different spectrums of resonance frequencies. It was difficult to control the tension in the material due to the yielding in the material at the clamped ends. It was therefore difficult to get the same tension in the material for different lengths between clamps.

Measurements:

The measurements were executed with different lengths, width and thickness of the material. The auto spectrum function in B&K2032 analyzer is applied to find E' and tanδ at the resonance peaks. There is no absolute calibration for the level in these plots. It is only positions and widths of the resonance peaks that are of importance for the calculations.

notation:

l= distance between clamps (total length sample is longer)
w= width of sample
d= thickness sample
me=magnetic excitation
pe=pluck excitation
mp=magnetic pickup
dm=distance between magnetic transducer and sample surface
ap=accelerometer pickup

Meas.id: e8te2
l=164mm, w=8mm, d=3mm, me, mp, dm=2mm,

Meas.id: e6te8
w=6mm, else same

The auto spectrum, Power Spectrum Density (PSD) 0-800 Hz can be seen in fig.3.5. The PSD for measurement id: e8te2 is shown in fig.3.6.There should be no influence from using samples of different widths, according to the model. We see that there is little change in the positions of the peaks when changing from 8 mm to 6 mm sample.

In order to achieve constant tension a mass element of 100 grams (corresponding to 0.5 bar pressure inside a streamer) was attached to the lower end of sample instead of clamped. Of course this turned out to be very impractical in this setup due to several things: pendulum effects, noise etc. Therefore, I went back to the method of adjusting the tension manually to same tension in each experiment.

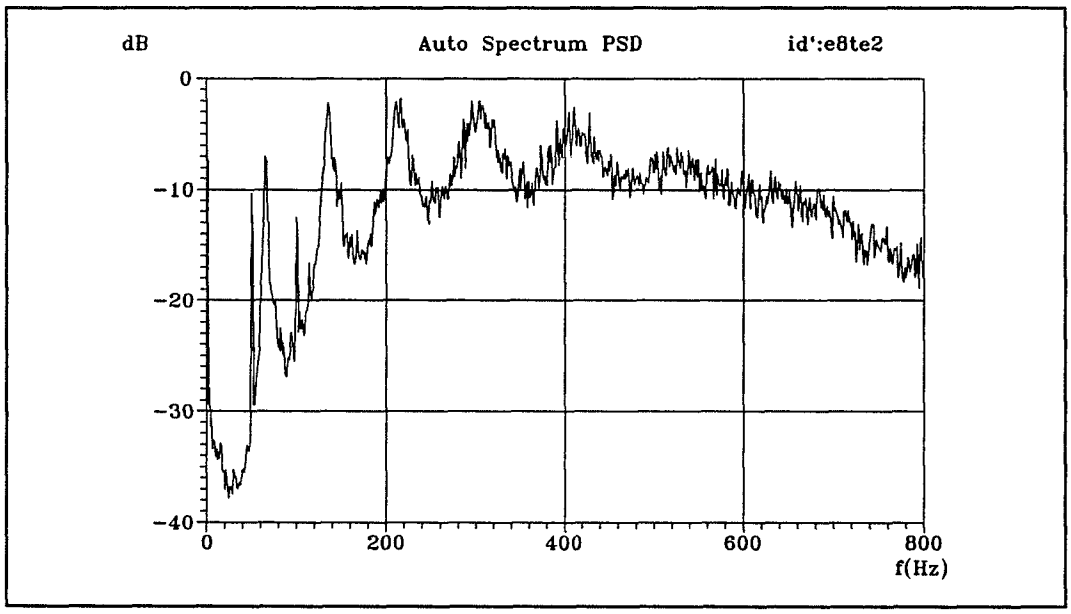

Figure 3.5 Auto Spectrum PSD [dB], Transversal Vibration Resonance, l=164mm, w=8mm

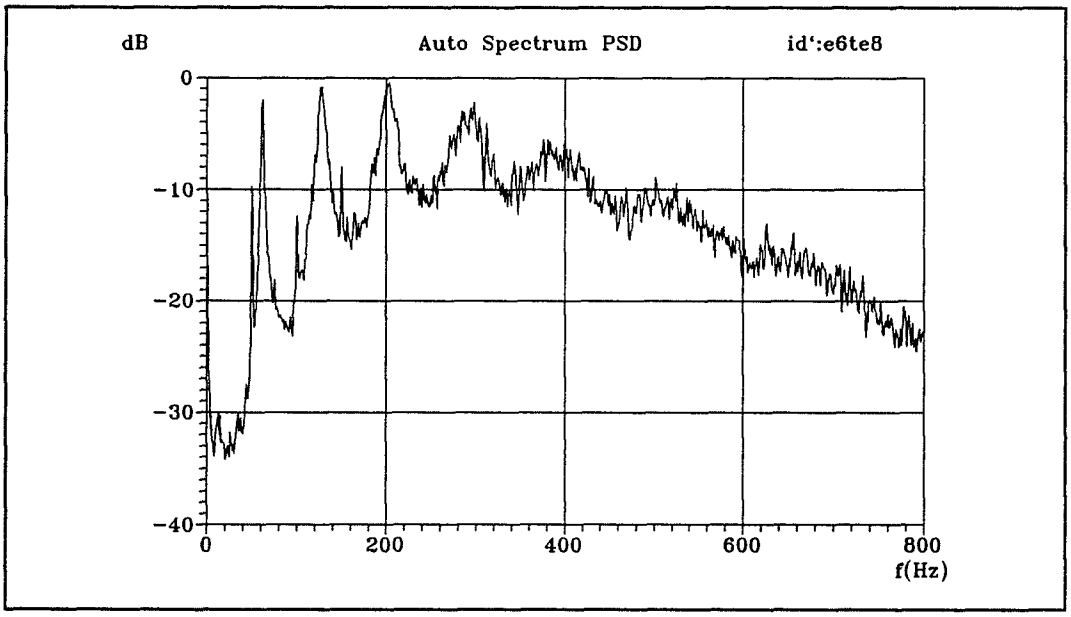

Figure 3.6 Auto Spectrum PSD [dB], Transversal Vibration Resonance, l=164mm, w=6mm

Meas.id: e6y8
l=180mm, w=6, d=3mm, me, mp, dm=2mm

Fig.3.7 shows the PSD for this measurement. The first resonance seems to be at $f_1 = 37$ Hz. The resonance frequencies and the width δf_n (3dB down) is shown in table 3.2 below.

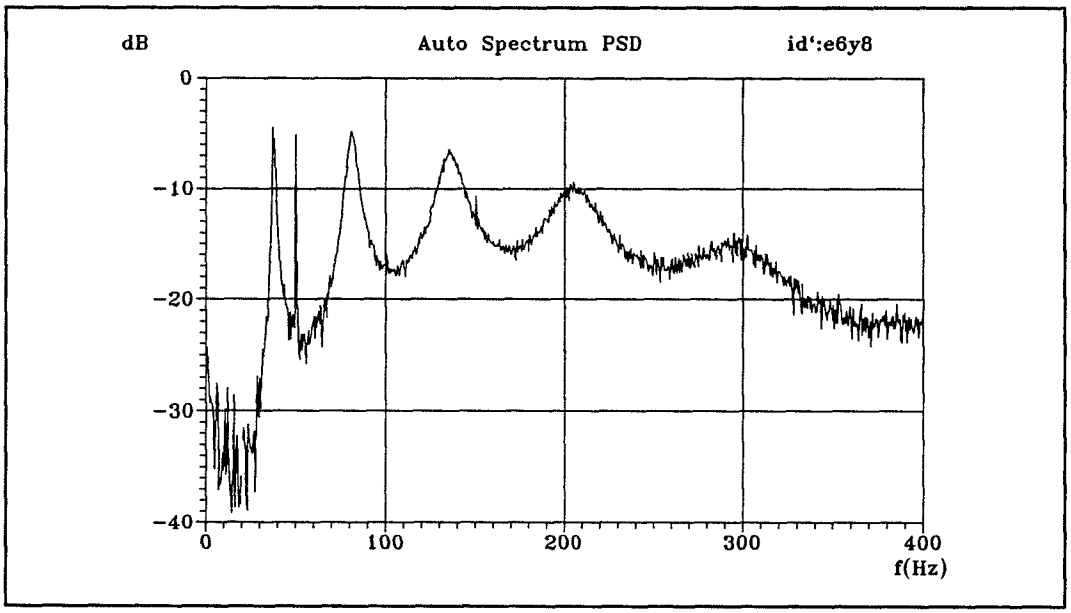

Figure 3.7 Auto Spectrum PSD [dB], Transversal Vibration Resonance, l=180mm, w=6mm

Table 3.2

n	1	2	3	4	5
f_n	37	81	135.5	205	295
δf_n	2	5.5	13.5	26.5	52

Using equation (3.11) to find the complex modulus from value of f_n. This done in MCAD-file: comp6m3 (Appendix C2).

The results show a higher real Young's modulus at low frequency and then decreasing with increasing frequency. According to the temperature response and the theory for viscoelastic behavior in polyurethane, this must be wrong. This was not easy to explain for quite some time. Some of the possible reasons at this stage was thought to be:

1) Influence of electromagnetic transducer. Static magnetic field is known as a possible source of inaccuracy (ref.B&K)

In order to investigate the influence of the electromagnetic transducer, different distances between the head and the sample was tested. This problem is described in the original german DIN 53440 norm. The recommended distance is 2-3mm from the sample surface and the position along sample should be close to the clamps. It was possible to see that the influence was a lot smaller in the measurements when the position of transducers were moved closer to clamps. Furthermore, a small accelerometer B&K4370 with a weight of only 0.65 grams was fixed with wax to the sample. Still, the same decreasing Young's modulus was found from the calculations. The position of the receiving transducer is important. By placing the accelerometer exactly in the midpoint between clamps some of the resonance peaks disappear. If this spectrum is used the E-module is increasing with frequency, but its value is much too high.

2) Influence of clamping (effective length (f) etc.), Factors in equation wrong etc.

3) Another thing is that the model might not be correct for this material. The bending stiffness might be so low that it is moving more like a membrane/string, and the resonance only dependent on tension and mass/length of sample. This could possibly also explain why the resonance frequencies increase when the sample is stretched more between the clamps.

Equation (3.1) was verified by checking against well-known theory on vibration in a bar. The expected approximate low frequency value from data for Young's modulus was confirmed by another method (simple extension experiment), that will be described in the next section.

Returning now to the problem of interpreting the resonance measurements. From other measurements and expectations, I know that the real part of Young's modulus is not changing much (typical 10%) in interval 2-200 Hz. So by solving equation (3.1) for f_n with a constant expected value for E, should give approximate values of expected resonance frequencies.

The results of expected values for resonance frequencies:

Table 3.3

l (mm)	f_1	f_2	f_3	f_4	f_5
131	29.7	81.8	160.5	265.3	396.6
164	19	52.2	102.4	169.3	253
180	15.7	43.3	85	140.5	210.1
272	6.9	19	37.2	61.5	92

l is the length of sample between clamps.

The case with l=180mm. When comparing the expected frequencies in table 3.3 with the measured ones in table 3.2, we see that the expected f_2 matches what I thought to be f_1. The expected f_3 matches measured f_2 and so on. It is quite obvious that the first resonance frequency is missing in the measurements or at least it is very weak compared to the others. The first peak in these measurements is then f_2.

This must be taken into consideration in calculation of complex modulus from equation 3.1. The new calculations with the above considerations is shown for the case with l=180mm in Appendix C3. The calculations now give a reasonable value for Young's modulus as a function of frequency.

Some additional measurements with accelerometer as pickup sensor instead of electromagnetic are shown in fig.3.8& 3.9.

Meas.id:fk10m11
l=131mm, w=10mm, d=3mm, me, dm=2mm, ap.
The position of the accelerometer was 1/8 of l from lower clamp.

Meas.id:fk10m12. Same as above, but accelerometer was positioned exactly in the middle between the clamps.

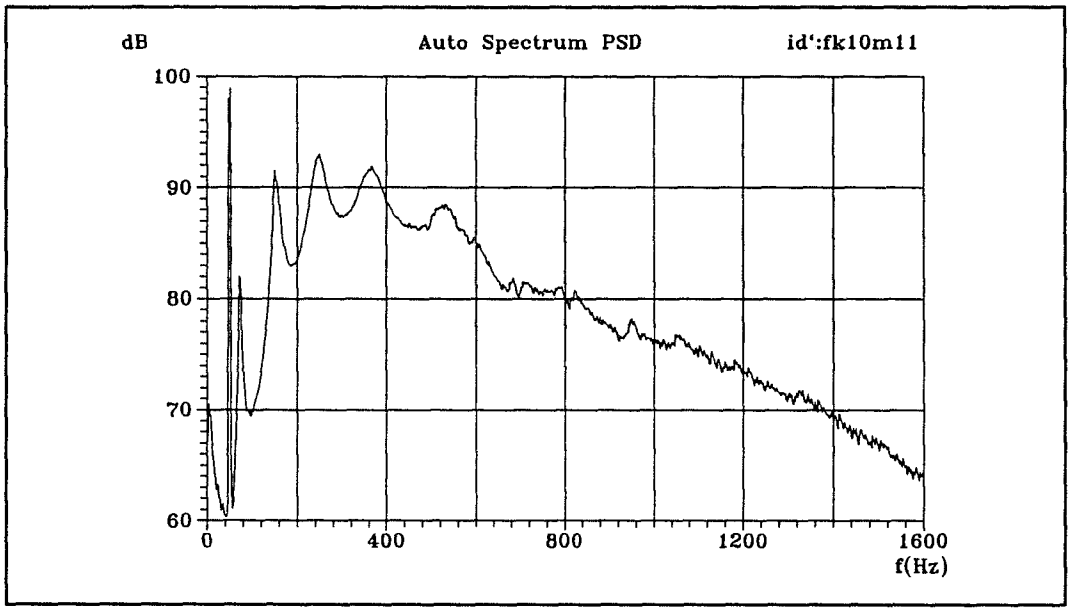

Figure 3.8 Auto Spectrum PSD [dB], Transversal Vibration Resonance, l=131mm, w=10mm, Pick up 1/8 from lower clamp.

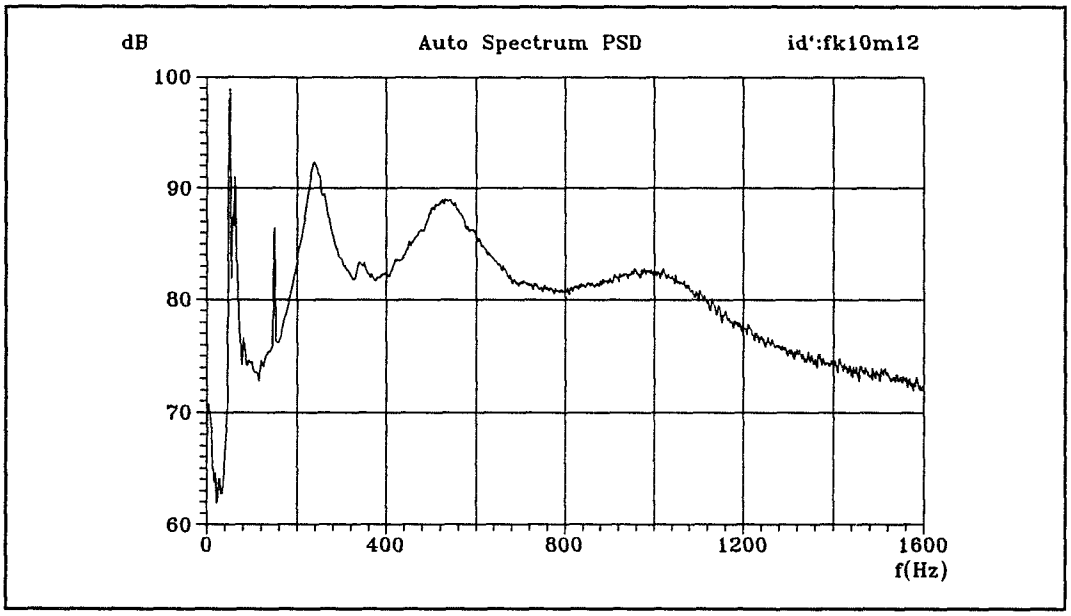

Figure 3.9 Auto Spectrum PSD [dB], Transversal Vibration Resonance, l= 131mm, w=10mm, Pick up midpoint between clamps.

When these two plots are compared it is possible to see that in fig 3.9 every second resonance is suppressed. This is due to the position of accelerometer. Only the even modes that are clearly visible, though some weak signs of the odd modes can also be seen.

The effect of lower temperature was tested by cooling down in a refrigerator from 20 °C to 5 °C. The effect was according to expectations: the resonance at 70 Hz moved to 78 Hz, 150 to 170 Hz, 242 to 282 Hz, 350 Hz to 415 Hz.

Many more measurements with different lengths between clamps and other combinations were carried out. The values are in the same order as the above, with a typical 20% variation in value for E. This is probably due to the difficulties of repeating the same clamping (same tension).

Experience with this apparatus has shown that this method is not straight forward when applied to soft polymer materials like this. There is a lot of tricks to pick up before getting measurements and interpretation correct. Furthermore, the method is time consuming and only give values at discrete frequencies.

The calculated Young's modulus based on the above measurements is not used in later modelling of breathing waves. A more convenient method which results in continuous measurements of Young's modulus will be described in the next section 3.3.

3.3 Simple Extension Experiment

This method results in a continuous complex modulus within a limited frequency range. It was possible to measure the complex modulus as a function of frequency in the frequency range 15-200 Hz. For materials in seismic applications this is probably the best method available. More heavy signal processing is involved in the calculations, but it is a fast method when standard programs can be used. The system is based on measuring the transfer function of extensional waves in a bar of the material (sample). A similar experimental setup was used by Bente Vestergaard ref.[18] in her Ph.D.-project at the Department of Solid Mechanics DTH.

Some changes were made to the data acquisition system. The earlier version used single frequency stepping through the spectrum, and the transfer function was calculated from single frequency measurements in a PC. In the present work, the built-in pseudo random noise generator in a B&K 2032 analyzer was used and the measured transfer function was then transferred to a PC for signal processing. The program for signal processing is the same as in ref.[18]. A model for vibrations in a bar according to the theory by Buchanan is implemented, using Newton-Raphson iterations. This program was used to find the complex modulus from the measured transfer functions in samples of streamer skin.

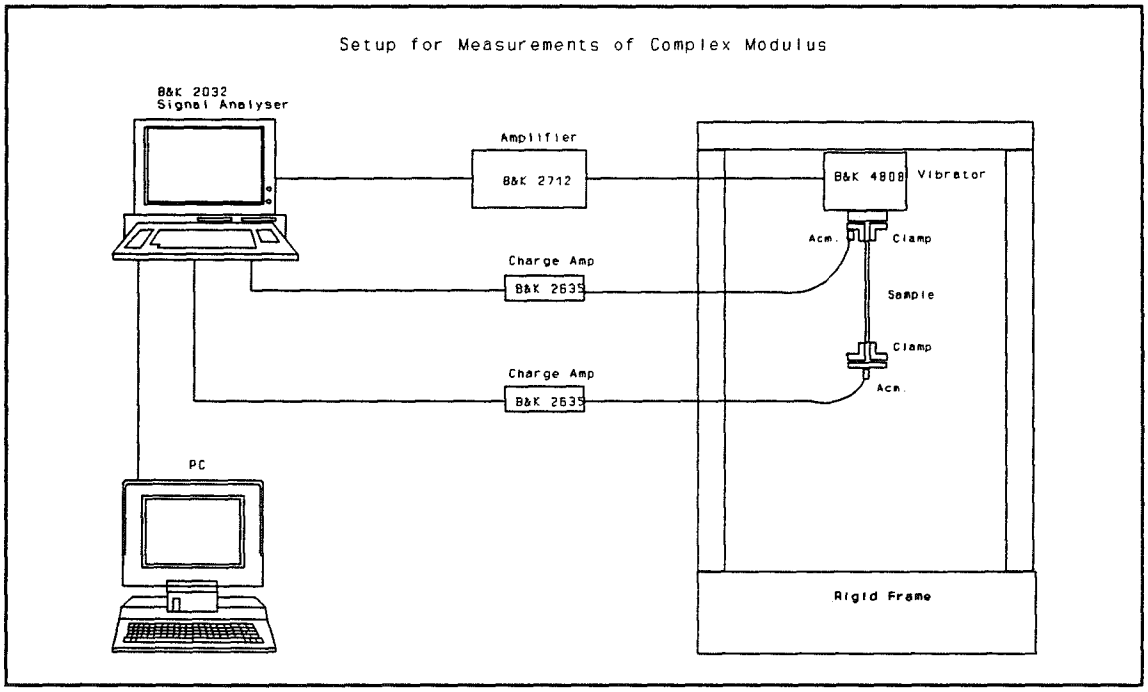

Figure 3.10 Setup for Measurements of Complex Modulus by extensional vibrations.

The experimental setup is shown in fig.3.10. Pictures (F1 and F2) from the experiment can be seen in appendix F2. A rigid frame is mounted on a solid base. The vibrator B&K4808 is mounted (up side down) on the upper side of the frame. A special clamp is mounted on the moving plate of the vibrator. The sample is hanging down with a similar clamp at the lower end. Two accelerometers are mounted, one in each end. The accelerometers are connected via charge amplifiers to the two channel analyzer. The signal generator is used in pseudo random mode with sufficient amplitude. By using the coherence spectrum on the analyzer, it was possible to check the validity of the transfer function.

The model:

A bar of length L and cross sectional area α and density ρ is clamped at one end and the other end is loaded with a mass m. The clamped end is harmonically excited. Longitudinal waves will be propagating in the sample. The model is taken from ref.[18].

The displacement u(x,t) from equilibrium in the sample is described by the equation:

$$\alpha E \frac{\partial^2}{\partial x^2} u(x,t) - \alpha \rho \frac{\partial^2}{\partial t^2} (u(x,t) + u_0(t)) = 0 \tag{3.12}$$

Boundary conditions:

$$u(0,t) = u_0(t) \quad , \qquad -\alpha E \frac{\partial}{\partial x} u(L,t) = m \frac{\partial^2}{\partial t^2} (u(L,t) + u_0(t)) \tag{3.13}$$

The forced vibration at the clamped end is: $u_0(t) = u_{01} e^{i\omega t}$

The solution to this is:

$$u(x,t) = \left[\cos(kx) + \frac{\gamma + \tan(kL)\sin(kx)}{1 - \gamma \tan(kL)} - 1 \right] u_0(t) \tag{3.14}$$

$$k^2 = \frac{\rho \omega^2}{E} \quad , \quad \gamma = \frac{m\omega^2}{k\alpha E} \tag{3.15}$$

The ratio of accelerations is the same as the ratio of displacements due to harmonic forced vibration gives: $u(x,t)'' = -\omega^2 u(x,t)$. From a known value of $E(\omega)$ the transfer function is found as:

$$F(\omega) = Ae^{i\phi} = \frac{u(L,t)+u_0(t)}{u_0(t)} = \frac{1}{\cos(kL) - \gamma\sin(kL)} \tag{3.16}$$

Introducing the ratio: mass of load (m) to mass of sample (M)

$$R = \frac{m}{\rho \alpha L} \tag{3.17}$$

Defining the complex variable $\zeta = kL$. The characteristic equation to be solved is then:

$$f(\zeta) = \cos(\zeta) - R\zeta\sin(\zeta) - \frac{e^{-i\phi}}{A} = 0 \tag{3.18}$$

This equation is then solved for ζ from measured value of $F(\omega)$. The corresponding value for complex modulus is then found:

$$E(\omega) = \frac{\rho \omega^2 L^2}{\zeta^2} \tag{3.19}$$

Measurements:

The measurements were done in the laboratory at department of solid mechanics at DTH. The low frequency response is dependent on the length of the sample and the mass of the lower clamp. Series of measurements were done with different lengths of the same material which was used in the earlier modulus apparatus test.

Test sample: 3mm Streamer skin, Polyurethane, Elastollan 1185A.

The clamps were mounted on a sample with the following dimensions: 3mm thickness, 10mm with and free length 60mm (between clamps). The sample was aligned normal to the clamps, to avoid inducing initial shear stress.

Two accelerometers of type B&K4393 were glued to the clamps. The accelerometer mounted on the upper clamp (at driver) serve as a reference. The weight of the accelerometers is 2.4 grams. Some measurements were done with a bigger accelerometer (B&K4370) at the lower clamp. The weight of this accelerometer is 54 grams.

Calibration:

The calculation of modulus from transfer function demands calibration of the two signals. The charge amplifiers B&K2635 was set according to sensitivity of the accelerometers. The input channels on the analyzer was set to 10mV/unit both channels.

The two accelerometers were glued to the same clamp (same position). The vibrator was driven by pseudo random noise to give an acceleration level of 5 m/s^2 (0.5g). The frequency response in this configuration gives the difference in sensitivity for the two sensors. The calibration data was transferred to files for future corrections to transfer functions in calculation of modulus.

Calibration data:

Instruments used in all measurements:

Analyzer: B&K 2032 s#1245506
Charge amp ch.A : B&K 2635 s#1624972
Charge amp ch.B : B&K 2635 s#117118

Specific to configuration:

File: cal8m (magnitude), cal8p (phase)

Accelerometers:	chA	acm.1, B&K4393 s#:1501182
	chB	acm.3, B&K4370 s#:757916

File: ecal8mag (magnitude), ecal8phase (phase)

Accelerometers:	chA	acm.1, B&K4393 s#:1501182
	chB	acm.2, B&K4393 s#:1326479

Three series of measurements with different lengths of sample were executed. The lengths are: l=60mm, l=117mm & l=258mm. The measurements with l=60mm is the data that will be used in the calculation for modulus. The length of the sample influences the resonances in the combined system of mass element and sample modulus. The first resonance at low frequency is the low frequency limit for the measurements. This can be moved by using different lengths of the sample.

The best measurements is achieved with the sample of length l=60mm. Though the low frequency response below 30Hz is better with the sample of length l=117mm. The measurements with sample length l=258mm is not presented here, due to obvious wrong response. This is most likely due to increasing pendulum movement instead of simple extension. This effect is probably the reason for the problems seen at higher frequencies around 150 Hz. The transfer function H1 Magnitude and Phase, is transferred to a PC for further calculations and presentation.

Measurement id: tr10m3
Config: l=60mm, acm.1 (ref) & acm.3
Transfer function, 3-200Hz, H1 mag & phase

The transfer function is shown in fig.3.11. As expected, both the real Young's modulus and loss factor is increasing monotonically. There is a low frequency resonance at 25 Hz, and probably an antiresonance at 125 Hz. From the theory and the shear modulus measurements at room temperature with torsion decay method (material data) we expect a value for $E'(\omega,T)$ and $\tan\delta(\omega,T)$: $E' = 30*10^6$ N/m^2, $\tan\delta=0.1$ at room temperature and approximately a frequency of 10 Hz. This can to a certain degree be used to verify a single point (typically at 10 Hz) in the present measurements of modulus as a function of frequency. The present measurements for Young's modulus and lossfactor at 10 Hz is close to the expected values.

The following measurements are enclosed in appendix C4:

Measurement id: tr10m40
Config: l=60mm, acm.1 (ref) & acm.2
Transfer function, 3-800Hz, H1 mag & phase

Measurement id: tr10m43
Config: l=60mm, acm.1 (ref) & acm.2
Transfer function, 3-200Hz, H1 mag & phase

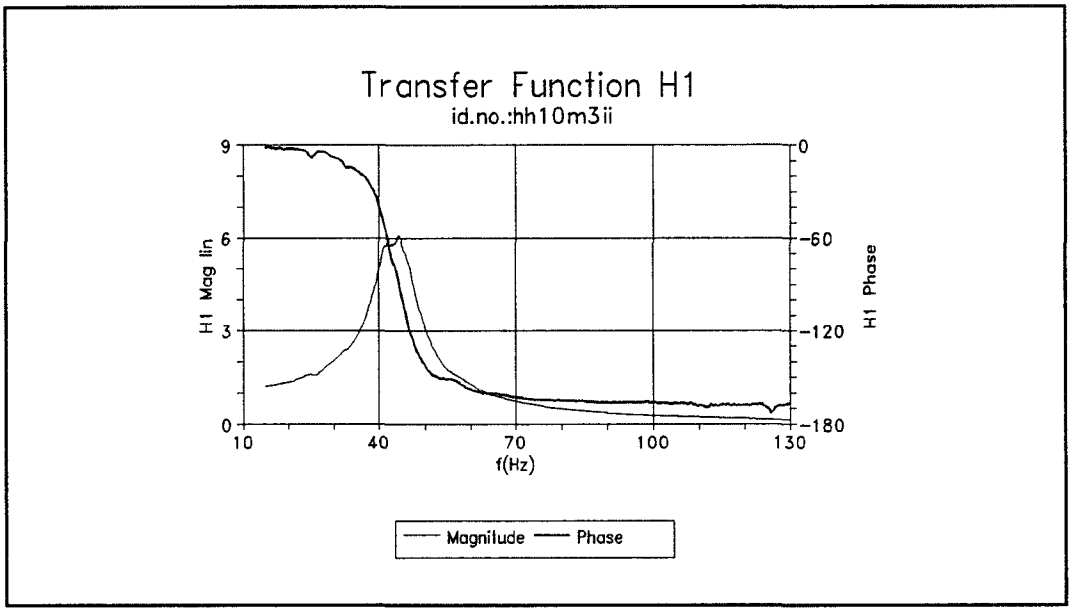

Figure 3.11 Transfer Function extensional vibration in 3mm skin.

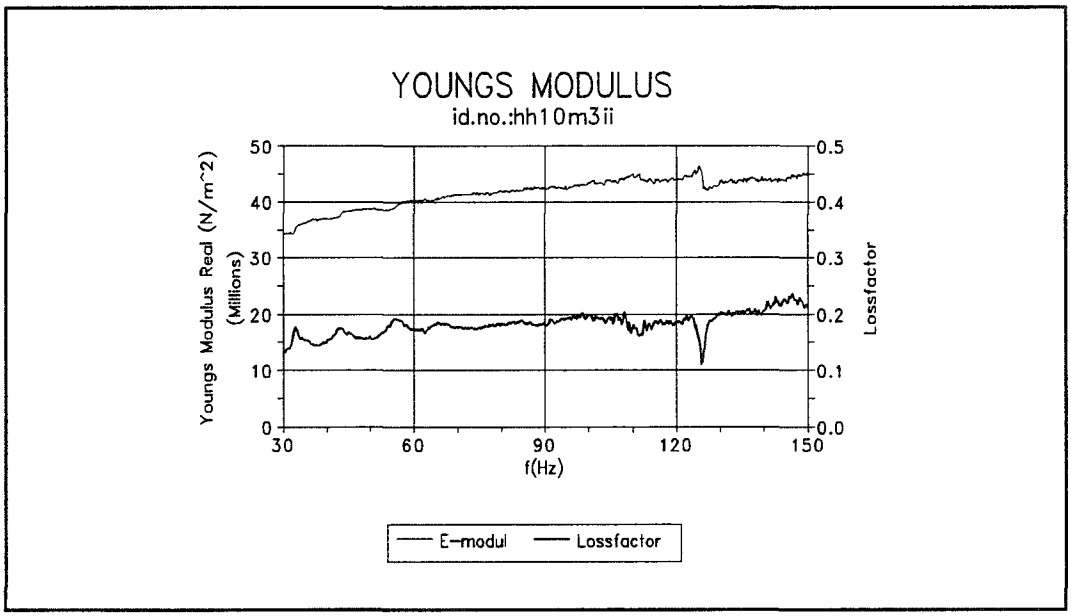

Figure 3.12 Complex Modulus for 3mm skin Elastollan 1185

Calculation of Complex modulus:

The transfer function from the analyzer is transferred to a PC for calculations of complex modulus. The software for calculation of modulus is a fortran program. The software ref [18] originally running on a SUN workstation, was transferred to a normal IBM 386 33MHz PC. In order to use a Lahey FORTRAN Compiler, it was also necessary to have OS386 installed. The complex modulus software is based on the model described in the theory above.

In order to use the transfer function data as an input to the modulus program it was necessary to make some changes to the files transferred from the analyzer. Manipulation like : 1) Phase changing: H1 phase between 180 and -180 was changed to monotonically decreasing. 2) Implementing calibration data. 3) H1 magnitude changed from dB to linear. 4) H1 mag & phase placed in sided columns in same file.

There is a configuration file, which have to match the specific measurement configuration.

Config file: main.ind
mass [kg], areal [m^2], length [m], density [kg/m^3]

Running software > up main.exp

Out file: main.ud
freq [Hz], H1 mag lin, H1 ph, --,--, E'[N/m^2], E''[N/m^2]

The results can then be plotted in a graphics package like Grapher or QPRO.

The result of the calculations is presented as real Youngs modulus E', and loss factor $\tan\delta = E''/E'$.

Complex modulus as function of frequency corresponding to the input data id: tr10m3 is presented in fig.3.12. The complex modulus has id no: hh10m3ii.

In a similar manner the corresponding calculations of complex modulus for the other input data is labeled: id.no: hh10m40 and hh10m43 (Enclosed in Appendix C5.)

The experimental material data will be used as an input to the theoretical bulge wave model that will be described in chapter 5. The bulge wave model is a continuum mechanical model, which take into consideration the viscoelastic behaviour of the streamer skin and the dynamics of the fluid inside. The model is also supported by input of real material data, like the complex Young's modulus from measurements described in this section (3.3). It is then necessary to develop a numerical function from the experimental data. This is done by polynomial least squares fit.

The method is based on propagation of one dimensional waves in a perfect bar sample. This idealization will have an effect on the accuracy of this method. In addition to this, the inaccuracy of the accelerometers and other instruments will contribute to the total uncertainty of the calculated modulus.

1) Uncertainty due to cutting of sample. It is difficult to cut a perfect bar from the viscoelastic tube. The sides are not perfectly normal to the surface. There is also a variation in width of the sample along the bar.

2) Uncertainty in parameters like: density, mass of load, area and length.

3) Uncertainty due to deviation from one dimensional wave model.

A proper analysis of these factors would be very complicated. Intuitively one should expect uncertainty due to cutting of sample to be the dominant factor of uncertainty, though limitation due to model can also contribute strongly. An uncertainty in the order of 10 % in the calculated Young's modulus can be expected with this method.

Curve fitting by Polynomial least squares:

This is standard procedure which is available in mathematics software like: MCAD.
The calculated data for complex modulus was transferred to a procedure in MCAD advanced math (application package). The result of fitting a polynomial of degree 3 to the complex modulus data is shown in fig.3.13. and fig.3.14.

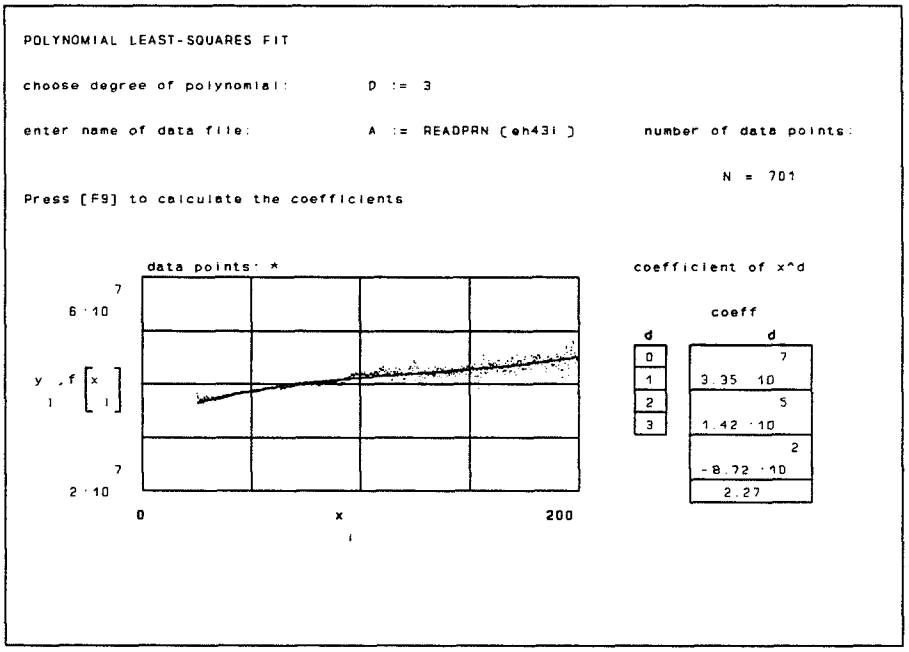

Figure 3.13 Polynomial Least Squares Fit of Real Young's Modulus

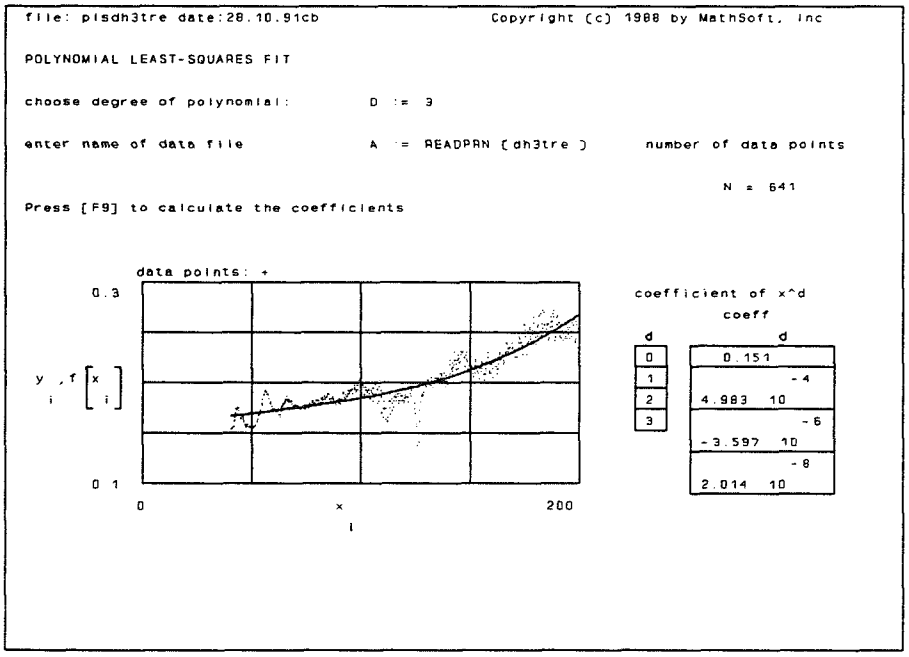

Figure 3.14 Polynomial Least Squares Fit to Lossfactor Data

3.4 CONCLUSIONS ON METHODS OF MEASUREMENT:

Three fundamentally different methods for measurement of complex modulus have been studied.

The ultrasonic method do not give data in a directly applicable frequency range. It might be possible to use symmetry principles to predict low frequency properties. The advantage of the ultrasonic method is that it is easy to use and can be done directly on empty streamer skins (no cutting of sample). The ultrasonic method does not involve heavy calculations either. The ultrasonic measurements has shown aspects of the viscoelastic behavior not seen with the other methods. It has also been instructive to use the method in order to understand the loss mechanism in streamer skin. The full potential of this method has not been investigated, due to the limited time. The other methods give data directly in the seismic frequency range.

The vibration resonance method with the complex modulus apparatus B&K4390 is very time consuming. The method is based on resonance in the sample, and only give data at discrete frequencies. One can easily make fatal mistakes both in measurements and interpretations. The method is (was ?) a recognized industrial standard (DIN 53440), and is therefore a reference for comparing results. It is very time consuming compared to the extension method described in section 3.3.

I also hold the vibration resonance method (ref.section 3.2) to be less accurate than the extension method. There is a certain ambiguity in the results. The method is more suitable for materials of considerable higher modulus like metals. Soft materials can be glued to a metal bar, and the complex modulus can be found based on measurements with and without the soft material attached to the bar.

The data from the extension method will be the preferred input to the bulge wave model. The method gives continuous data for complex Young's modulus as a function of frequency in the range 20-300 Hz. The best results are achieved with relatively short samples e.g. l=60mm. This is probably due to nonlinear movement when using longer samples. The method demands a relatively complicated setup and signal processing to produce the complex modulus data.

Measuring viscoelastic behaviour in polymers like streamer skin is known to be difficult. This can be confirmed from the above experiments. Even so, reliable data for complex modulus as a function of frequency has been found. In the final breathing wave model, it is seen that the frequency dependence of the lossfactor and real Young's modulus is of considerable importance in the dispersion relation and in the frequency dependent damping factor. It is therefore essential to have realistic data for complex modulus if one shall have any hope of modelling the bulge waves in seismic streamers.

4.0 FLOW NOISE

The main activity in this project has been focused on the problem with noise due to the breathing wave mode, but some initial theoretical study on flow noise has also been started.

In some articles on flow noise, the breathing waves are also considered to be a part of the total flow noise. The two principal noise mechanisms are: 1) Direct propagation of pressure fluctuations from turbulent boundary layer. This convective component propagate along the array with same speed as the convection speed of the turbulent eddies. 2) Excitation of breathing waves.

The breathing wave mode can be excited both by local turbulence, or directly by vibrations in the stress-members connected to the fluid-filled tube. In solid-filled arrays the direct pressure fluctuations from the boundary layer outside are dominant. In liquid filled arrays the breathing waves are dominant. This is the reason why we have concentrated on the latter noise mechanism in our present seismic streamer design.

In 1951 Lighthill developed his theory of aerodynamic sound in order to control the noise of jet propelled aircraft. The source was defined to be the difference between the exact statements of natural laws and their acoustic approximations. The source distribution is found to be of quadropole nature, and is identified by the double divergence (of Lighthill's stress tensor) structure of the source term in the wave equation. In linear inviscid flow, Lighthill's stress tensor T_{ij} vanish. But in turbulent flow T_{ij} does not vanish and turbulence generates sound as a quadrupole source distribution.

The forces generated on the surface of a body in turbulence are of dipole nature and more efficient sources of noise than the compact quadropoles of free turbulence.

The sound of turbulent flow can often be easily heard due to entrained gas bubbles. Application of Lighthill's theory shows that the sound generated by turbulence with entrained gas (air) bubbles is much stronger than without bubbles.

The fluid motion in a turbulent flow is generally chaotic, but in some regions the flow is correlated. The term eddy is defined to be a region where the flow conditions are relatively similar. Flow quantities are well correlated within the eddy, but are uncorrelated over distances larger then the eddy dimension (correlation scale). The eddies are formed in non-uniform moving flows and tend to move with the mean stream. The cross correlation of the noise signal at space separation and time delays can be used to analyze the nature of the turbulent flow. Due to the stochastic nature of the noise signal, it is often described by the statistical properties.

file:wave\hydeff date: 8 12 91 cb

Ref. A J.Shashaty JASA 71(4) April,1982

Calculation of effective hydrophone length and discrimination against flow noise:

Sylinder hydrophone

Radius of hydrophone [m]: R = 0.015

Length of hydrophone [m]: L = 0 04

Speed [knots]: v := 5

Effective length hyd [m]: $X := 2 \cdot \left[R^2 + \left[\frac{L}{2} \right]^2 \right]^{\frac{1}{2}}$ X = 0.05

Effective group length [m]: g := 12 ·X g = 0.6

Discrimination cutoff [Hz] $fc = 6\ 45 \cdot \frac{2\ 54}{100} \cdot \frac{v}{g}$ fc = 1 365

n := 1 10 multiples of fc: f(n) := n ·fc

Attenuation dB : $d(f) := 20 \cdot \log \left[\frac{fc}{f(n)} \right]$

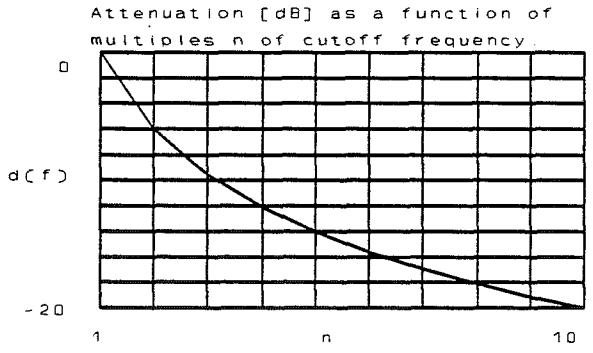

Figure 4.1 Calculation of effective length **ref.[7]**

In order to reduce the influence of noise from turbulent boundary layer the hydrophones are not in contact with the water. The clearance between the outer skin (hose) and the hydrophone is filled with a fluid.

Different hydrophones and distance to the skin have been studied to calculate flow noise in towed arrays ref.[6]. The turbulent pressure fluctuations are integrated over the effective area of the hydrophone, by using a weighted process based on dipole radiation from the hose wall as a definition of **area of effectiveness**. The **effective length** can be found by dividing area of effectiveness with the circumference. The **effective length** can be used for comparing the hydrophones susceptibility to flow noise. Discrimination against flow noise may be compared for hydrophones of various types and sizes ref.[7]. From this method a low frequency cutoff is found. Below this frequency there is no inherent discrimination in the design. And above this frequency, the discrimination is inversely proportional with frequency (1/f, 20 dB/decade). Some calculations for a seismic streamer design is shown fig.4.1.

In the article ref.[8], a quantitative prediction of the effect of convective flow noise is calculated by simple models. The penetration of convective flow noise to an interior point is given for different geometries and fillings.

For a flat plate geometry, the flow noise suppression at depth d is:

Liquids:

$$\frac{\delta p}{P} = e^{-\omega \frac{d}{v_c}} \tag{4.1}$$

Solids:

$$\frac{\delta p}{P} = \left[1 + \omega \frac{d}{v_c}\right] e^{-\omega \frac{d}{v_c}} \tag{4.2}$$

Where v_c is the convection speed of the eddies. δp is the pressure fluctuations measured by the hydrophone and P is the wall-pressure fluctuations. The effects of flow noise decrease exponentially with distance from the turbulent layer. This shows that it is important to have much distance between the hydrophone and the turbulent layer. It shows the difficulty in suppressing noise in thin line arrays.

Note that the pressure level is a factor $(1+\omega d/v_c)$ greater for solids than for liquids. This increase is due to the presence of the shear wave component, which is strongly attenuated in liquids. The disadvantage of solid filling is less at lower frequencies.

The above expressions are valid for a flat plate geometry. The extension to a cylindrical geometry, results in similar expressions as above. They exhibit the same exponential decay. The expression (ref.[8]) is only available for liquids, but the expression for solids is analog to the flat plate geometry.

Liquids:

$$\frac{\delta p}{P} = \frac{I_0(k_z a_h)}{I_0(k_z a)} \tag{4.3}$$

The model in ref.[8] also includes viscoelastic parameters for the filling. Oil saturated open cell foam is used in the model. The foam is a 97% porous open-cell rubber foam. It is expected that the oil is virtually trapped in the foam if the foam is strong with low porosity and the oil is highly viscous. For foam with large porosity which is saturated with oil of low viscosity, sloshing of the oil relative to the foam is expected. This introduces an additional attenuation mechanism. This should give lower noise level for foam of low porosity saturated with oil of low viscosity. The shear wave component of the flow noise is likely to increase, but the overall effect is probably a lower flow noise level for the correctly chosen materials.

The effect of oil saturated foam has not been fully investigated in the present project. The attenuation as a function of streamer radius for a liquid filled streamer is shown in fig.4.2

Experimental surface design for streamer skin:

During this project an experimental surface design of the streamer skin was tested on Geco Echo. The surface of the streamer skin was designed with semi-circular riblets. Ref. [33].

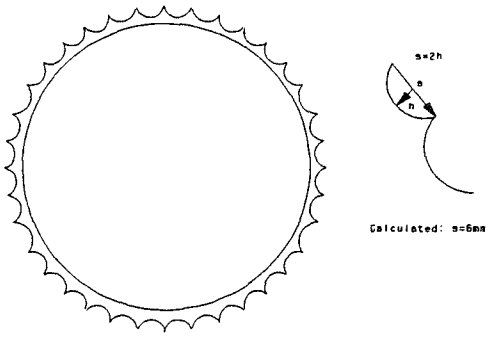

A prototype seismic hydrophone section with this skin, was sent out for test on the seismic ship Geco Echo. The results are described in the report: "Riblets on streamer skin" ref.[32].

Some initial analysis has been done during this project, and an average of 0.5 dB improvement in signal/noise ratio can be seen. A more careful investigation will have to be done in order to the verify the improvement in signal/noise by using riblet streamer skin. In the present project report, the focus has been on the other noise mechanism (breathing

file: wave\flow date:8.12.91 cb

Convective flow noise: ref Francis/Slazak/Berryman JASA 75(1) jan 84
Only valid for fluid filled streamer at low frequency

Streamer radius [m]: $a := 0.035$

Hydrophone radius [m]: $r := 0.015$

Tow speed [m/s]: $v = 2$

Convective speed [m/s] $c = 0.8 \cdot v$

Frequency [Hz]: $f := 10$

Wavenumber [1/m]: $k := \frac{2 \cdot \pi \cdot f}{c}$

Ratio streamer/hyd radius: $n := 1, 1.5 \ldots 5$

Radius streamer: $a(n) := n \cdot r$

$z1(n) := k \cdot a(n)$ $z2 := k \cdot r$ $z2 = 0.589$

Modified Bessel func: $I0(z) = 1 + \frac{z^2}{2^2} + \frac{z^4}{2^2 \cdot 2^2 \cdot 4^2} + \frac{z^6}{2^2 \cdot 2^2 \cdot 2^2 \cdot 4^2 \cdot 6^2}$

Flow Noise attenuation dB $d(n) = 20 \cdot \log\left[\frac{I0(z2)}{I0(z1(n))}\right]$

n	d(n)
1	0
1.5	- 1.051
2	- 2.693
2.5	- 5.066
3	- 8.204
3.5	- 11.968
4	- 16.106
4.5	- 20.376
5	- 24.608

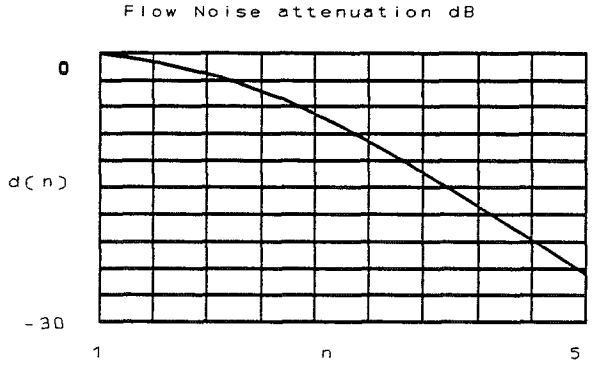

Figure 4.2 Calculation of flow noise level as a function of radius

5.0 MODEL FOR BREATHING WAVES IN STREAMER SECTION

The literature has been searched to find background material on the slowly propagating breathing waves that can be seen as the main noise component in fluid filled streamers.

One of the articles on this topic especially related to seismic streamers is by H.F. Weichart ref.[12]. From the measurements in the article, the fact that different streamer skin materials has an influence on the measured amplitude of noise signals was identified. Due to the fact that the measurements were done with 45 m long hydrophone groups, the measured speed was actually the propagation speed in the stress members and not the local speed of breathing waves. A theoretical model was developed to describe the wave propagation in the sections. In the results the only solution is a phase speed equal to speed of sound in water. From the given solutions in this article, it is seen that the theory only covers modes of little relevance. The breathing waves are not described by the theory in the above article.

Other articles published in Geophysical Journals on this topic tend to be very phenomenological. In the available articles and reports, the attempts to model the breathing waves have up to now started out with acoustic wave equations, which are not fundamental enough to reveal the nature of breathing waves.

As described in the introduction (chapter 1), the model developed in the Stad Girl report ref.[11] can not be used to describe the breathing wave mode.

The important fact that the distensibility of the tube is of far greater importance than the compressibility of the fluid, must be realized in order to find the breathing wave mode.

In the present streamer design, the bulk modulus for the oil filling is in the order of 10^9 Pa, while the elastic modulus (Young's) in the streamer skin is in the order of 10^7 Pa.

This indicates that the fluid can be regarded as incompressible. The wave propagation in fluid filled seismic streamers is similar to pressure wave propagation in blood veins.

In the paper by Morgan & Kiely ref.[1], the hydrodynamic equations for incompressible fluid and elastic equations for the tube wall is matched through boundary conditions at the wall. The solution of the equations contain Bessel functions of complex arguments and will in general have to be solved numerically. However, for restricted ranges of the variables approximate results in analytical form is derived.

The paper by Chow & Apter ref.[2] also take into consideration the mass of the tube wall. This was not included in Morgan & Kiely ref.[1]. Furthermore the correspondence principle between elastic and viscoelastic materials is explained. It is shown that the problem can be solved for a simple elastic tube, and then the elastic parameters can be replaced with the viscoleastic parameters of the tube in the solution. This principle has also been applied to the streamer model. Two different tube wall materials (voigt & linear solid) is considered in ref.[2] and dispersion and attenuation of waves are plotted. No analytical form of the solution is given in the article by Chow & Apter ref.[2].

The fluid is considered to be compressible and inviscid in the paper by Rubinow & Keller ref.[3]. However the tube walls have been considered viscoelastic in some cases. The equations of motion for the fluid and tube wall is solved to a complicated transcendental dispersion relation. Infinitely many modes of propagation is found. One of the tube modes can be identified as the breathing wave mode.

The problem is solved for many special cases like e.g. stiff wall and no wall. Only dimensionless equations for numerical solution is presented. The phase velocity and group velocity is plotted for some limited cases. No analytical equations for cases covering the streamer configuration is given in ref.[3]. There can be infinitely many modes existing in this system when losses are considered, acoustic modes and tube modes.

One of the useful things in the article by R&K ref.[3], is that it shows how an impedance matrix can be introduced to account for the constraint on the motion of the tube wall due to the surrounding medium. The actual expressions for the impedance is not presented here, but this can be found in the book by Fahy ref.[16].

In the case of breathing wave mode in the streamer with water as the surrounding medium, only the radiation impedance for 0-mode need to be considered. The radiation impedance is found to be purely reactive and represent a mass like load.

The theoretical model for wave propagation in streamer section developed here is very much the same as in the article by Morgan & Kiely ref.[1]. The theory is somewhat extended and modified to fit the streamer design. The dispersion relation found, is then used to find transfer functions from noise sources to groups of hydrophones, and also between single hydrophones in a seismic hydrophone array configuration.

5.1 The Theoretical Model for the Breathing Wave Mode

The purpose of this modelling has been to develop a model for breathing waves, that is connected to physical parameters in the streamer design. The model can be used both for evaluation of streamer design and in signal processing for reduction of noise.

In this system the distensibility of the tube is of far greater importance than the compressibility of the fluid.

The model will include the viscoelastic behavior of the tube wall and the viscosity of the fluid. The model will result in a dispersion relation.

Fundamental equations:

The fluid filled tube with dimensions is shown in fig.5.1. The fundamental equations will be developed in Cylinder coordinates (r,θ,x).

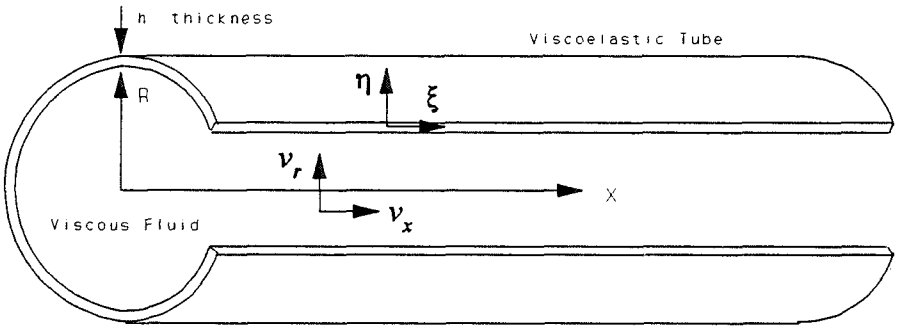

Figure 5.1 Cylinder coordinates

Assumptions:

- axial symmetry
- small disturbances (neglecting nonlinear terms).

With the above assumption the Navier Stokes equations for the fluid become:

$$\rho\frac{\partial v_r}{\partial t} = -\frac{\partial p}{\partial r} + \mu\left[\frac{\partial^2 v_r}{\partial r^2} + \frac{1}{r}\frac{\partial v_r}{\partial r} + \frac{\partial^2 v_r}{\partial x^2} - \frac{v_r}{r^2}\right] \tag{5.1}$$

$$\rho\frac{\partial v_x}{\partial t} = -\frac{\partial p}{\partial x} + \mu\left[\frac{\partial^2 v_x}{\partial r^2} + \frac{1}{r}\frac{\partial v_x}{\partial r} + \frac{\partial^2 v_x}{\partial x^2}\right] \tag{5.2}$$

The equation for conservation of mass:

$$\frac{\partial(rv_r)}{r\partial r} + \frac{\partial v_x}{\partial x} = 0 \tag{5.3}$$

The component of the stress tensor on an element of area perpendicular to radius is:

$$\sigma_{rr} = p - 2\mu\frac{\partial v_r}{\partial r} \tag{5.4}$$

The shear component of the stress tensor is (in direction parallel to the tube axis):

$$\sigma_{rx} = \mu\left[\frac{\partial v_x}{\partial r} + \frac{\partial v_r}{\partial x}\right] \tag{5.5}$$

Equations of Elasticity:

According to the correspondence principle the system equations can be solved for the elastic case and then replaced by the complex modulus to account for viscoelastic behavior:

The tension components in the tube wall is:

$$T_\theta = \frac{Eh}{1-\sigma^2}\left[\frac{\eta}{R_0} + \sigma\frac{\partial\xi}{\partial x}\right] \tag{5.6}$$

$$T_x = \frac{Eh}{1-\sigma^2}\left[\frac{\partial\xi}{\partial x} + \sigma\frac{\eta}{R_0}\right] \tag{5.7}$$

The equations of motion of the tube are:

$$\rho_0 h\frac{\partial^2\eta}{\partial t^2} = \sigma_{rr}(R,x,t) - \frac{T_\theta}{R_0} \tag{5.8}$$

$$\rho_0 h\frac{\partial^2\xi}{\partial t^2} = \frac{T_x}{\partial x} - \sigma_{rx}(R,x,t) \tag{5.9}$$

Substituting equations (5.6) and (5.7) into respectively (5.8) and (5.9):

$$\rho_0 h\frac{\partial^2\eta}{\partial t^2} = \sigma_{rr}(R,x,t) - \frac{Eh}{1-\sigma^2}\left[\frac{\eta}{R_0^2}+\frac{\sigma}{R_0}\frac{\partial\xi}{\partial x}\right] \tag{5.10}$$

$$\rho_0 h\frac{\partial^2\xi}{\partial t^2} = \frac{Eh}{1-\sigma^2}\left[\frac{\partial^2\xi}{\partial x^2} + \frac{\sigma}{R_0}\frac{\partial\eta}{\partial x}\right] - \sigma_{rx}(R,x,t) \tag{5.11}$$

Propagation of forced pressure waves:

Assuming that the propagating forced pressure waves are harmonic in time.
Then ξ,η,v_r,v_x, and p all vary as $e^{i(Kx-\omega t)}$. Where K is the complex wavenumber. $K=K_1+iK_2$. K_1 is real wavenumber and K_2 is the damping constant.

Let:

$$\begin{aligned} \xi &= Se^{i(Kx-\omega t)} \quad , \quad \eta = \delta e^{i(Kx-\omega t)} \\ v_r &= w(r)e^{i(Kx-\omega t)} \quad , \quad v_x = u(r)e^{i(Kx-\omega t)} \end{aligned} \tag{5.12}$$

Inserting these forms into the continuity equation. We see that the order of magnitude for ratio:

$$\left|\frac{v_r}{v_x}\right| = \left|\frac{w}{u}\right| = order|RK| \tag{5.13}$$

For small damping the $|K| \cong K_1 = 1/\lambda$

Introducing the restriction of long wavelength compared to radius: $R/\lambda << 1$ neglecting all terms of order R/λ in equation (5.1):

$$\frac{\partial p}{\partial r} = 0 \quad , \quad p = Pe^{i(Kx-\omega t)} \tag{5.14}$$

Comparing the second term on the right side in (5.2). This term can be neglected if we demand that in addition to $R/\lambda << 1$ also $\lambda(\omega\rho/\mu)^{1/2} >> 1$. Substituting equation (5.12) into (5.2) and (5.3):

$$-i\omega\rho u = -iKP + \mu\left[\frac{d^2}{dr^2} + \frac{1}{r}\frac{du}{dr}\right] \tag{5.15}$$

$$\frac{1}{r}\frac{drw}{dr} + iKu = 0 \tag{5.16}$$

Boundary conditions:

Continuity in velocity at the inside of tube wall: The velocity components in fluid is equal to velocity components of the tube wall.

$$U \equiv \frac{\partial \xi}{\partial t} = -i\omega S e^{i(Kx-\omega t)} = u(R_0)e^{i(Kx-\omega t)} \tag{5.17}$$

$$W \equiv \frac{\partial \eta}{\partial t} = -i\omega \delta e^{i(Kx-\omega t)} = w(R_0)e^{i(Kx-\omega t)} \tag{5.18}$$

These are the linear boundary conditions (u and w evaluated at R_0):
The necessary condition for this is: $\delta/R << 1$.

Substituting (5.12) and (5.14) into the equations of elasticity (5.10) and (5.11), and replacing σ_{rr} and σ_{rx} by (5.4) and (5.5):

$$-\rho_0 h\omega^2\delta = P - 2\mu\left[\frac{dw}{dr}\right]_{r=R_0} - \frac{Eh}{1-\sigma^2}\left[\frac{\delta}{R_0^2} + \frac{i\sigma K}{R_0}S\right] \tag{5.19}$$

$$-\rho_0 h\omega^2 S = \frac{Eh}{1-\sigma^2}\left[-K^2 S + \frac{i\sigma K}{R_0}\delta\right] - \mu\left[\frac{du}{dr} + iKw\right] \tag{5.20}$$

Simplifying Eqs. (5.19) and (5.20):

Considering terms containing S in (5.20):

Simple analysis shows that for small damping and no viscosity: $|\omega^2/K^2| \cong c^2 = Eh/2\rho R$
If ρ and ρ_0 is of same magnitude and $h/R << 1$, then the term containing S on the left side of (5.20) can be neglected.

Considering terms containing δ in (5.19):

Using the required $R/\lambda << 1$, it is seen that the left side of (5.19) can be neglected.

The above assumptions means neglecting the terms which represent the inertia of the tube in the equations of motion.

Using the assumption $R/\lambda << 1$ when comparing the two last terms in (5.20). It is seen that the term iKw can be neglected.

Equation (5.5) becomes: $\sigma_{rx}=\mu(\partial v_x/\partial r)$

The simplified (5.20) becomes:

$$S = \frac{i\sigma}{KR_0}\delta - \frac{\mu}{BhK^2}\frac{du}{dr}\Big|_{r=R_0} \quad , \quad B = \frac{E}{1-\sigma^2} \tag{5.21}$$

Combining (5.19) and (5.21):

$$P = 2\mu\frac{dw}{dr}\Big|_{r=R_0} + \frac{Eh}{R_0^2}\delta - \frac{i\sigma}{R_0K}\mu\frac{du}{dr}\Big|_{r=R_0} \tag{5.22}$$

The ratio of first term to last in (5.22) is of order R^2K^2/σ. According to long waves approximation the first term can be neglected.

$$P = \frac{Eh}{R_0^2}\delta - \frac{i\sigma}{R_0K}\mu\frac{du}{dr}\Big|_{r=R_0} \tag{5.23}$$

This approximation also reduces equation (5.4) to $\sigma_{rr}=p$

The four equations (5.15),(5.16),(5.21) and (5.23) together with boundary conditions (5.17) and (5.18), can be solved for the four unknowns: u, w, P and δ.

(5.15) and (5.23) give:

$$\frac{d^2u}{dr^2} + \frac{1}{r}\frac{du}{dr} + \frac{i\omega}{\nu}u = \frac{iK}{\mu}\frac{Eh}{R_0^2}\delta + \frac{\sigma}{R_0}\frac{du}{dr}\Big|_{r=R_0} \tag{5.24}$$

where $\nu=\mu/\rho$ is the kinematic viscosity

After restricting u(r) to be nonsingular at r=0, the solution to this differential equation is:

$$u = AJ_0(\alpha r) + \frac{K}{\omega}\frac{Eh}{\rho R_0^2}\delta + \frac{\nu\sigma}{i\omega R_0}\frac{du}{dr}\Big|_{r=R_0} \tag{5.25}$$

where $\alpha=(i\omega/\nu)^{1/2}$
A is a constant and J_0 is the Bessel function of order zero.
$du/dr|_{r=R0}=\alpha AJ_0'(\alpha R_0)=-\alpha AJ_1(\alpha R_0)$.

$$u(r) = AJ_0(\alpha r) + \frac{K}{\omega}Eh\frac{\delta}{R_0^2} - \frac{\sigma}{\alpha^2 R_0}\alpha AJ_1(\alpha R_0) \tag{5.26}$$

from (5.16) we have:

$$w = -\frac{iK}{r}\int_0^r r'u(r')dr' \tag{5.27}$$

lower limit chosen to satisfy condition of symmetry w(0)=0

(5.26) into (5.27):

$$w(r) = -\frac{iAK}{r}\frac{r}{\alpha}J_1(\alpha r) - \frac{iK^2}{r\omega}\frac{Eh\delta}{\rho R_0^2}\frac{r^2}{2} + \frac{iK\sigma}{r\alpha R_0}A\frac{r^2}{2}J_1(\alpha R_0) \qquad (5.28)$$

Application of boundary conditions (5.17) and (5.18) to the velocities u and w and replacement of S by (5.21) lead to homogeneous equations for the unknowns δ and A:

$$\delta\left[\frac{\omega}{K}\frac{\sigma}{R_0} - \frac{K}{\omega}\frac{Eh}{\rho R_0^2}\right] - A\left[J_0(\alpha R_0) + \frac{i\alpha\omega\mu}{BhK^2}J_1(\alpha R_0) - \frac{\sigma}{\alpha R_0}J_1(\alpha R_0)\right] = 0 \qquad (5.29)$$

$$\delta\left[1 - \frac{K^2}{\omega^2}\frac{Eh}{2\rho R_0^2}\right] - A\left[\frac{K}{\omega\alpha}J_1(\alpha R_0) - \frac{K\sigma}{2\omega\alpha}J_1(\alpha R_0)\right] = 0 \qquad (5.30)$$

The solution to this set of equations exist if and only if the determinant of coefficients is equal to zero.

$$\left[1 - \frac{K^2}{\omega^2}\frac{Eh}{2\rho R_0}\right]\left[J_0(\alpha R_0) + \frac{i\alpha\omega\mu}{BhK^2}J_1(\alpha R_0) - \frac{\sigma}{\alpha R_0}J_1(\alpha R_0)\right] - \left[\frac{\omega}{K}\frac{\sigma}{R_0} - \frac{K}{\omega}\frac{Eh}{\rho R_0^2}\right] * \left[\frac{K}{\omega\alpha}J_1(\alpha R_0) - \frac{K\sigma}{2\omega\alpha}J_1(\alpha R_0)\right] = 0 \qquad (5.31)$$

This can be written in a more convenient form:

(5.32)

$$\left[\frac{K^2}{\omega^2}\frac{Eh}{2\rho R_0}\right]^2\left[2\alpha R_0\frac{J_0(\alpha R_0)}{J_1(\alpha R_0)} - 4\right] + \frac{K^2}{\omega^2}\frac{Eh}{2\rho R_0}\left[4\sigma - 1 - 2\alpha R_0\frac{J_0(\alpha R_0)}{J_1(\alpha R_0)}\right] + (1-\sigma^2) = 0$$

This equation must be solved for K^2/ω^2. The phase velocity and damping factor will then be determined by respectively the real and imaginary part of $K/\omega=(K_1+iK_2)$

This is complicated due to the fact that α and Bessel functions are complex quantities. In general this have to be solved numerically, but for certain restricted ranges it is possible to derive results in analytical form.

The two cases : i) Small viscosity, ii) Large viscosity or low frequency

Small Viscosity:

The first case of small viscosity is more precisely, the case $R_0(\omega\rho/\mu)^{1/2} >> 1$. This approximation is equal to demanding boundary layer much smaller than the radius of the streamer. Note that this might violate the condition $R/\lambda << 1$. The restriction implies $|\alpha R_0| >> 1$. This means that asymptotic expansions of Bessel functions for arguments $>> 1$ can be used. This results in :

$$\frac{J_0(\alpha R_0)}{J_1(\alpha R_0)} \sim -i + \left(\frac{1}{2\alpha R_0}\right) \tag{5.33}$$

Substituting this into (5.32) and solving approximately by retaining only terms necessary to give answer correct to order $|1/\alpha R_0|$. The two roots are obtained:

$$\tau_1 = \frac{K^2}{\omega^2}\frac{Eh}{2\rho R_0} = 1 + \frac{i}{\alpha R_0}\left[2 - 2\sigma + \frac{\sigma^2}{2}\right] \tag{5.34}$$

$$\tau_2 = \frac{K^2}{\omega^2}\frac{Eh}{2\rho R_0} = \frac{i(1-\sigma^2)}{2\alpha R_0} \tag{5.35}$$

The second root is impossible due to the phase velocity approaches infinity as μ approaches zero. The first root leads to the following formula for phase speed:

$$c = \frac{\omega}{K_1} = \pm\left[\frac{Eh}{2\rho R_0}\right]^{\frac{1}{2}}\left[1 - \left(1-\sigma+\frac{\sigma^2}{4}\right)\frac{1}{R_0}\left(\frac{\mu}{2\rho\omega}\right)^{\frac{1}{2}}\right] \tag{5.36}$$

$$K_2 = \pm\omega\left[\frac{2\rho R_0}{Eh}\right]^{\frac{1}{2}}\left[\left(1-\sigma+\frac{\sigma^2}{4}\right)\frac{1}{R_0}\left(\frac{\mu}{2\rho\omega}\right)^{\frac{1}{2}}\right] \tag{5.37}$$

This is the relevant approximation for breathing waves in streamer sections.

The Phase speed in equation (5.36) and damping factor K_2 in equation (5.37) is plotted in fig.5.2 below (ref.Appendix E1):

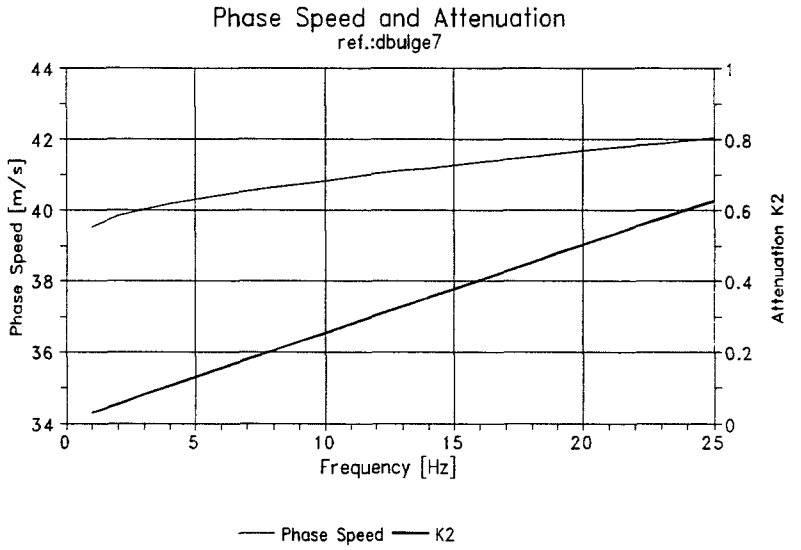

Figure 5.2 Phase Speed $c(\omega)$ and Attenuation $K_2(\omega)$ ref. equations (5.36) and (5.37)

Calculation of group speed:

The group speed $c_g = d\omega/dk$ can be calculated from the phase speed. The group speed for the low viscosity case is shown below. Equation (5.36) can be written in a more convenient form before derivation:

$$F_1 \omega^{-\frac{1}{2}} = 1 - \frac{\omega}{k} F_2 \tag{5.38}$$

$$F_2 = \left[\frac{Eh}{2\rho R_0}\right]^{-\frac{1}{2}} \quad , \quad F_1 = \left[\left(1-\sigma+\frac{\sigma^2}{4}\right)\frac{1}{R_0}\left(\frac{\mu}{2\rho}\right)^{\frac{1}{2}}\right] \quad , \quad F = \frac{F_2}{F_1} \tag{5.39}$$

$$-\frac{1}{2}\frac{d\omega}{dk}\omega^{-\frac{3}{2}} = -\frac{F}{k}\frac{d\omega}{dk} + \omega\frac{F}{k^2} \tag{5.40}$$

Multiplying equation (5.40) with k^2 and rearranging gives:

$$C_g = \frac{d\omega}{dk} = \frac{C_p}{1 - \frac{1}{2C_p\sqrt{\omega F}}} \tag{5.41}$$

For high frequencies, the phase speed is approximately equal to the group speed: $C_p \approx C_g$
For low frequencies, the group speed exceeds the phase speed: $C_g > C_p$.

Large viscosity or low frequency:

Consider the case: $R_0(\omega\rho/\mu)^{1/2} << 1$.

The condition can be satisfied by making ω as small as necessary for fixed R_0 ,ρ and μ.
The restriction $R/\lambda << 1$ is strengthen by this procedure.

Approximating the Bessel functions in (5.32) by the two first terms in a power series expansion for small arguments of the Bessel functions.

$$c = \frac{\omega}{K_1} = \pm \left[\frac{Eh}{2\rho R_0}\right]^{\frac{1}{2}} R_0 \left[\frac{\omega\rho}{\mu}\right]^{\frac{1}{2}} \frac{1}{(5-4\sigma)^{\frac{1}{2}}} \tag{5.42}$$

$$K_2 = \pm\omega\left[\frac{2\rho R_0}{Eh}\right]^{\frac{1}{2}} \left[(5-4\sigma)^{\frac{1}{2}} \frac{1}{R_0}\left(\frac{\mu}{\rho\omega}\right)^{\frac{1}{2}}\right] \tag{5.43}$$

This solution has not been applied in the later modelling of breathing waves described in section 5.3. The condition R/δ is calculated in appendix E1, when using the other approximation (equation (5.36) and (5.37)). For higher viscosity and smaller tube diameter, the present approximation resulting in equation (5.42) and (5.43), might be a better approximation (dependent on condition testing).

5.2 Fluid Loading

The effect of fluid loading on a long circular cylindrical body of which the distribution of normal surface velocity is harmonic in both axial and circumferential directions is given in ref.[16]. The cylinder surface specific acoustic impedance associated with a specific distribution of surface velocity. This radiation impedance is given by:

$$z_{rad} = \frac{-j\omega\rho_0 H_n[(k^2-k_z^2)^{\frac{1}{2}}R_0]}{(k^2-k_z^2)^{\frac{1}{2}}\dot{H}_n[(k^2-k_z^2)^{\frac{1}{2}}R_0]} \tag{5.44}$$

When the axial wavenumber k_z exceeds the acoustic wavenumber $k=\omega/c$, the argument of the Hankel function can be replaced by a modified Hankel function of real argument:

$$K_n(x) = \frac{\pi}{2} j^{n+1} H_n(jx) \tag{5.45}$$

When $k_z > k$, the radiation impedance is given to be purely imaginary:

$$\begin{aligned} z_{rad} &= -j\omega\rho_0 R_0 \ln[(k_z^2 - k^2)^{\frac{1}{2}}R_0] \quad , n=0 \ , (k_z^2 - k^2)R_0^2 \ll (2n+1) \\ z_{rad} &\simeq j\omega\rho_0 \frac{R_0}{n} \quad , n\geq 1 \ , (k_z^2 - k^2)R_0^2 \ll (2n+1) \end{aligned} \tag{5.46}$$

The radiation impedance is approximately zero when: $(k_z^2-k_2)^{1/2}R_0 >> n^2+1$

The different circumferential modes are indicated by n. The mode n=0 is called the breathing mode. This mode is identical to the breathing wave mode in streamer sections. From equation (5.46) it is seen that the radiation impedance for this mode is purely imaginary. The impedance represents a purely mass like fluid reaction. This extra mass like impedance can be introduced into the model for breathing waves. At the outer surface of the tube the normal stress is related to the displacement by an impedance matrix ref.[3].

This fluid loading has not been included in the model at the present time.

5.3 Modelling of Transfer Functions in Hydrophone Array Configuration

This is an **overview of the necessary steps** when modelling transfer functions between sensors/hydrophones in a hydrophone array:

1) Measurements of viscoelastic behavior for streamer skin in section 3.3. Complex Young's modulus measured for extensional waves in a bar sample of the tube material:

$$E^*(\omega) = E'(\omega) + jE''(\omega) \qquad d(\omega) = \frac{E''(\omega)}{E'(\omega)} \tag{5.47}$$

2) Polynomial Least Squares Fit of Young's Modulus (ref. fig.3.13 and fig.3.14).

3) Modelling of the breathing wave mode in an oil-filled viscoelastic tube (ref. section 5.1). Dispersion relation and frequency dependent attenuation in analytical form with design parameters (ref. equations (5.36) and (5.37)). The viscous part of attenuation has been increased with a factor of 2, for the additional area due to inner wire-bundle and spacer structure in the streamer section.

Phase speed:

$$c(\omega) = \frac{\omega}{K_1} = \left[\frac{E'(\omega)h}{2\rho R_0}\right]^{\frac{1}{2}} \left[1 - \left(1-\sigma+\frac{\sigma^2}{4}\right)\frac{1}{R_0}\left(\frac{\mu}{2\rho\omega}\right)^{\frac{1}{2}}\right] \tag{5.48}$$

Damping:

$$K_2(\omega) = \omega\left[\frac{2\rho R_0}{E'(\omega)h}\right]^{\frac{1}{2}} \left[\left(1-\sigma+\frac{\sigma^2}{4}\right)\frac{2}{R_0}\left(\frac{\mu}{2\rho\omega}\right)^{\frac{1}{2}} + \frac{E''(\omega)}{2E'(\omega)}\right] \tag{5.49}$$

4) Phase speed and attenuation as a function frequency ref. Appendix E1.

5) Transfer functions between hydrophones and sensors. Wave propagation model with dispersive wavenumber and attenuation coefficient ref. Appendix E2.

A description of the physical layout for the hydrophone array can be seen in fig.5.3 on next page. The breathing waves P1 and P2 are travelling from the sources (connectors) towards the hydrophones. Modelling of transfer function for the simple case with one source from the end in the layout for the 12 meter section can be seen in Appendix E2.

Note: Functions of space and frequency (x,ω) is equivalent to index i,n in Mcad files .

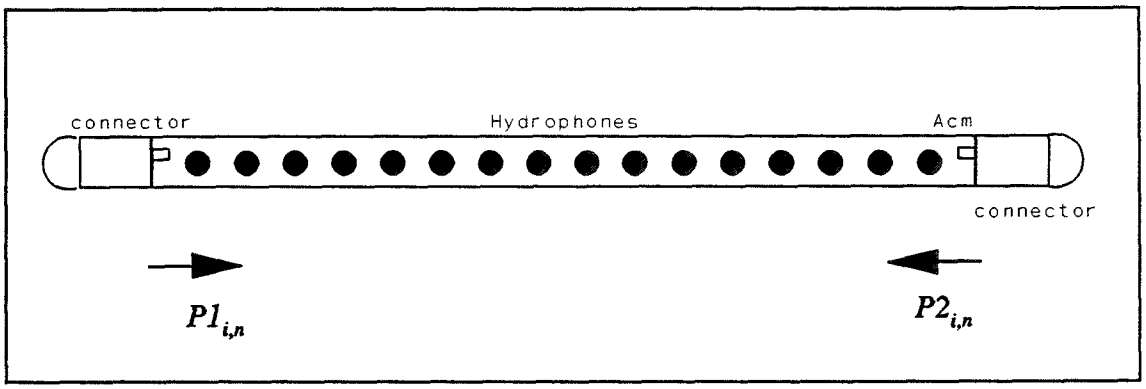

Figure 5.3 Layout for the hydrophone array

$$P1_{i,n} = Ae^{-d_n x_i} e^{j[\omega_n t - k_n x_i]} \tag{5.50}$$

$$P2_{i,n} = Be^{-\beta L} e^{-[d_n|L-x_i|]} e^{j[\omega_n t - k_n[x_i - L] - ks_n L]} \tag{5.51}$$

L is the length between connectors, ks_n and β is respectively the wave number and attenuation in the stress-wire: k_n and d_n is respectively the wavenumber and attenuation for the breathing wave mode. The two sources (connectors) are connected trough the wave mode in the stress-wire. The above model can be extended to more than two sources.

The noise signal on a hydrophone in position i is the sum:

$$P_{i,n} = P1_{i,n} + P2_{i,n} \tag{5.52}$$

If several hydrophones are connected in a group, the noise signal is:

$$G_n = \sum_{i=1}^{N} P_{i,n} \tag{5.53}$$

The transfer function from one sensor to a group of hydrophones is then:

$$H_n = \frac{G_n}{P_{i,n}} \tag{5.54}$$

The predicted transfer functions developed by modelling as described above, will be compared to measurements in experiments with a 12 meter hydrophone section in chapter 6.

6.0 EXPERIMENTS WITH THE 12 METER STREAMER SECTION

In seismic data acquisition, the length of the seismic cable (streamer) is normally 3-4 km long. The streamer consists of 100 meter long hydrophone sections with groups of hydrophones normally of 12 meter length. The generation of breathing waves in the hydrophone sections is described in chapter 1 and 5.

In this project the goal has been: i) Modelling of breathing waves (noise) and comparing to measurements, ii) Reduction of noise by adaptive noise cancelling. The experiments were done during my one year stay at the Technical University of Denmark (DTH). A short streamer section was brought down to Copenhagen for this purpose.

It is obviously difficult to set up laboratory experiments to study noise generated by vibrations in the streamer when dealing with apertures of this order. Nobody was too keen on handling a standard 100 meter streamer section in the experiments. Based on previous measurements and simple models, we decided that it would be possible to do the experiments with a 12 meter long hydrophone section. This length was certainly difficult enough to handle in vertical experiments.

6.1 The 12 Meter Experimental Section

Wiring diagram and layout drawings for the 12 meter experimental section are enclosed in Appendix F1.

The basic design of the 12 meter section was based on the digital streamer Nessie-3, which normally comprises 100 meter long sections. The hydrophone groups are formed by 12 in-line hydrophones connected in parallel, with spatial tapering and overlap. The experimental 12 meter section was built with 24 hydrophones with 0.5 meter spacing, individually wired to a Nessie-3 type connector. In addition to the hydrophones, two B&K 4370 accelerometers were installed inside each end of the section on the connector bulkhead.

A 15 meter long lead-in cable with waterproof connector was used for the experiments. A special tail-piece and front clamping were prepared for mechanical termination in the experimental setup. The equipment was built and prepared at Fjord Instruments in Bergen during the period of theoretical studies at University of Bergen in the beginning of the NIFU-31 project. Together with equipment for oil filling, the 12 meter section was transported down to DTH in Copenhagen for the experiments during my stay there.

6.2 Experiments in Air

Modelling of transfer functions for the breathing wave mode in the hydrophone sections are based on: measurements of viscoelastic properties of the streamer skin and the theoretical model described in respectively chapter 3 and chapter 5.

From the work with the model it was found that the fluid-loading due to the media (sea-water) around the streamer can be regarded as a mass-load for the breathing mode. That is, only a minor influence on the dispersion relation in the low frequency seismic band can be expected. According to equation (5.46) the fluid loading should have negligible effect on the damping.

At first the predicted transfer functions by modelling were compared to real measurements of breathing waves from sea tests. It turned out to be difficult due to the fact that the dataset is produced by natural excitation in a limited frequency band, and without controllable source excitation. Interference between several sources especially at low frequency and excitation essentially only at low frequencies makes the comparison difficult. In order to compare the theoretical model with measurements of breathing waves for a more well-known and controllable excitation over a wider frequency band, we decided to make an experimental setup with excitation from one end by a controllable vibrator.

A big vibrator (B&K4801T body and B&K4812 exciter head) was available for this purpose at the Department of Industrial Acoustics at DTH. The dynamic rated force (sine peak) is 445 N. The air-cooled vibrator has a direct 380 V power supply, and is controlled by a separate power amplifier B&K2707.

The weight of the vibrator is 88 kg, which makes it relatively difficult to handle. The unit is not waterproof, so it was not possible to use it in water. We decided to do the first measurements in air and compare with predicted transfer functions by modelling.

The normal operation of the streamer is horizontal at 10 meters depth. We tried to make a horizontal setup with the one end connected to the vibrator, and the other end fixed to a concrete pillar. A streamer segment has a strong in-line tension in normal operation due to the total length of the streamer is in the order of 3 km. There is a global wave propagation in the steel members inside the section generating the local breathing wave mode at discontinuities like connectors. We have focused on the local breathing wave mode in this project.

It turned out to be difficult to excite the breathing wave mode in a controlled manner in horizontal setups in air. It was not possible to generate the breathing wave mode without exciting other noise modes, like stress-members rattling against the tube wall.

Different horizontal setups were tried:

i) The 12 meter section at 1 meter above the floor mounted between two solid pillars in the basement. The streamer section was stretched by a manual winch.

Problem: The section was hanging in a slope on the middle and it was difficult to excite the connector to generate the breathing waves with the vibrator. Tried to excite with impulse (hitting from one end) with poor results.

ii) Section on the floor, one end connected to the vibrator and other end free. Assuming small effect of contact with floor.

Problem: When the stress-members (steel wires inside) are without tension, they generate noise in contact with the tube-wall.

After these exercises, the strategy was at least more clear. The section needed at least a tension, enough to avoid the stress-members to be in contact with the tube wall during vibration. The hydrophone section should be connected directly to the vibrator, and the oil-filled tube should be free, without influence from the surroundings in the setup.

Hanging the 12 meter section vertically:

The solution to the problems with the horizontal setup was to hang the section vertically from the 3. floor in the stairways down to the basement. The vertical setup can be seen in fig.6.1. Some pictures from the setup can be seen in appendix F2.

At first this experimental setup might seem to very far from the realistic case with a horizontal section in balance at 10 meter depth. There is a vertical pressure gradient in the section when hanging like this, and no fluid load from surrounding water. Based on the measurements of streamer skin properties in chapter 3 and the breathing wave model in chapter 5, this setup will obviously have some effect on the resulting measurements. The polyurethane material in the skin is a nonlinear material. Due to the pressure gradient, there will be a prestretch gradient in the skin going down the section. The effect is an increasing Young's modulus with distance.

This means that the breathing wave phase speed is some dependent on distance. This depends on nonlinearity in the material. Only some introductory measurements of the nonlinearity of the material was done in chapter 2. According to this information the effect of pressure-gradient can be expected to result in a total of 10% increase in phase speed going from top to bottom. When comparing transfer functions measured over short distances like 1 meter in these experiments, the influence should be in the order of 1 %.

The variation in gravity with height, has also been neglected in the model.

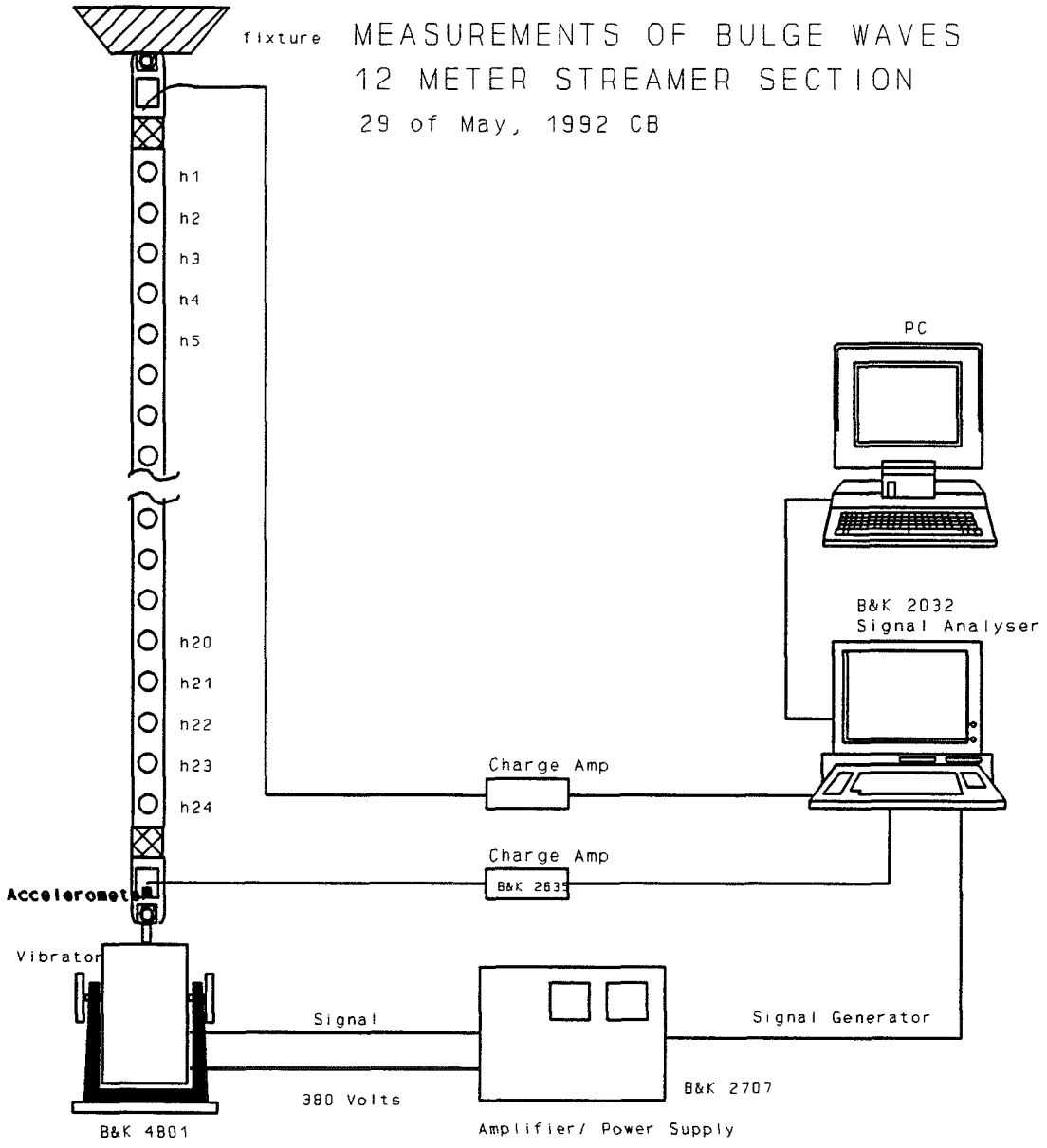

Figure 6.1 Experimental setup for generation and measurements of breathing waves in 12 meter streamer section hanging vertically.

Installation for experiments:

The section was filled with oil. The front end with the lead-in cable was fixed at the upper end to a winch. The section was lifted by the winch mechanism so that the tailpiece on the end-connector was in correct height to match a special made connection device on the vibrator piston. After adjustment and mechanical connection, the section was stretched by a dc offset control of the vibrator piston from the amplifier. The objective was to minimize contact between inside stress member structure and tube wall (the "rattle" effect). The actual value of the stress in the stress-members is not important for the local breathing wave mode.

An external accelerometer was mounted on the lower end-connector to measure the source vibrations. Two accelerometers are also installed, one in each side inside the hydrophone section. The hydrophones and inside accelerometers are wired to the connector at the upper end. The lead-in cable was hanging down into the basement and connected to the instruments. The hydrophones and accelerometers were connected to a rack of charge amplifiers of type B&K2635. Real time analysis was done by a signal analyzer B&K 2032.

First measurement of transfer functions and impulse response:

Excitation: pseudo random noise 1-50 Hz alt. 1-25 Hz
Adjusting vibration level to approximately 1 mg = 0.01 m/s^2

Transfer functions:

i) Between hydrophones
ii) Between accelerometer on connector and single hydrophones
iii) Between accelerometer and groups of hydrophones.

A good agreement was found between the measured transfer functions and the transfer functions predicted by modelling (ref.section 5.3).

Some signal analysis was done directly with the 2 channel FFT analyzer when running the vibrator.

The signals were recorded on tape for later analysis. Up to 7 channels were recorded simultaneously with common time base. Normally the two accelerometers, one in each end, and 4 single hydrophones were recorded. In some recordings, the hydrophones were grouped by connecting them in parallel. The recordings have been used both for comparing to model and in experiments with the adaptive noise cancelling system, which will be described in chapter 10.

6.3 Comparing Measurements to Modelling

The measurements of Auto Spectrum for the signal from the accelerometer on vibrator and the signal from hydrophone 21 can be seen in appendix F3. Some limited excitation at lower frequencies can be seen. This is due to the response of the vibrator.

The coherence was nearly 1.0 for all frequencies both for transfer functions between accelerometer to hydrophones and between hydrophones. As an example of measured coherence see appendix F4.

The vibrator was excited with pseudo random noise 0-25 Hz. The measured transfer function for the breathing wave mode between hydrophone H23 and H21 was measured and compared to the corresponding transfer function predicted by modelling (ref. section 5.3). The result can be seen in fig.6.2.

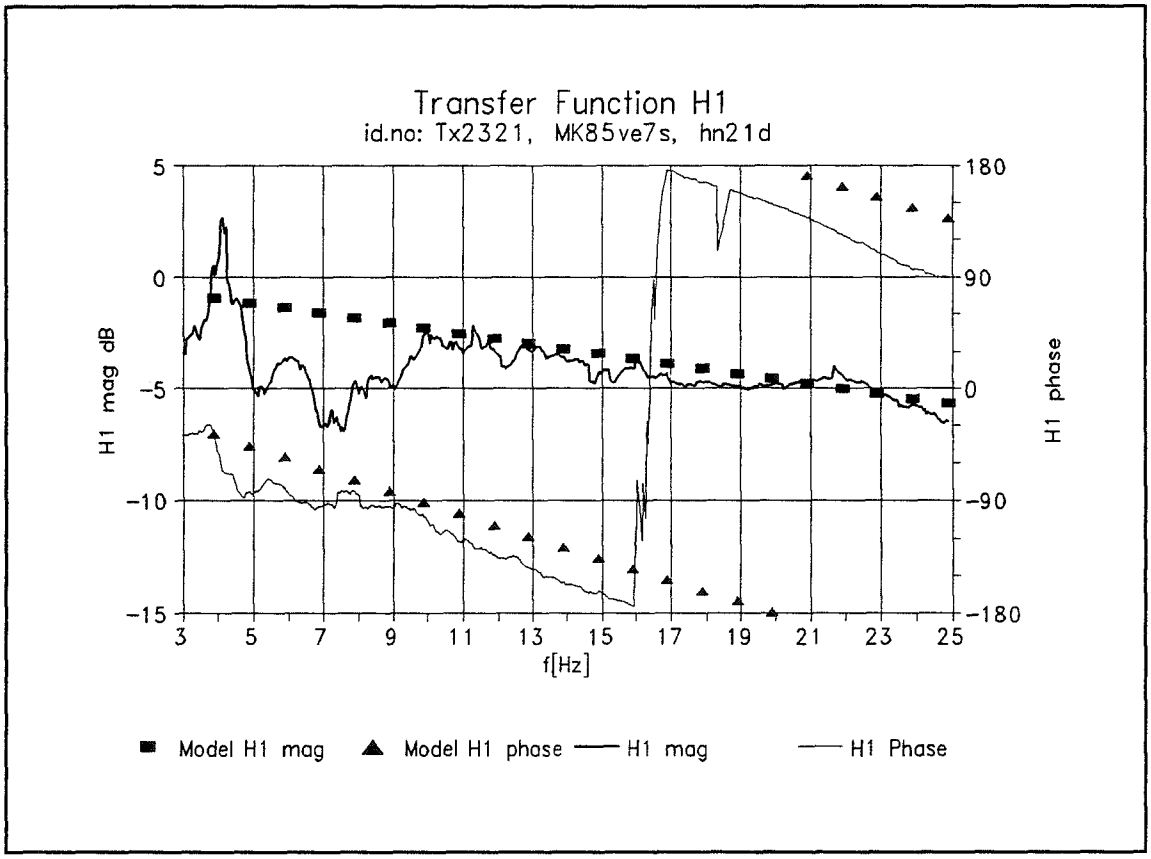

Figure 6.2 Transfer function for the breathing wave mode from hydrophone H23 to H21. Measured compared to predicted by modelling.

There is a good match between measured and predicted transfer function between the two hydrophones. However, the match in the low frequency part is not too good. This can be explained from interference between waves from lower end and waves from upper end of the 12 meter section. Note that the attenuation is approximately 1 dB/m at 3 hz and 6 db/m at 20 Hz. Due to the stronger attenuation at higher frequencies, we can expect to see the interference mainly at low frequency. A second source at the upper end was put into the bulge wave model, in order to show this effect.

The fixture at the upper end of the section is not perfect. Furthermore, the skin was touching the spacers inside and there was some air between the upper oil level and connector. Due to the above problems there are probably several more diffuse sources. The result of 2 sources in the model can be seen in fig.6.3. The interference between primary wave and additional sources seems to be a reasonable explanation for the deviation seen at low frequency when comparing measured and predicted response in fig.6.3.

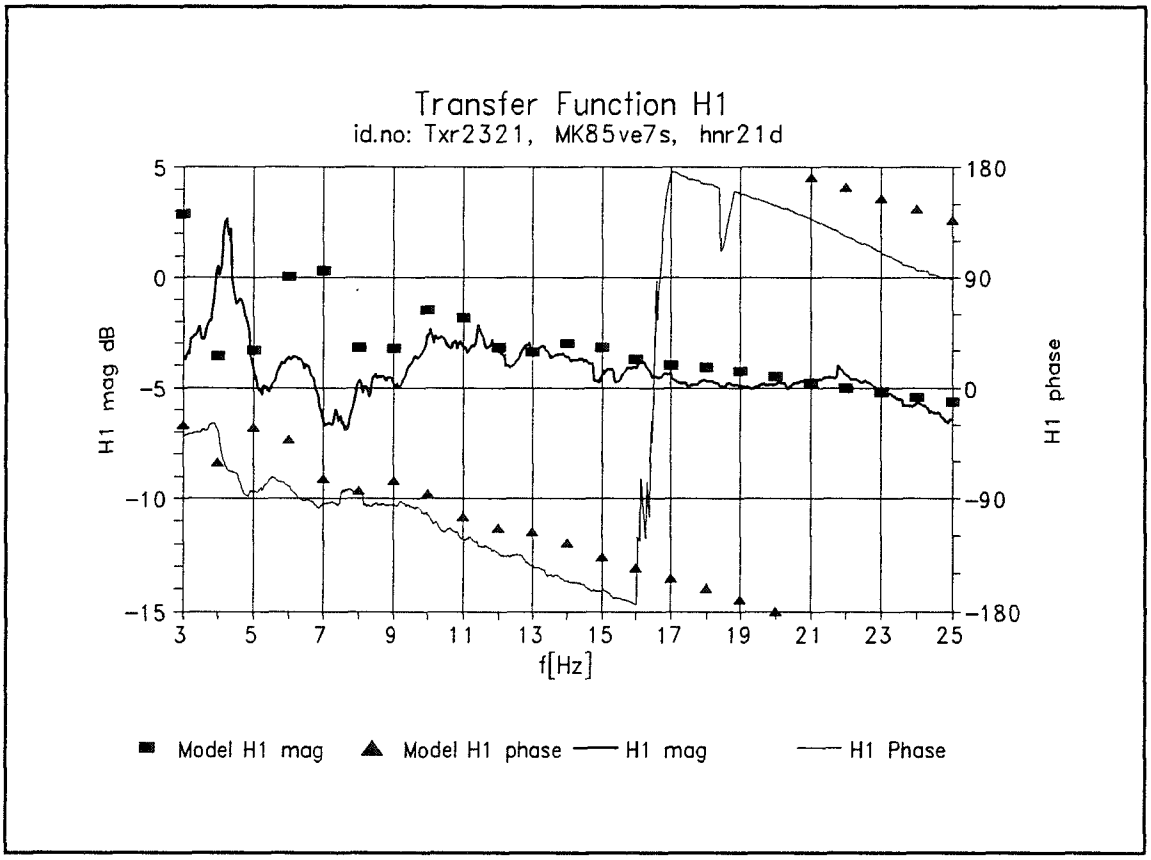

Figure 6.3 Transfer function for the breathing wave mode from hydrophone H23 to H21, with additional source at upper end. Measured compared to predicted by modelling.

The transfer function between the accelerometer on the lower connector at the vibrator head and to hydrophones H24,H23,H22 and H21 in a group can be seen in fig. 6.4. The match between the predicted and measured transfer function is good, except for offset in magnitude due to unknown conversion factor between connector acceleration and pressure wave in tube.

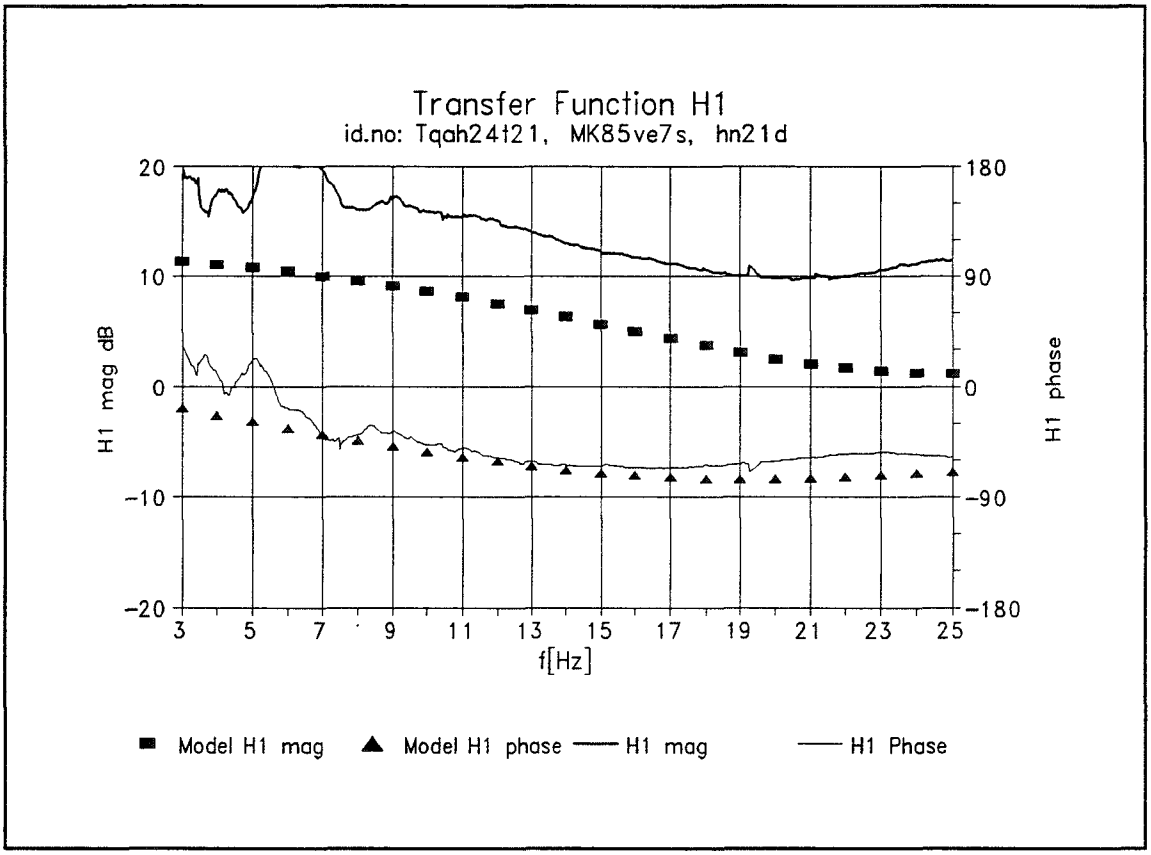

Figure 6.4 Transfer function for the breathing wave mode from accelerometer to hydrophone group (H24,H23,H22,H21). Comparing measured to predicted by modelling.

The interference seen at low frequencies can be explained in the same way as before. The interference at low frequencies is probably due to sources at the upper end of the section. The result of including a second source at the upper end in the model can be seen in fig.6.5

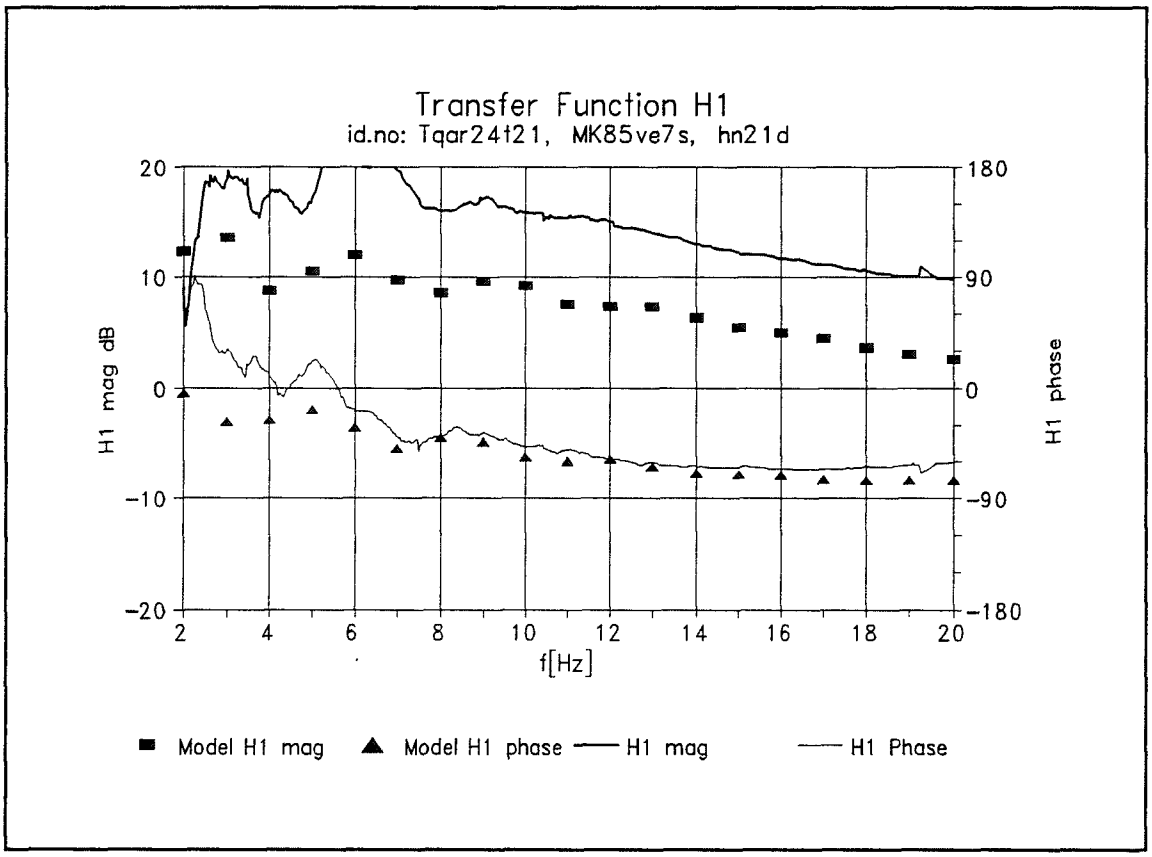

Figure 6.5 Transfer function for the breathing wave mode from accelerometer to hydrophone group (H24,H23,H22,H21), with additional source at upper end. Comparing measured to predicted by modelling.

The results from the experiments in this chapter, shows that the breathing wave model in chapter 5 gives a realistic description of propagation of breathing waves in streamer sections.

7.0 TOWING IN A WATER TANK

Some initial testing of the 12 meter section in a ship water tank was done at the Danish Maritime Institute DMI Ship Laboratory in Copenhagen. The purpose of this test was to investigate to what extent it was possible to simulate the operational towing conditions in an experimental setup in water. As described before the hydrophone sections are connected together, forming up to 4 km long streamer cables. It is only possible to simulate the same conditions to a certain extent, when towing a 12 meter section in a water tank. The mechanical terminations and flow of water will not be the same as in the real case.

In addition to the economical issue, the advantage of using a test tank is: easy access, repeatability and controlled environment. The company FI expressed a strong interest in the investigation of towing streamer sections in a long water tank.

Due to limited time in this project, only initial testing and signal analysis have been done, to see if this is a relevant method at all.

7.1 The water tank

The water tank is located at Danish Maritime Institute's Ship Laboratory in Copenhagen. The tank is filled with fresh water and the size is:

Length: 250 meter, Width: 12 meter, Depth: 6 meter

A 12 meter long and 12 meter wide measuring platform is moving on a railway on top of the tank. The platform can move at a steady speed along the tank up to 5 knots. At the end of the tank there is a wave machine, that can produce up to 0.7 meter high waves. The hydraulic/ mechanical wave machine is controlled by a computer, and waves can be shaped with desired characteristics to a certain extent.

The experimental setup for towing the 12 meter section at 1 meter depth in the 250 meter long water tank can be seen in fig.7.1. Some pictures from the experiment can be seen in appendix F2.

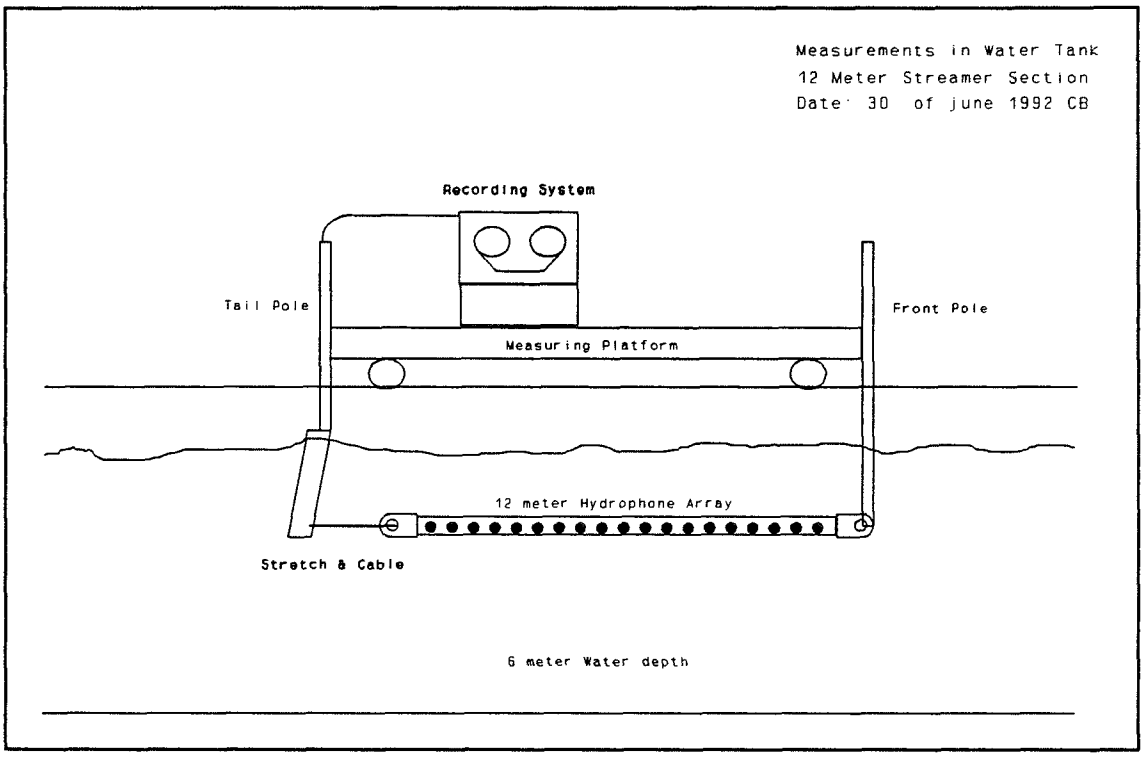

Figure 7.1 Setup for measurements with the 12 meter section in a water tank

7.2 Setup with the 12 meter section in the water tank

1) The 12 meter section was installed between two poles.

2) The two poles were prepared with mechanical connections for this purpose.

3) The tail pole was prepared with a streamlined profile at an angle with the pole, in order to minimize turbulence at this end.

4) The tail connector was connected to the tail pole via a nylon rope (damping element).

5) The lead in cable from the hydrophones and accelerometers was pulled through the tail pole up to the battery powered B&K charge amplifiers.

6) The signals from hydrophones and accelerometers were recorded on a Racal FM instrument tape recorder for later analysis.

7) The platform was moving up to a speed of 5 knots. The signals from hydrophones and accelerometers were recorded.

The transfer functions for the breathing wave mode were measured in the setup with the 12 meter section hanging down to the vibrator, described in chapter 6. It would be a natural extension of the experiment to move everything into water. But the vibrator is not waterproof and alternative methods of excitation with the vibrator on the platform would be very complicated.

The setup was then based on natural excitation by vibrations induced by turbulence around the front pole when towing. A more streamlined tail pole with stretch connection to tail of section was used in order to reduce the number of sources.

A more controllable excitation over a broader frequency range would be desirable for the purpose of comparing the measurements with the model. This is partly due to interference seen at low frequency and lack of excitation at higher frequencies with natural excitation in a setup like the one in the water tank.

Measurements in the water tank:

1) Towing the section in the tank without surface waves up to 5 knots

2) Towing the section up to 5 knots while generating surface waves of 0.7 meter height in the tank.

7.3 Analysis of Measured Signals

We experienced quite a lot of 50 Hz power noise. The lead-in cable to the hydrophones is pulled along most of the platform and electromagnetic interference from the power supply can be expected.

The background noise increased with the activity of different machinery on the platform.

Measurement of background noise level can be seen in fig.7.2. This was recorded when standing still at start position.

The 12 meter streamer section was then towed up to a speed of 2.5 m/s (5 knots). The recorded signals have been analyzed on the B&K2032 FFT analyzer. Some results can be seen below. The Auto Spectrum PSD for hydrophone H21 and H23 can be seen in fig.7.3.

The software package QPRO 4.0 has been used for presentation of the analyzed frequency domain signals. The standard option in QPRO: weighted Moving Average (MA) with period 12 has been applied to smooth the data-set for presentation. The peaks and main structure of the spectrum are preserved when using the weighted MA process. The measurements are presented in fig.7.2 - fig.7.7

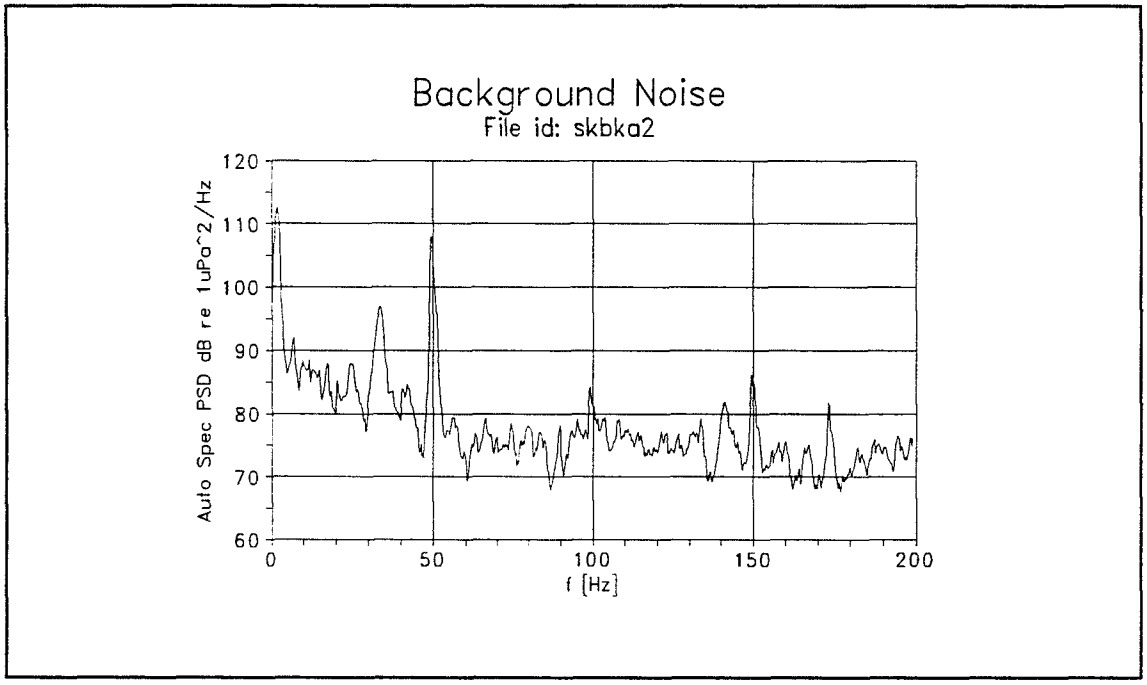

Figure 7.2 Background Noise on hydrophone H23, Auto Spectrum PSD.

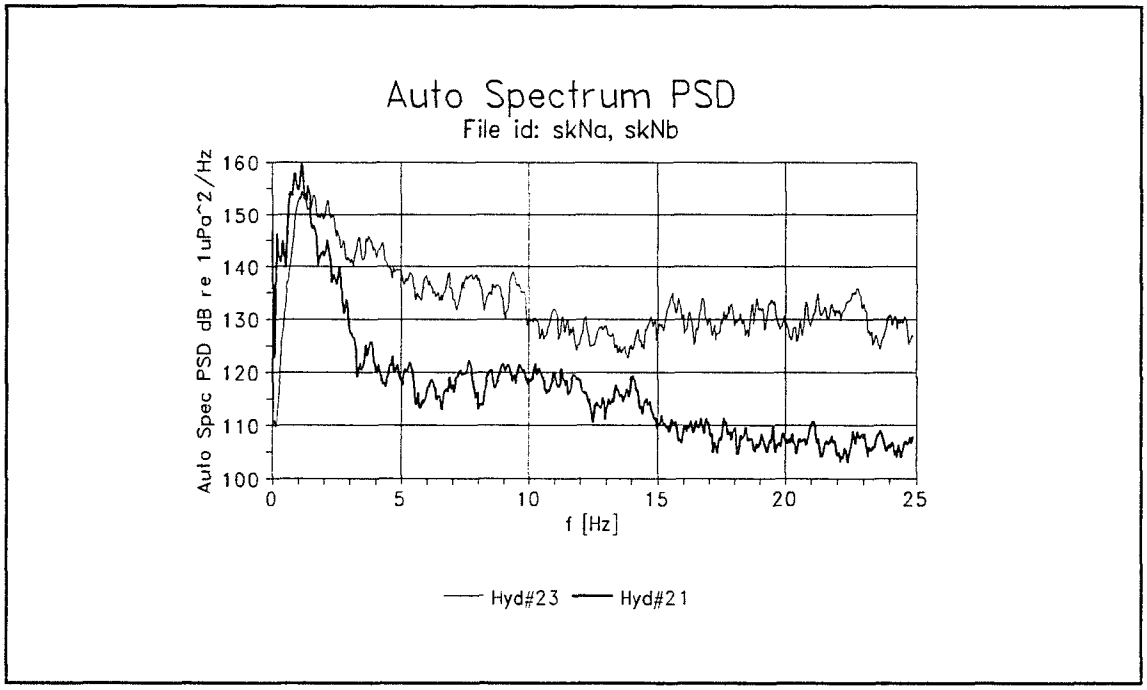

Figure 7.3 Towing 12 meter streamer section in water tank at speed 2.5 m/s. Auto Spectrum PSD for hydrophones H23 and H21.

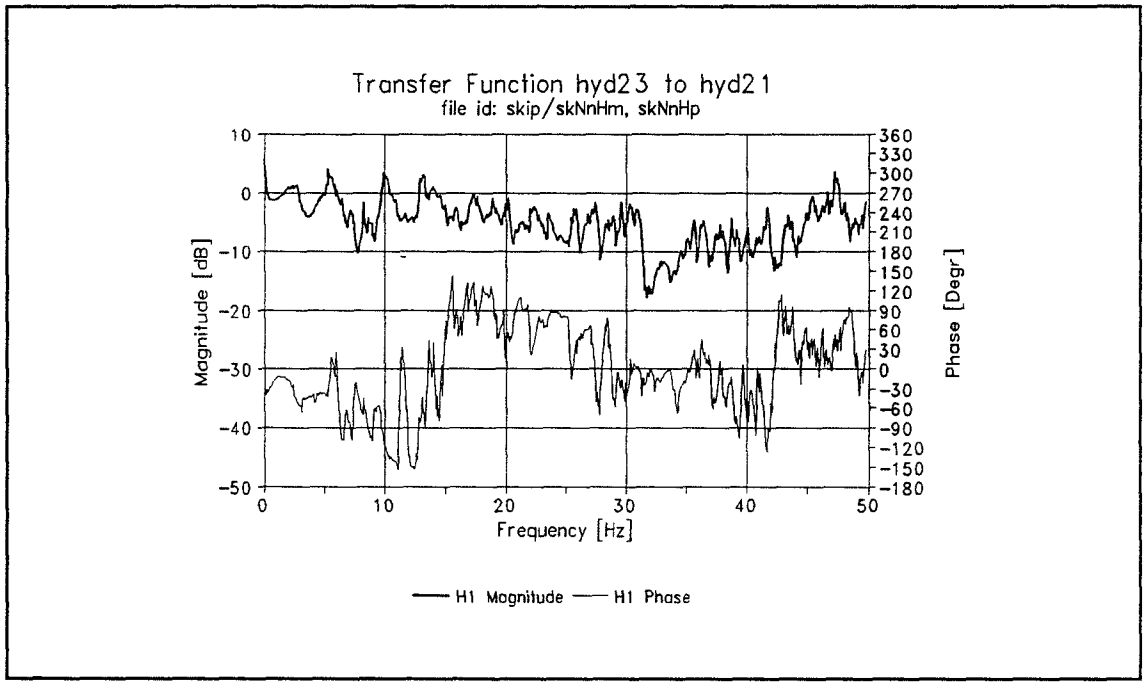

Figure 7.4 Transfer function from hydrophone H23 to H21. Towing 12 meter section in water tank at speed 2.5 m/s.

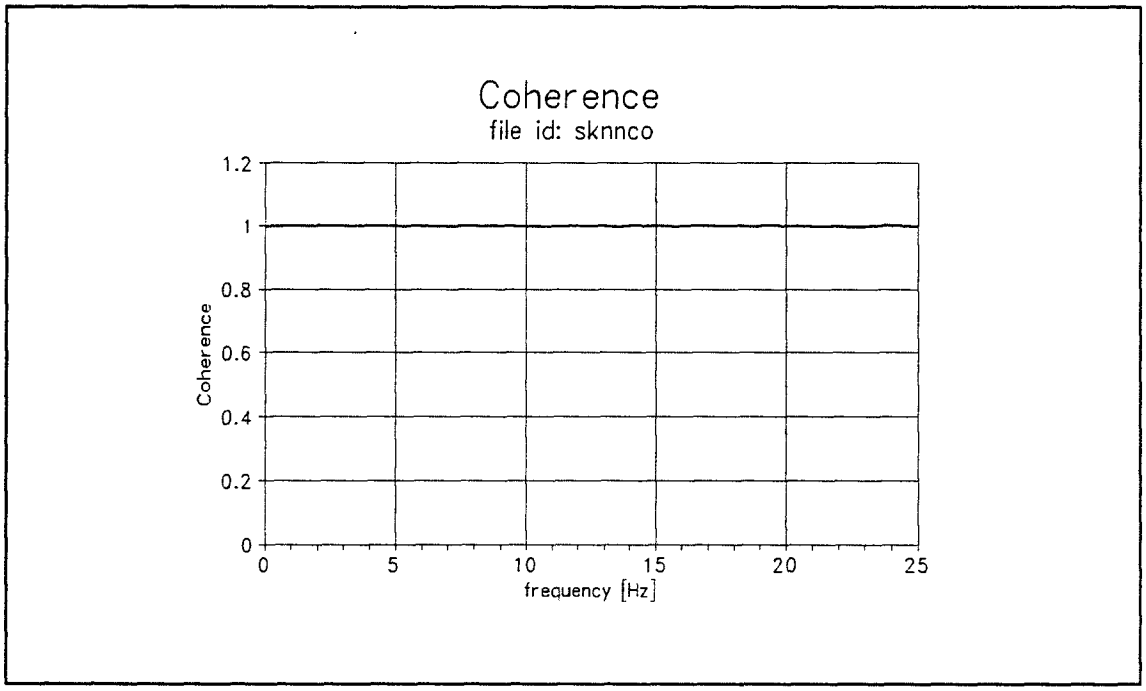

Figure 7.5 Coherence between Hydrophone H23 and H21. Towing 12 meter section in water tank at 2.5 m/s

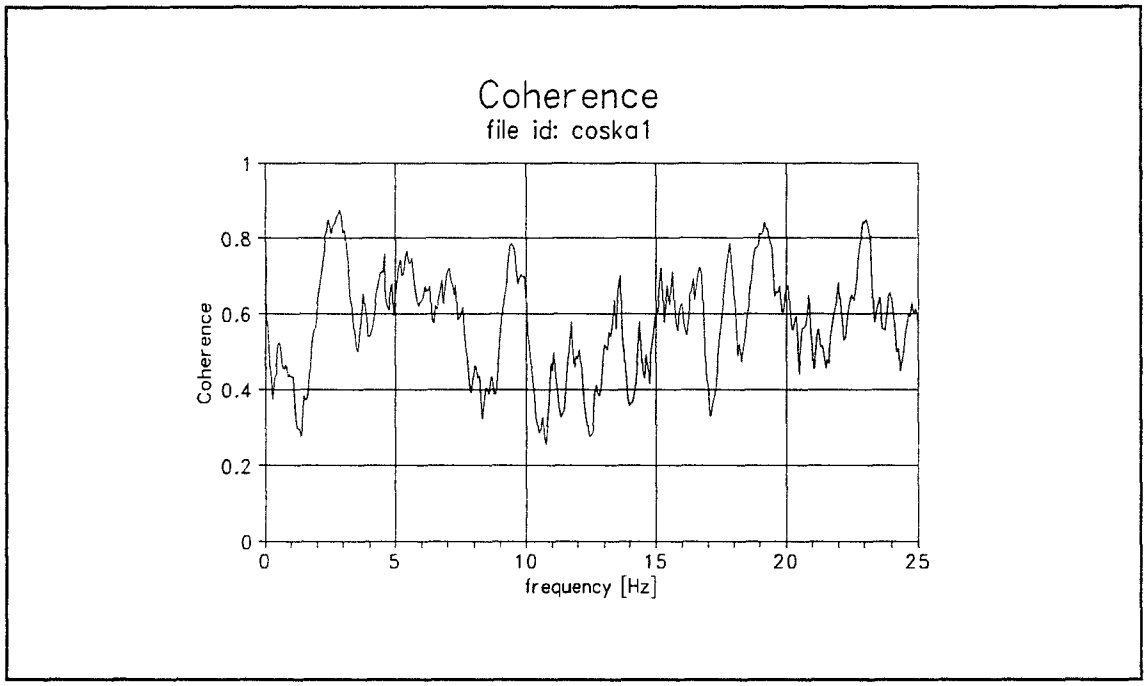

Figure 7.6 Coherence between external accelerometer on pole and Hydrophone H23. Towing 12 meter section in water tank at speed of 2.5 m/s.

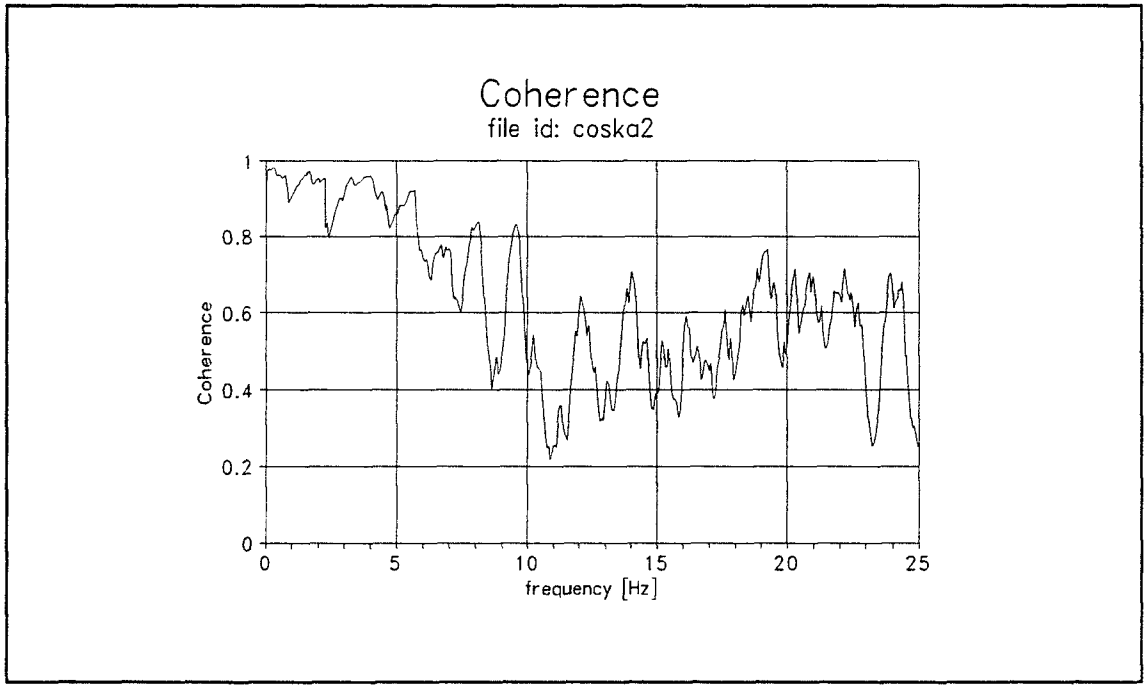

Figure 7.7 Coherence between internal accelerometer on connector bulkhead and H23. Towing 12 meter section in water tank at speed of 2.5 m/s.

The transfer function from hydrophone H23 to H21 can be seen in fig.7.4. The coherence between hydrophone H23 and H21 is close to 1.0 for all frequencies in fig.7.5. The coherence between the accelerometer on the front pole and hydrophone H23 shown in fig.7.6 is poor. The coherence between the internal accelerometer mounted on the connector bulkhead and hydrophone H23 is shown in fig.7.7. The coherence is good below 7 Hz and then decreasing to a level around 0.5.

Considerable flow noise can be expected in this setup. A front turbulent eddy will be generated as the section is moving forward. This front eddy will have an strong effect on the first hydrophones, and will be seen in addition to the breathing waves generated by the piston like movement of the connector.

The accelerometer will only measure information coherent with the breathing waves. The hydrophones will measure the noise due to breathing waves and an additional signal component due to the turbulent eddies convecting along the streamer section. The breathing waves are generated by natural excitation mainly at low frequencies. The total noise level is dominated by the breathing waves at lower frequencies. This should explain why the coherence in fig.7.7 is good only at lower frequencies, and that the coherence between hydrophones in fig.7.5 is good for all frequencies.

The poor coherence between the external accelerometer on the pole and hydrophone H23 in fig.7.6, indicates that this position do not give a good representation of the noise sources.

The above experiments show that its possible to generate the breathing waves in this setup. Realistic measurements can however not be expected due to flow conditions and short section. With improvements to the experimental setup and noise conditions in the tank, it might be a method to consider for comparing sections of different design under approximately same conditions.

8.0 ADAPTIVE NOISE CANCELLING THEORY

The background theory ref.[29] & [30] for the adaptive noise cancelling system implemented in the project will be described in this chapter. The theoretical description leads up to the Normalized LMS algorithm with recursive power estimate in section 8.3.

The background theory for signal to noise ratio and signal distortion when the reference input contains a low level signal component, will be described in section 8.5. The expected noise reduction will be described briefly in section 8.6.

8.1 The Adaptive Linear Combiner

The adaptive linear combiner is fundamental to adaptive systems. The adaptive linear combiner is also known as a nonrecursive adaptive filter. The linear combiner is only linear for a fixed setting of the filter weights. The weights are a function of the input signal in the adaptive process. The operation of the adaptive filter is then nonlinear.

The adaptive linear combiner can be implemented both for the multiple input case and the single input case. The adaptive processor, implemented with adaptive linear combiner and unit delay elements can be seen in fig.8.1.

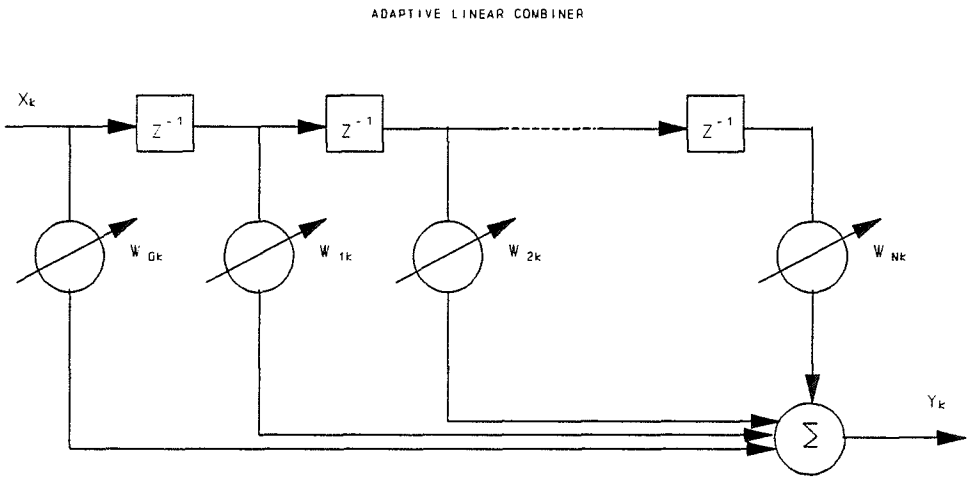

Figure 8.1 Adaptive linear combiner. Network with unit delay elements and adjustable filter weights.

It is convenient to use vector notation for description of operation of the adaptive linear combiner. The input signal vector can be either a multiple input or a single input case. The input signal will be interpreted as a single input in this chapter.

The input signal vector $\mathbf{X}_k$ is written as a transposed **T** row vector for convenient notation.

$$\boldsymbol{X}_k = [x_{0k}\ x_{1k}\ \ \ldots\ \ x_{Lk}]^T \tag{8.1}$$

The weight vector is defined:

$$\boldsymbol{W}_k = [w_{0k}\ w_{1k}\ \ \ldots\ \ w_{Nk}]^T \tag{8.2}$$

Note the unit delay elements in the linear combiner. It is easy to see that the linear combiner is equivalent to a convolution of the input signal with the weight vector.

The output signal is then:

$$y_k = \sum_{l=0}^{N} w_{lk} x_{k-l} \tag{8.3}$$

This relationship between the input and output signal can be expressed using vector notation:

$$y_k = \boldsymbol{X}_k^T \boldsymbol{W}_k = \boldsymbol{W}_k^T \boldsymbol{X}_k \tag{8.4}$$

The adaptive linear combiner will be used in a closed loop adaptive system. Fig.8.2 shows an adaptive system with performance feedback. A "training signal" or desired response signal d_k is assumed to be available. The adaptive system would of course not be necessary if this was the actual desired response.

The difference between the desired response and the output from the adaptive linear combiner ϵ_k is called the error signal or performance signal.

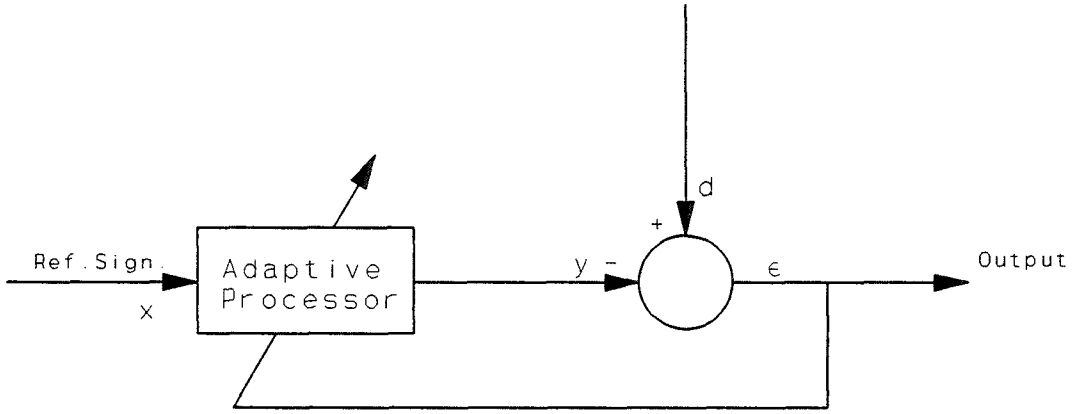

Figure 8.2 Adaptive system with performance feedback

The error signal is then:

$$\epsilon_k = d_k - y_k = d_k - W^T X_k \tag{8.5}$$

The weight vector of the linear combiner is optimized (adjusted) so that the output from the combiner y_k is as close as possible to the desired response d_k .

The adaptive process is normally some practical implementation of minimizing the mean-square value of the error signal.

The input signal $\mathbf{X}_k$, error signal ϵ_k and desired response d_k are assumed to be statistically stationary. The mean squared error is then:

$$MSE \doteq \xi = E[\epsilon_k^2] = E[d_k^2] + W^T E[X_k X_k^T] - 2E[d_k X_k^T] W \tag{8.6}$$

The mean squared error as a function of the filter-weights is called a performance surface.

The expected value of a product is the product of expected values only when the variables are statistically independent. The signals x_k and d_k are generally not independent.

The input correlation matrix is defined:

$$R = E[X_k X_k^T] = E\begin{bmatrix} x_{0k}^2 & x_{0k}x_{1k} & \cdots & x_{0k}x_{Lk} \\ x_{1k}x_{0k} & x_{1k}^2 & \cdots & x_{1k}x_{Lk} \\ \vdots & \vdots & \cdot & \vdots \\ x_{Lk}x_{0k} & x_{Lk}x_{1k} & \cdots & x_{Lk}^2 \end{bmatrix} \tag{8.7}$$

The cross correlation matrix is defined:

$$P = E[d_k X_k] = E[d_k x_{0k} \;\; d_k x_{1k} \;\; \cdots \;\; d_k x_{Lk}]^T \tag{8.8}$$

Equation (8.6) is a quadratic performance function of the weights in the vector W. The elements of W will be of first and second degree when equation (8.6) is expanded. The performance function is generally a hyperparaboloid, that is concave upwards. There is only a single global optimum and no local minima when the performance function is quadratic.

Gradient methods are normally used in the adaptive process to make the weight vector seek the minimum of the performance surface.

The gradient is obtained by differentiating the performance function with respect to each component in the filter vector.

$$\nabla \doteq \frac{\partial \xi}{\partial W} = \left[\frac{\partial \xi}{\partial w_0} \;\; \frac{\partial \xi}{\partial w_1} \;\; \cdots \;\; \frac{\partial \xi}{\partial w_N}\right] \tag{8.9}$$

The minimum Mean Squared Error is when the filter weight vector W is set to the optimal value W^* (the Wiener weight vector), where the gradient is zero.

$$\nabla = 0 = 2RW^* - 2P \quad , \quad W^* = R^{-1}P \tag{8.10}$$

R: input correlation matrix
P: cross correlation between primary and reference signal

In our application the quadratic performance function is unknown and no analytical description is available. Locations of points on the performance surface can be measured by averaging the squared error over a time period. A systematic procedure (method/algorithm) must be applied to search the performance function to find the optimum weight vector.

Several methods for searching the performance surface exist. For example Newton's method and the method of steepest descent. An estimate of the gradient is used to find the direction to the minimum of the performance surface. The methods are called descend methods.

8.2 The LMS Algorithm

A special estimate of the gradient of performance function that is valid for the adaptive linear combiner is used in the Least Mean Squared algorithm.

Other methods require an estimate of the gradient at each iteration, taking differences between estimated points on the performance surface.

Instead of estimating the gradient by taking short term averages of $E[\epsilon_k^2]$, the LMS algorithm is using ϵ_k^2 itself as an estimate of the gradient.

A gradient estimate is then available at each iteration:

$$\nabla_k = \begin{bmatrix} \frac{\partial \epsilon_k^2}{\partial w_0} \\ \cdots \\ \frac{\partial \epsilon_k^2}{\partial w_L} \end{bmatrix} = -2\epsilon_k X_k \tag{8.11}$$

The LMS algorithm is defined:

$$W_{k+1} = W_k - \mu\nabla_k = W_k + 2\mu\epsilon_k X_k \tag{8.12}$$

This is a steepest descent type of algorithm where the new weight vector W_{k+1} is calculated from the previous weight vector W_k with an adjustment in the opposite direction of the gradient. The simplicity of the LMS algorithm can be seen in equation (8.12).

It is easy to implement on a computer. The adjustment of the weight vector is just the product of the error signal (performance signal) and the input signal vector $\mathbf{X}_k$ multiplied with an adaption constant μ, which is controlling the rate of conversion.

Thus the LMS algorithm can be implemented without squaring, differentiation or averaging in a simple and efficient way.

It is possible to show ref.[29] that the LMS algorithm only converges for the following condition:

$$\frac{1}{\lambda_{max}} > \mu > 0 \tag{8.13}$$

Where λ_{max} is the largest eigenvalue of the eigenvalue matrix of $\mathbf{R}$. λ_{max} can not be bigger than the trace of $\mathbf{R}$.

From equation (8.7) tr[$\mathbf{R}$] is equal to $(L+1)E[x_k^2]$. That is $(L+1)$ times input signal power.

$$0 < \mu < \frac{1}{(L+1)(\textit{signal power})} \tag{8.14}$$

The adaptive process can be expected to be noisy, due to the fact that the weight vector is based on imperfect gradient estimate at each iteration .

8.3 Normalized LMS with Recursive Power Estimate

The normalized LMS algorithm ref.[30] can be used to overcome gradient noise amplification. The adaption constant is then normalized with the signal power:

$$W_{k+1} = W_k + \frac{\alpha}{a + \|X_k\|^2} \epsilon_k X_k \tag{8.15}$$

Convergent (stable) if :

$$0 < \alpha < 2 \tag{8.16}$$

W_k	:	Old Filter vector
W_{k+1}	:	New Filter vector
α	:	Normalized adaption constant, regulating speed and stability
a	:	Small value to avoid numerical difficulties

The increased computation requirements can be reduced by computing a recursive estimate of the signal power:

$$\pi_{k+1} = (1-\beta)\pi_k + N\beta x_k^2 \tag{8.17}$$

The normalized LMS with recursive power estimation:

$$W_{k+1} = W_k + \frac{\alpha}{a + \pi_k} \epsilon_k X_k \tag{8.18}$$

This algorithm is using one location of extra storage to compute signal power instead of using N locations to compute $X_k^T X_k$.

The averaging time is controlled by β. The time constant of the power averaging has a time constant of N samples if β is chosen:

$$\beta = 1 - \frac{1}{N} \tag{8.19}$$

8.4 Learning Curve for The LMS Algorithm

The curve of Mean Squared Error (performance signal) with iteration number k in the adaptive process is called a learning curve.

The adaption constant μ regulates the speed and stability of adaption.

The time constant of the learning curve ref.[29]:

$$\tau_{mse} \approx \frac{N+1}{4\mu tr[R]} \tag{8.20}$$

Misadjustment is a measure of how closely the adaptive process tracks the true Wiener solution. The misadjustment is shown to be ref.[29]:

$$M \approx \mu tr[R] \tag{8.21}$$

Note! The **misadjustment** is directly proportional to μ
The **time constant** is inversely proportional to μ

! There is a trade-off between the misadjustment and the rate of adaption.

8.5 Signal to Noise and Distortion

In a practical implementation of the adaptive Noise canceller, the reference input can contain a low level signal component in addition to the reference signal. Some important results will be described below: ref. [29] & Appendix H1.

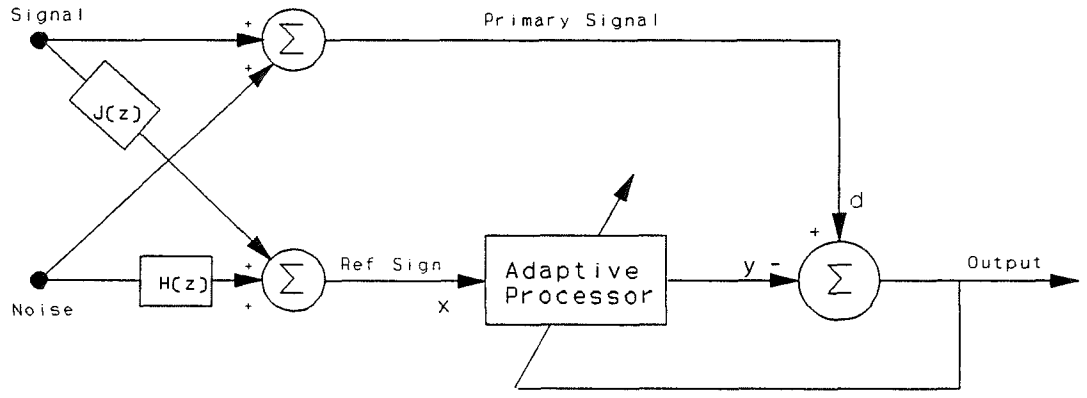

Figure 8.3 Adaptive noise cancelling system with reference input containing low level signal component in addition to reference signal.

Power inversion principle:

According to the results from Appendix H1, the output signal to noise density ratio is:

$$\rho_{out}(z) = \frac{1}{\rho_{ref}(z)} \tag{8.22}$$

Under the assumptions: unconstrained adaptive solution and noise in the primary and the input are mutually correlated.

The signal to noise density ratio at the output of the noise canceller is simply the reciprocal of the signal to noise density ratio at the reference input for all frequencies. **This is called power inversion.**

Signal distortion:

Another important result from Appendix H1 is the equation for signal distortion.

Using the equation for signal to noise density at the reference input:

$$D(z) \approx \frac{\rho_{ref}(z)}{\rho_{pri}(z)} \tag{8.23}$$

This result shows that signal distortion is low for high signal to noise ratio at the primary and low signal to noise ratio at the reference input.

Output noise spectrum:

The spectrum of output noise in terms of signal to noise ratio at the reference input:

$$\Phi_{output\ noise} \approx \Phi_{nn}(z)\,|\rho_{ref}(z)|\,|\rho_{pri}(z)| \tag{8.24}$$

This result shows that the output noise spectrum is proportional to the input noise spectrum. The second factor indicates low output noise spectrum for low signal to noise at the reference. The last factor shows that low signal level on the primary gives the best result.

The above results shows that the adaptive noise cancelling system can still work with a small signal component in the reference input.

8.6 Expected Noise Attenuation

In addition to the information originating from the noise source, the input signal (reference) to the adaptive filter also contain some stocastic noise.

It can be shown ref.[28] that the theoretical noise attenuation [dB] to be expected with the adaptive noise cancelling system is:

$$\delta L = 10\log\frac{1}{1-\gamma^2} \tag{8.25}$$

Where γ^2 is the coherence between the reference signal and the primary signal to the filter.

As an example, the theoretical noise attenuation for a coherence of $\gamma^2=0.9$ is 10 dB.

9.0 THE ADAPTIVE NOISE CANCELLING SYSTEM

This chapter will describe how adaptive noise cancelling is implemented to reduce noise-level, and thereby improving Signal to Noise ratio in seismic hydrophone arrays.

In this project, we have focused on reduction of noise due to breathing waves generated in the streamer section as described in chapter 1 and chapter 5.

The theory for adaptive noise cancelling described in chapter 8 is implemented in a system for seismic hydrophone arrays (streamer). Fig.9.1 shows how the adaptive noise cancelling principle is implemented for a hydrophone group (similar for a single hydrophone).

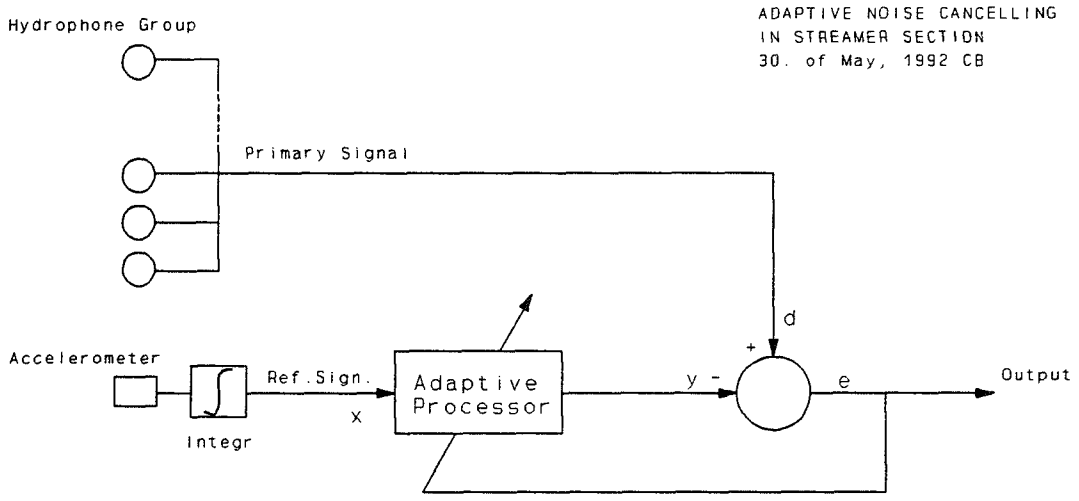

Figure 9.1 The adaptive noise cancelling system implemented for a hydrophone group in a seismic streamer.

The reference sensor is an accelerometer mounted on the connector, in the end of the streamer section. The accelerometer is essentially only sensitive to the vibrations in the connector, which is causing the breathing waves to propagate towards the hydrophones.

In order to gain Signal to Noise by adaptive noise cancelling, it is important that the reference sensor has high sensitivity for noise and low sensitivity for signal. That is, a high Noise to Signal ratio is desirable for the reference sensor. This is called the power inversion principle and was described in chapter 8.5 and in appendix H1.

The accelerometer signal is integrated one time before input to the adaptive processor. The adaptive processor is an adaptive linear combiner adjusted by the normalized LMS algorithm with recursive power estimate.

The adaptive processor is implemented on a DSP32C PC System Board from Loughborough Sound Images. The processor is an AT&T DSP32C digital signal processor operating with 54 MHz clock. The DSP32C is running at 12.5 MIPS (25 MFLOPS).

The board has two analog input channels and two analog output channels with alterable 4th order lowpass filters. The default cutoff frequency is 18.5 kHz.

The first experiments in this project were done with default settings of filter cutoff. Due to instability problems, the resistor values in the filter were changed to give a lowcut frequency of 600 Hz. This setting should be suitable for seismic applications. The resistor pack was chosen according to table 6 in section 6.5 in user manual ref.[31].

AT&T Software: Support Library which includes Assembler, Application software library, C Compiler and C Library routines.

Lougborough Software: Debug Monitor and Interface library.

The normalized LMS algorithm is coded in C with some routines in assembler. The main program is including modules from application software library and C library routines. Some modules were developed by Peder Christiansen ref.[28]. The main program is listed in appendix I1.

Fig.9.2 shows the experimental setup for the adaptive noise cancelling system. The experiments with the adaptive noise cancelling system will be described more in detail in chapter 10.

In the experimental setup, the reference and the primary signals are taken from a tape recorder. This is convenient in the experiments due to possibility of repeating measurements and using several channels with the same time base. The system can of course also operate directly on signals from the streamer section.

The inputs and outputs of the DSP are connected to the DSP patch panel. The output signals which can be defined in software are connected to the real time analyzer B&K2032. The result of the analysis is transferred to an IBM type PC for presentation.

The DSP board is installed in another PC. The software for the DSP is compiled and downloaded to the DSP. The DSP is controlled and monitored from software running on the PC processor.

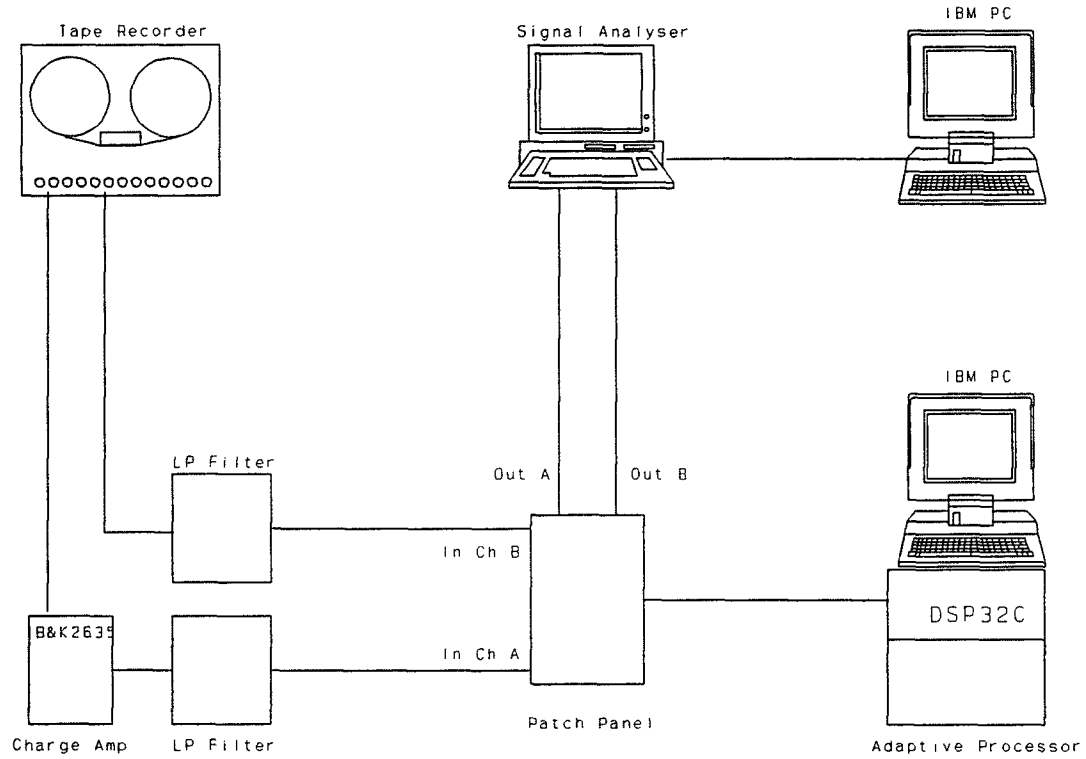

Figure 9.2 Experimental setup for the adaptive noise cancelling system.

10.0 EXPERIMENTS WITH THE ADAPTIVE NOISE CANCELLING SYSTEM

This chapter describes some experiments with the adaptive noise cancelling system. The background theory is described in chapter 8, and the implementation in a seismic hydrophone array is described in chapter 9.

The adaptive noise cancelling system have been tested for the following cases:

1) Generating noise from one end of the 12 meter section by vibrator (ref.fig.6.1)

2) Same as above, plus a source on the outside of the streamer to simulate primary signal.

3) FM Tape Recordings from previous sea tests: "Stad Girl" and "Rauberg".

Noise reduction was also seen, when testing the system with the signals recorded when towing the 12 meter streamer section in the ship tank at DMI (ref. chapter 7).

The principle of the adaptive noise cancelling system was described in fig.9.1, and the experimental setup with the DSP and the signal analyzer was shown in fig.9.2.

The first tests showed that the accelerometer signal must be integrated once in order to achieve efficient noise reduction at low frequencies (ref.fig.9.1). In experiments with the 12 meter section it was possible to select integration mode on the charge amplifier. But for experiments with older measurements from sea tests, it was necessary to do an analog integration of the accelerometer signal before connecting to the DSP. This was done by connecting a capacitor in series with an integrating charge amplifier on the output signal from the tape deck.

The following measurements were done with the B&K2032 FFT analyzer:

- Auto Spectrum ch.A, PSD (Power Spectrum Density) e.g. accm. signal
- Auto Spectrum PSD ch.B, for hydrophone group or single hydrophone
- Cross correlation, showing correlation between ch.A and ch.B
- Time ch.A, Time ch.B
- Transfer Function H1 magnitude
- Transfer Function H1 phase

The data was transferred to a PC for further analysis and presentation. The software for transferring data has some limitations. Only the results in frequency domain can be transferred in Ascii format. However, all time domain results can be transferred as screen dumps. There was some problems with the software in the beginning, so some of the results are only available as screen dumps.

The input and output channels of the DSP can be defined in the control software for the processor:

Input Ch.A: Reference signal/ Accelerometer
Input Ch.B: Primary signal/ Hydrophones
Output Ch.A: Signal after adaptive noise cancelling
Output Ch.B: Signal before adaptive noise cancelling

By connecting the two output channels to the analyzer, it is then possible to see the effect of noise cancelling both in real time and the steady state solutions after the learning phase. The transfer function magnitude is then representing the damping gained by the adaptive noise cancelling system.

10.1 Generating Noise in 12 Meter Section with Vibrator

The 12 meter section was hanging according to fig.6.1. The vibrator was excited with pseudo random noise from the built-in signal generator in the B&K 2032 FFT signal analyzer. The accelerometer signal and the hydrophone signals were recorded for different hydrophone group configurations.

The coherence between the accelerometer and the hydrophones was close to 1.0 for all frequencies (within band of analysis) in the measurements in chapter 6. The measurements of coherence are shown in appendix F4. According to the theory in chapter 8, a good result of adaptive noise cancelling can be expected when the coherence is close to 1.0.

With the real time analyzer, it was possible to actually see how the adaptive processor was learning to cancel the noise when turning on the process. With a split screen on the analyzer it is possible to see the signal with and without the effect of noise cancelling (ref. the two output signals from the DSP).

Demonstrating the effect of adaptive noise cancelling:

The effect of the adaptive noise cancelling system was first demonstrated by generating pseudo random noise with the vibrator and cancelling the noise component in the hydrophone signal. Fig.10.1 shows the hydrophone signal when turning on the adaptive noise cancelling. Time (0 - 32 seconds) is along the x-axis and amplitude along y-axis. The adaptive system is turned on at time point 6 seconds.

In this case, the primary signal contains noise correlated in some unknown way with the vibrations of the connectors. So the effect of the adaptive filter should be to remove the noise signal. The noise cancelling can be seen to take effect just after turning on the filter at time point 6 seconds.

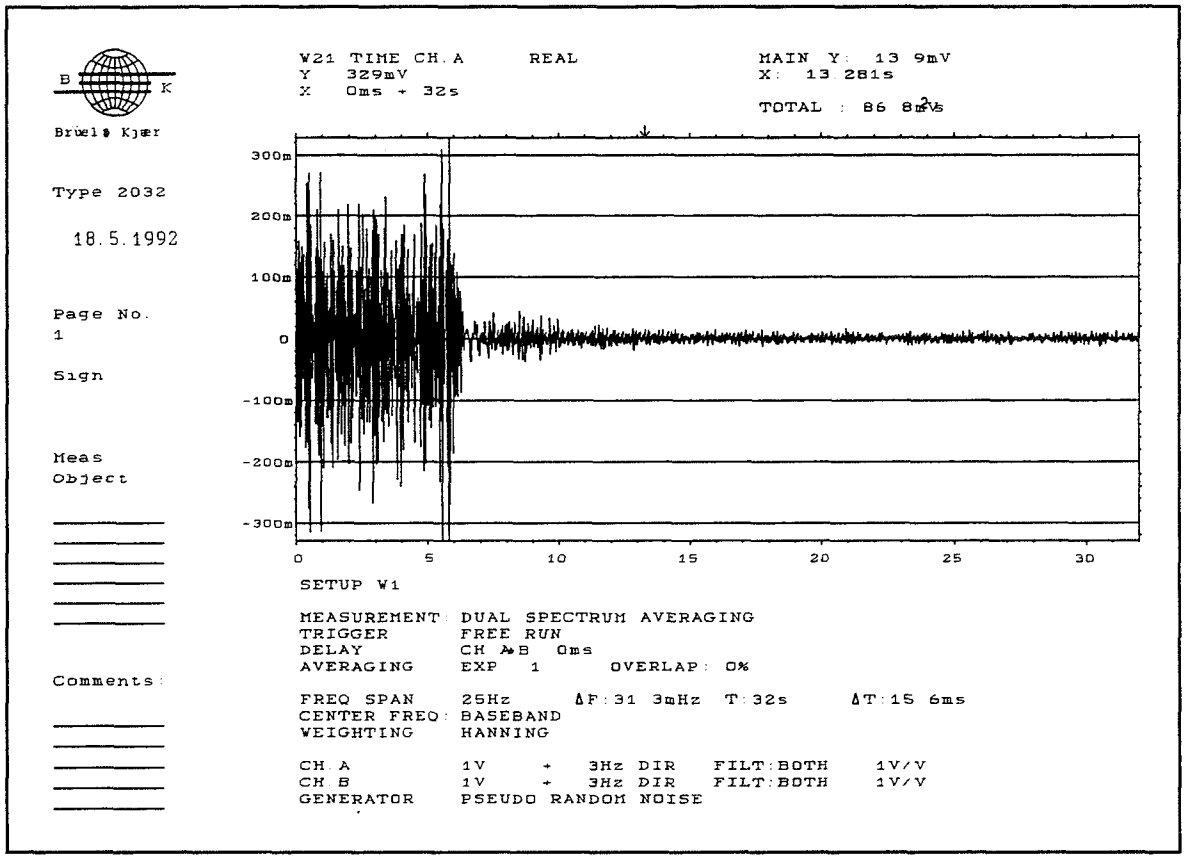

Figure 10.1 Time response output signal from adaptive processor. Showing the effect of adaptive noise cancelling when processor is turned on at time 6s.

These first results were certainly very promising. The system was working so well, that I was rather suspicious at first. I needed some way to verify the results before thrusting them.

The response of the system can be verified by comparing the filter coefficients of the adaptive linear combiner in fig.10.3 with the measured Real Impulse Response in fig.10.2.

From the rough calculations of travelling time from wave speed and distance, the peak in the impulse response can be expected at 30 ms. The peak in the measured impulse response is at 31 ms in fig.10.2. The effect of the adaptive algorithm should be to adapt the settings of the filter weights similar to the measured impulse responce. The filter coefficients in fig.10.3 has a peak at 40 ms. This is quite close to the expected response and the processor is obviously adapting to the unknown impulse response (transfer function).

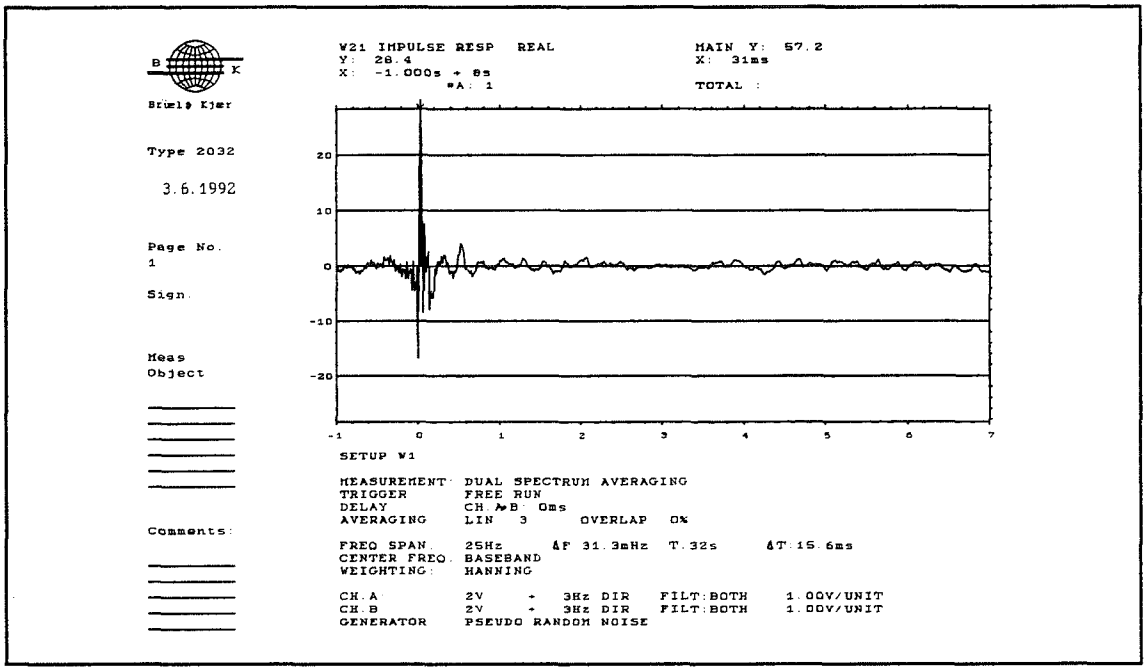

Figure 10.2 Measured Impulse Response from Hydrophone H23 to H21 for the breathing wave mode.

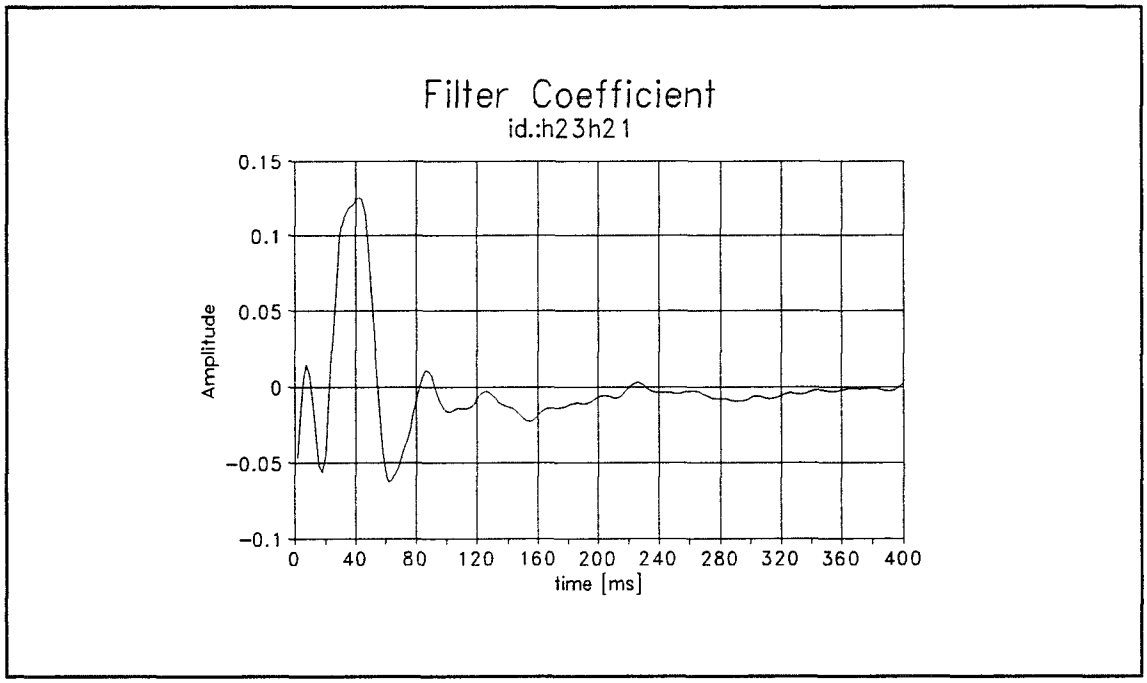

Figure 10.3 Filter coefficients in steady state (after adaption). Adaptive noise cancelling on Hydrophone H21 using H23 as a reference. N=200 coefficients, 2 ms sampling.

The learning curve:

The adaption speed was chosen very low in order to see the learning phase. In normal operation the adaption time is actually a lot shorter then the time seen in fig.10.1. The squared error is recorded as a function of time immediately after filter is turned on. The reduction in squared error as a function of sample number is called a learning curve. The learning curve for noise cancelling on hydrophone group (H24,H23,H22,H21) using the accelerometer as reference can be seen in fig.10.4.

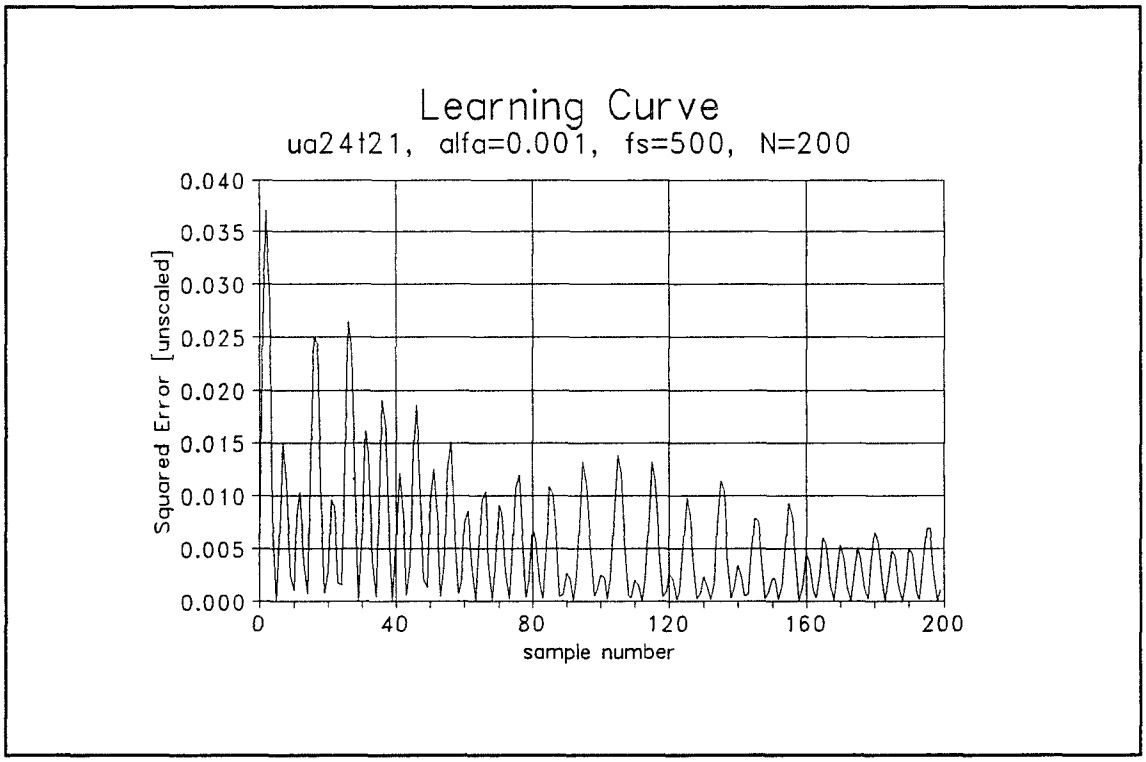

Figure 10.4 The Learning Curve for adaptive noise cancelling on hydrophone group (H24,H23,H22,H21), using the accelerometer as a reference sensor.

Noise reduction in dB:

After the learning phase the steady state solution gives a signal where the noise is strongly reduced. The damping can be seen directly in dB by measuring the transfer function magnitude from the signal before to the signal after noise cancelling. The damping achieved by adaptive noise cancelling for the case as described above can be seen in fig.10.5.

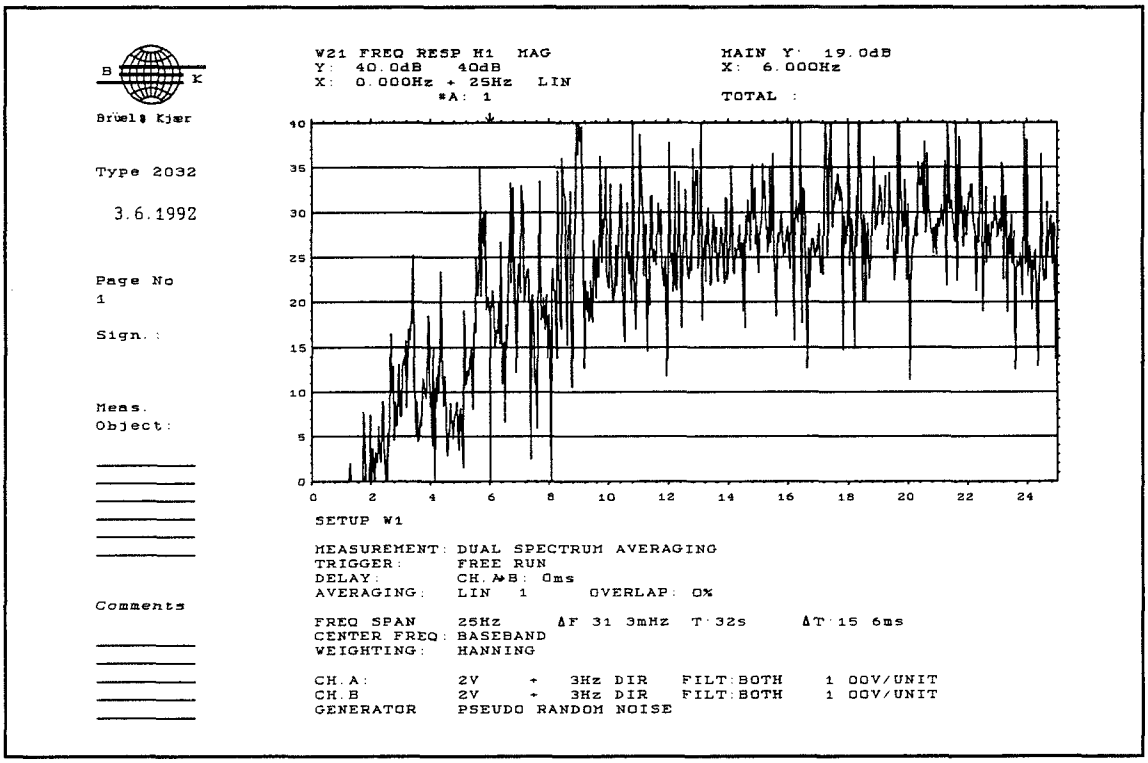

Figure 10.5 Damping in dB achieved by adaptive noise cancelling on hydrophone group (H24,H23,H22,H21), using the accelerometer as reference sensor.

The noise reduction is in the order of 20 dB, however some lower below 6 Hz.

The software package QPRO 4.0 has been used for presentation of the analyzed frequency domain signals. The standard option in QPRO: weighted Moving Average (MA) with period 12 has been applied to smooth the data-set for presentation (fig.10.6 etc.). The peaks and main structure of the spectrum are preserved when using the weighted MA process. The plots marked B&K like fig.10.5 above are direct screen-dumps and **no** MA has been applied to these.

10.2 Generating Noise with Vibrator Plus Primary Signal

The setup was similar to the setup above (ref. figur 6.1), plus an additional speaker mounted outside adjacent to the streamer section. It was then possible to simulate a realistic case, where the hydrophone signal is a sum of noise due to breathing waves propagating from the vibrating connector and a signal component from the external source. The speaker was mounted just a few cm from the streamer skin on a pedestal close to the position of hydrophone H23.

The signals from the accelerometer and hydrophones were recorded on a FM tape recorder for experiments with the adaptive system.

Case 0:	60 Hz signal to speaker no noise generated with vibrator	ref.fig.10.6
Case 1:	60 Hz signal to speaker Pseudo RND noise 0-100 Hz to vibrator	ref.fig.10.7
Case 2:	60 Hz signal to speaker 15 Hz signal to vibrator	ref.fig.10.8
Case 3:	Impulse signal to speaker 15 Hz signal to vibrator	ref.fig.10.9
Case 4:	Impulse signal to speaker Pseudo RND noise 0-100 Hz to vibrator	ref.fig.10.10

The hydrophone signal directly from tape should be the same as the output signal from the adaptive processor in case 0, when no noise is generated. The signals are compared in fig.10.6

The two signals are very similar except for some mismatch at low frequencies. This might be due to the fact that the signal has been through an A/D and D/A conversion.

The signal before and after noise cancelling for Case 1 are shown in fig.10.7. Before noise cancelling the signal component at 60 Hz from the external source (speaker) is nearly drowned in "pseudo random" noise. After noise cancelling the signal component stands clearly out, and the improvement in signal to noise ratio is approximately 20 dB.

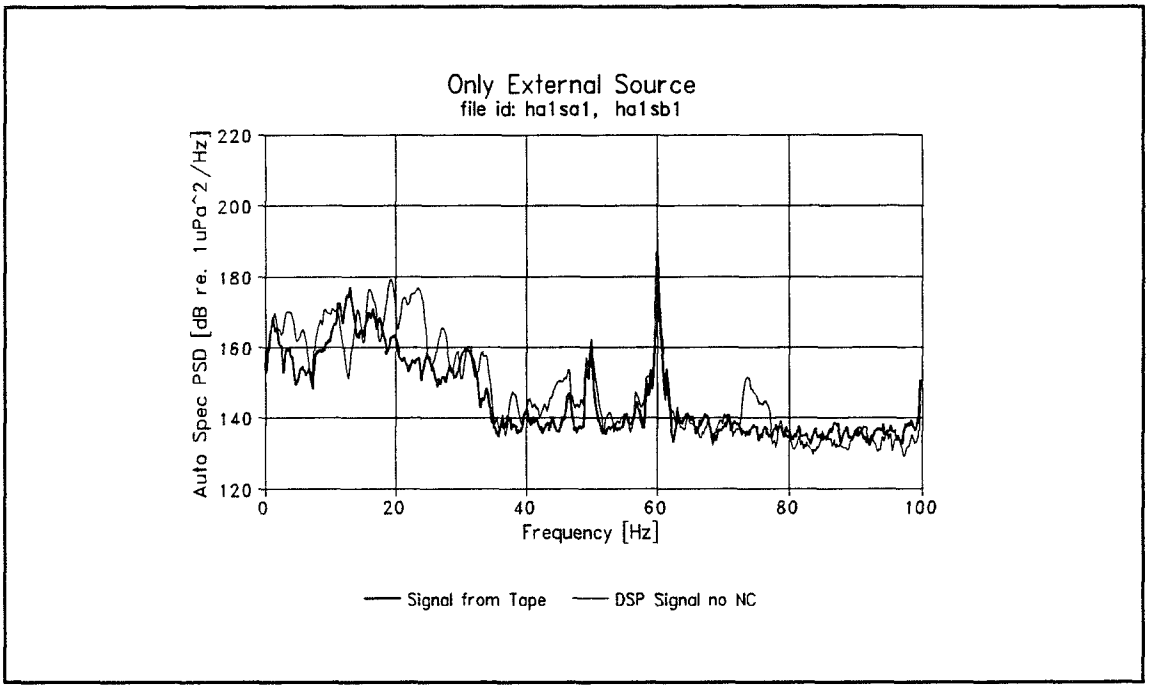

Figure 10.6 Case 0: No noise generated and 60 Hz signal. Comparing output signal from adaptive noise cancelling system to input signal.

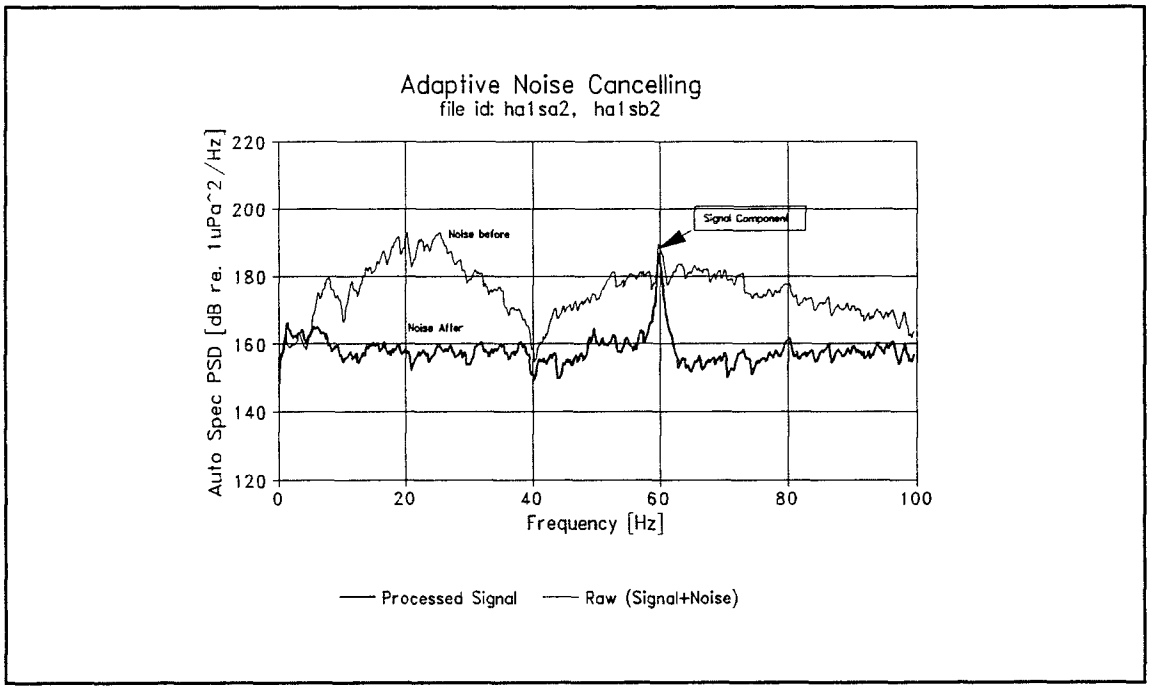

Figure 10.7 Case 1: Pseudo RND noise and 60 Hz signal. Comparing before and after adaptive noise cancelling.

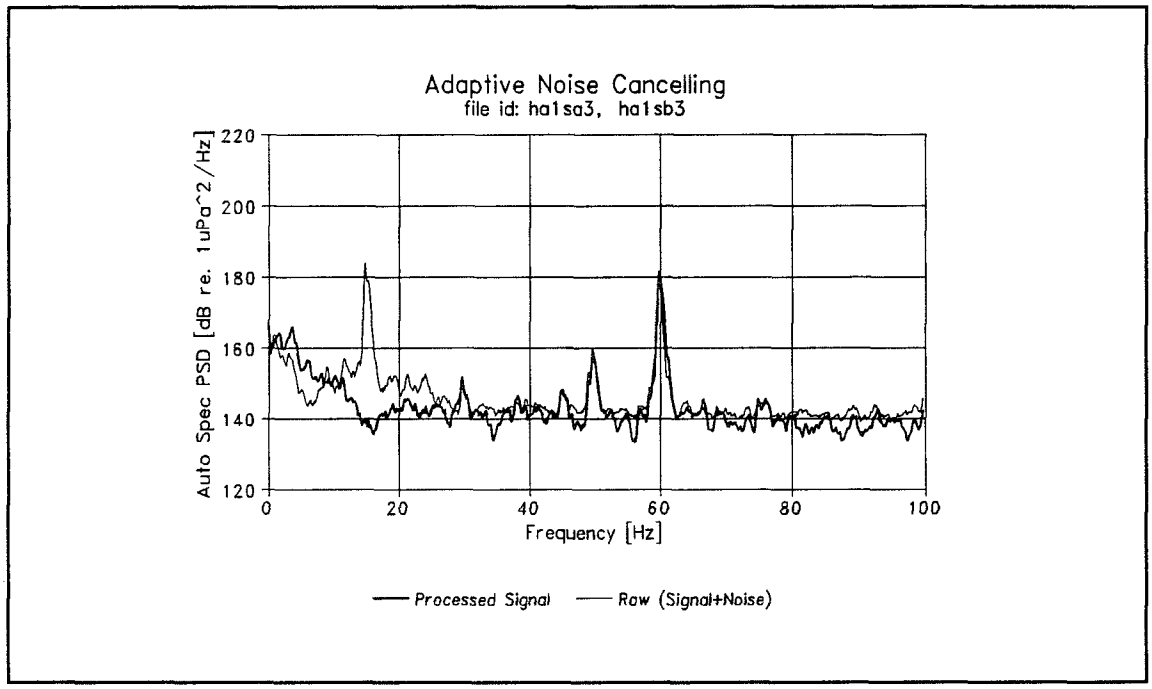

Figure 10.8 Case 2: 15 Hz noise and 60 Hz signal. Comparing before and after adaptive noise cancelling.

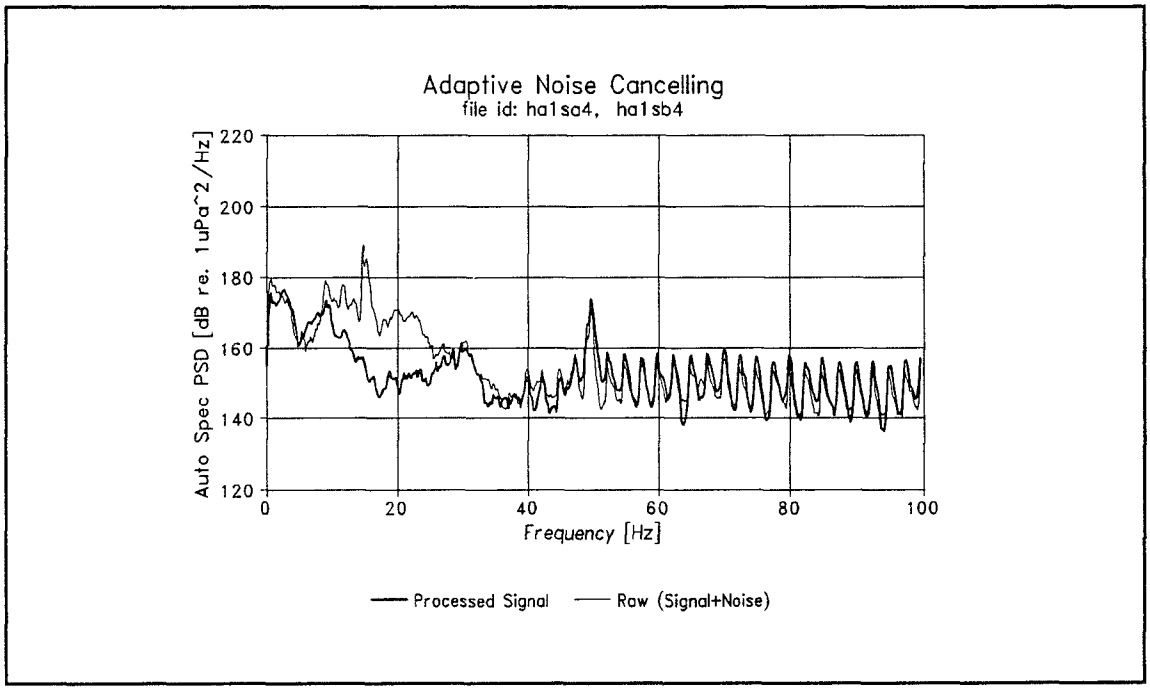

Figure 10.9 Case 3: 15 Hz noise and impulse signal. Comparing before and after adaptive noise cancelling.

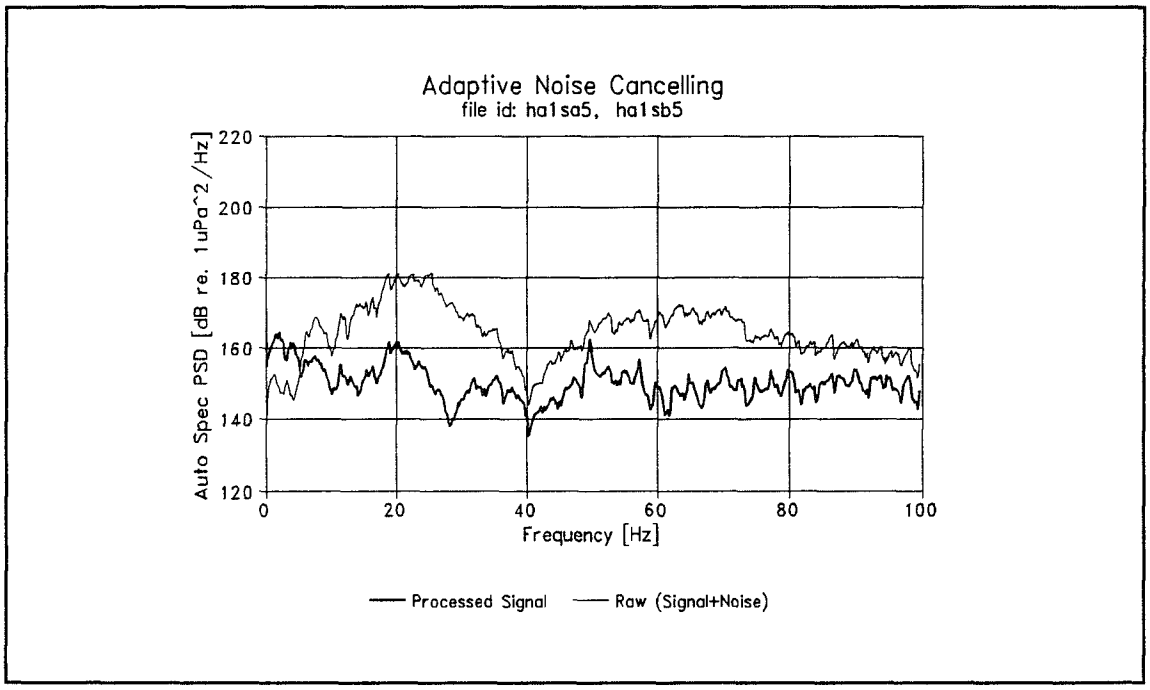

Figure 10.10 Case 4: Pseudo RND noise and impulse signal. Comparing before and after adaptive noise cancelling.

The signals before and after noise cancelling for case 2 are shown in fig.10.8. Before turning on the adaptive processor the spectrum contains both the primary signal at 60 Hz (speaker) and the generated noise signal at 15 Hz. After the learning phase, the adaptive filter has removed the noise component at 15 Hz without affecting the desired signal at 60 Hz.

In fig.10.9 the speaker was driven with impulse excitation to simulate a seismic impulse signal from the outside. Simultaneously the vibrator was generating breathing waves (noise) with a frequency of 15 Hz. The adaptive processor removes the 15 Hz noise component without affecting the desired primary impulse signal. This is the kind of behavior we desire for seismic signals containing primary seismic information and noise due to breathing waves generated by vibrations in the hydrophone array.

The adaptive processor is removing the noise to some extent for case 4 in fig.10.10, but the primary signal is not perfectly recovered. It seems to be more difficult to recover broadband signals in broadband noise.

Fig.10.11 and fig.10.12 shows an example of time domain signal representation of the signals before and after adaptive noise cancelling for case 3. In fig.10.11 the primary impulse signal is totally dominated by the generated 15 Hz breathing wave noise. After noise cancelling, the weak impulse signals from the external speaker in air can be seen clearly.

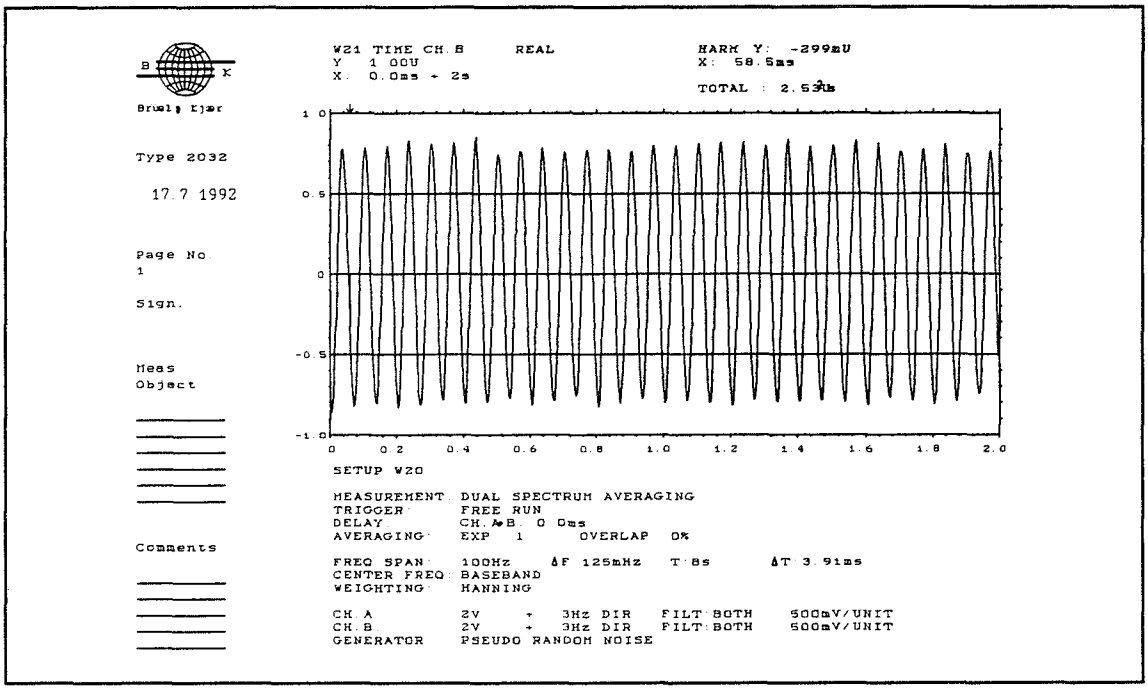

Figure 10.11 Case 3. Time response for hydrophone signal **before** adaptive noise cancelling.

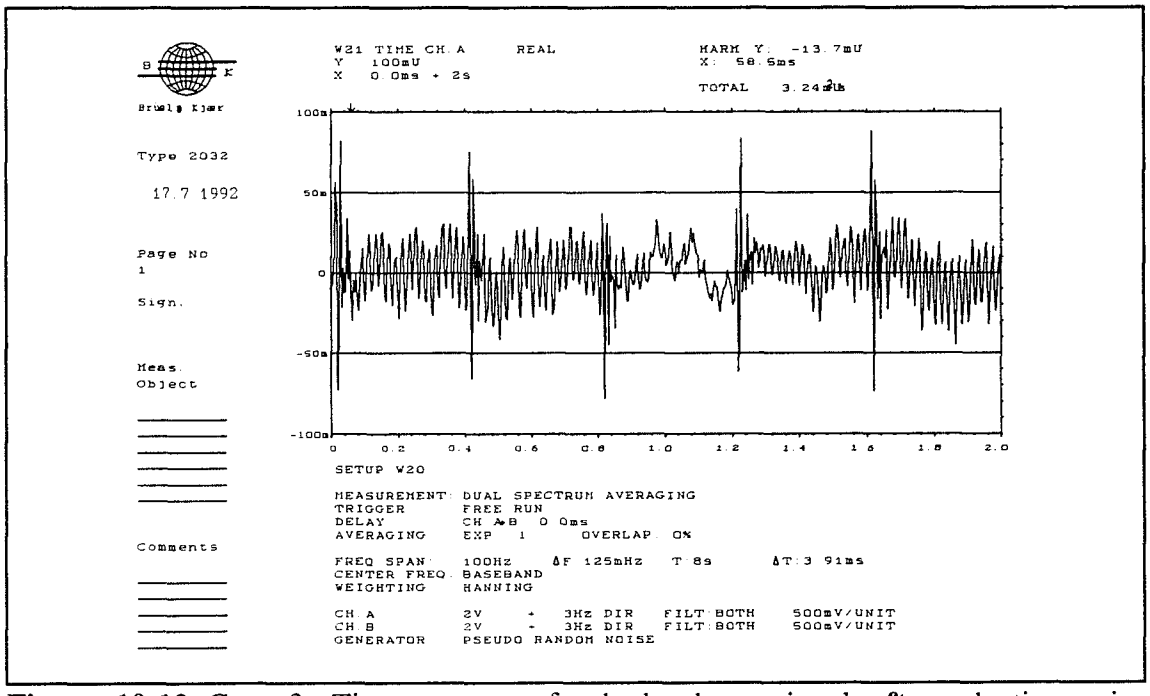

Figure 10.12 Case 3. Time response for hydrophone signal **after** adaptive noise cancelling.

10.3 Sea Test Recordings: Stad Girl and Rauberg data

The adaptive noise cancelling system has also been tested with old recordings of hydrophone signals in previous sea tests like the "Stad Girl" test in 1986 and the test on "Rauberg" in 1989. The result of adaptive noise cancelling is expected to be even better with new improved accelerometer recordings. The accelerometers in these tests were primarily installed for monitoring of towing conditions at that time.

A new improved accelerometer unit has been built during this project. The unit has been tested on a seismic vessel and a brief description of the results are given in the end of this section.

The hydrophone signal before and after noise cancelling is compared in fig.10.13. The hydrophone signal and the reference signal from accelerometer is taken from noise recordings with no seismic signal during the "Stad Girl" test in 1986.

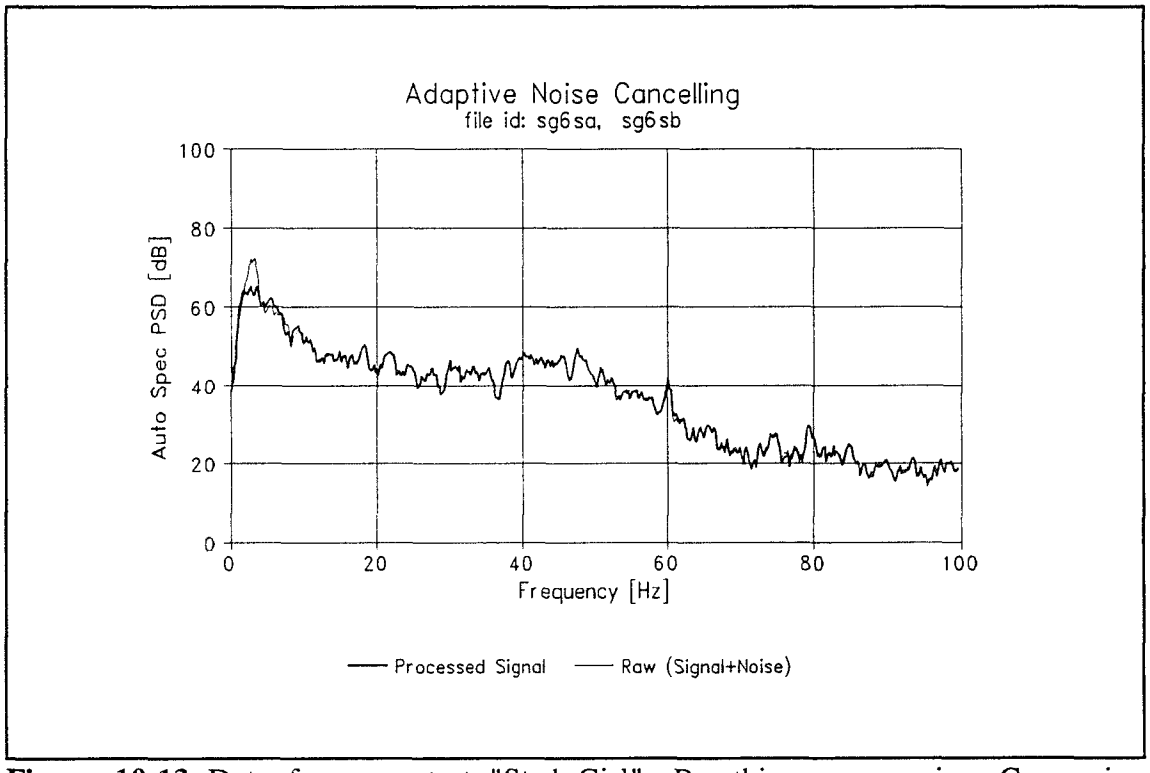

Figure 10.13 Data from sea test "Stad Girl". Breathing wave noise. Comparing hydrophone signal before and after adaptive noise cancelling.

Some of the recordings in the Stad Girl tests are of special interest because they also contain recordings of seismic pulses. This is actually the realistic case with a hydrophone signal that contain both noise and seismic signal. We also have simultaneous recordings of a reference signal from an accelerometer mounted on a nearby connector. Though the reference signal is not of desired quality, the adaptive system gives a noise reduction of the low frequency breathing wave noise.

The hydrophone signal containing primary signal (seismic pulse) and breathing wave noise are compared before and after adaptive noise cancelling. The breathing wave noise mainly around 5 Hz is reduced approximately 10 dB. The time response for the signals before and after noise cancelling can be seen in fig.10.15 and fig.10.16 on next page.

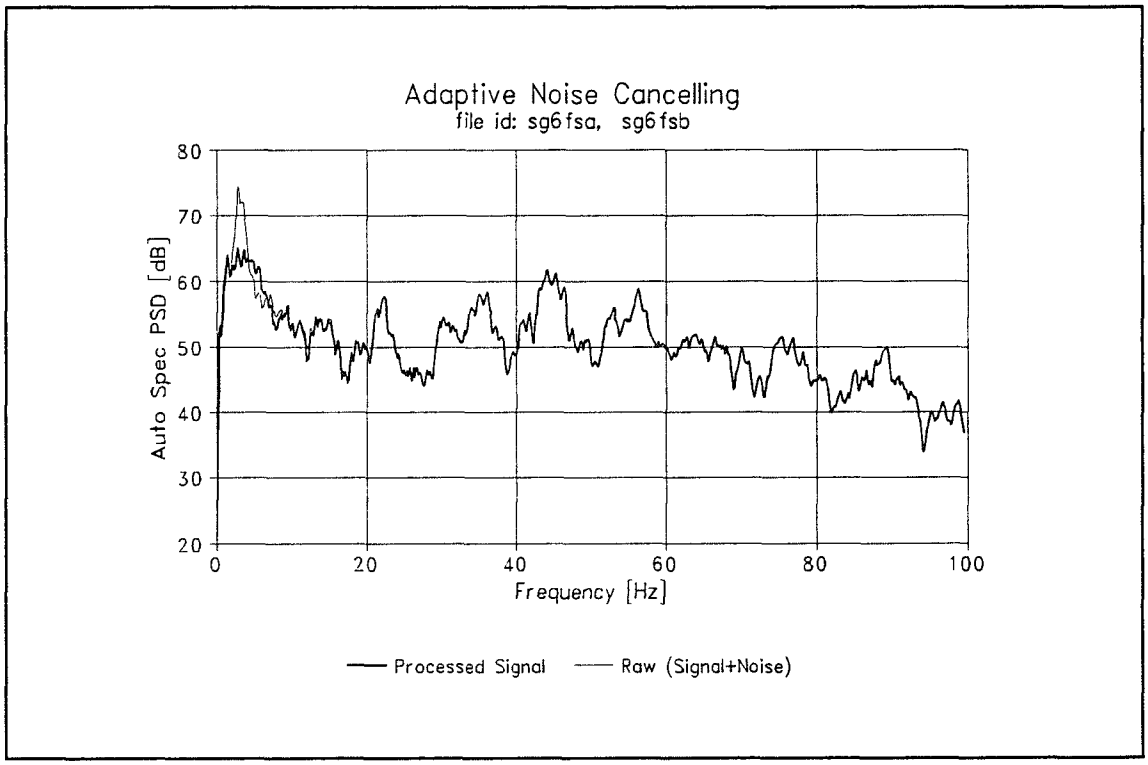

Figure 10.14 Data from sea test "Stad Girl". Breathing wave noise and signal from airgun. Comparing hydrophone signal before and after adaptive noise cancelling.

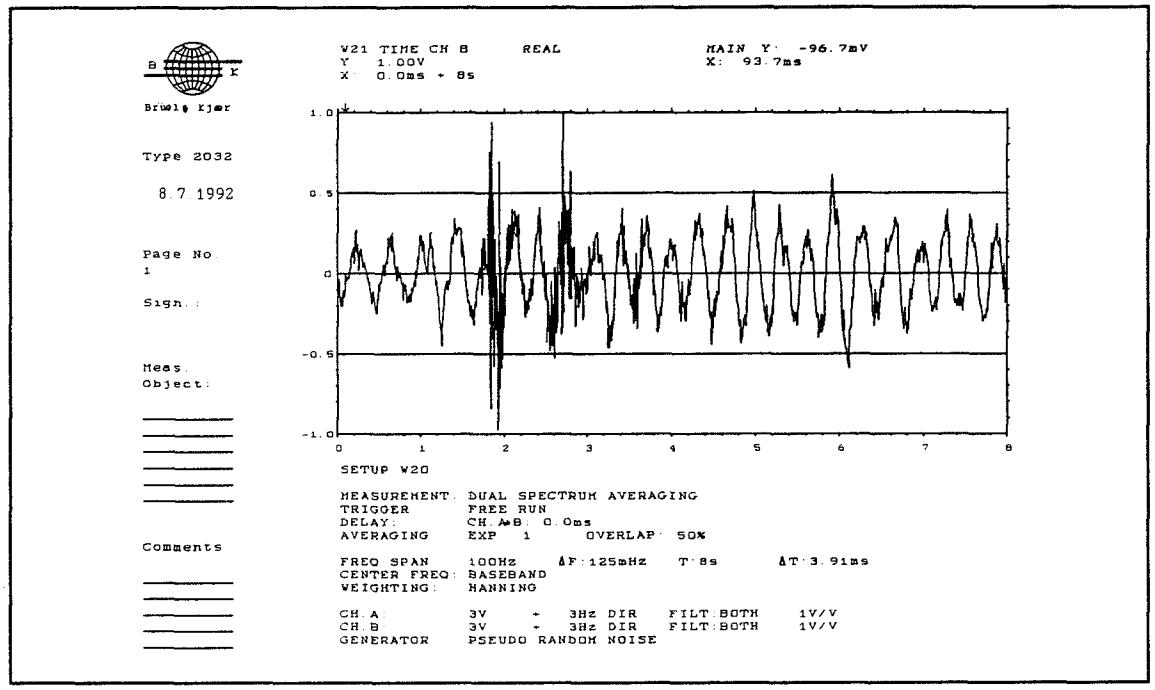

Figure 10.15 Data from sea test "Stad Girl". Time response for hydrophone signal before adaptive noise cancelling.

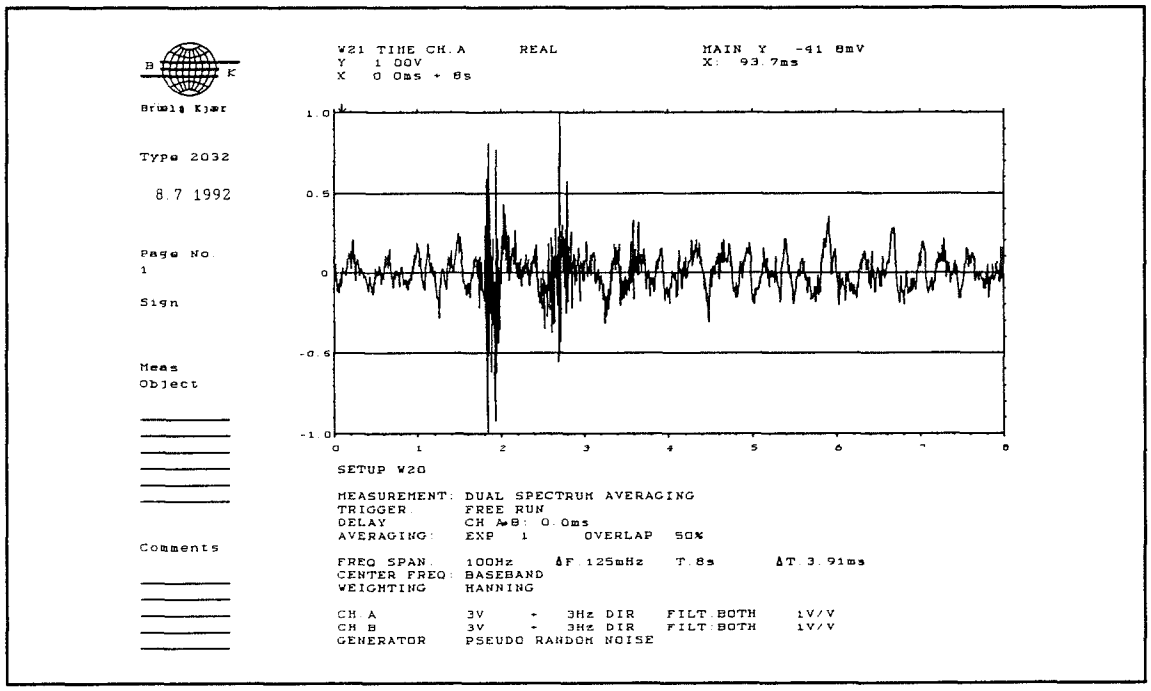

Figure 10.16 Data from sea test "Stad Girl". Time response for hydrophone signal **after** adaptive noise cancelling.

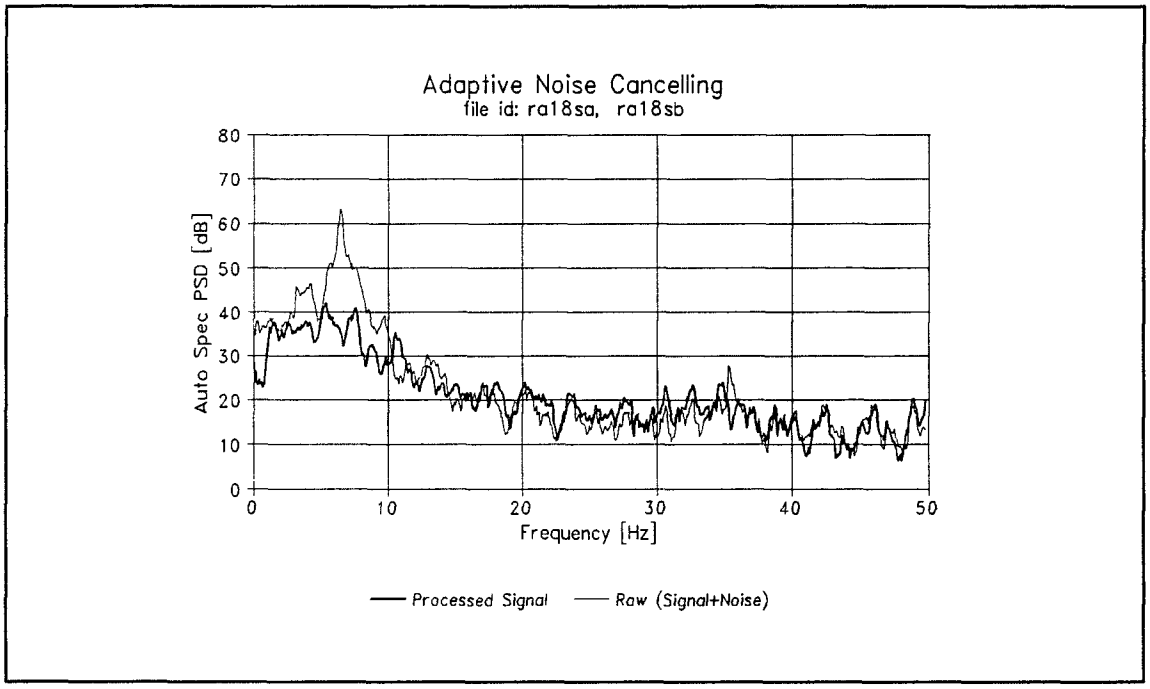

Figure 10.17 Data from sea test "Rauberg". Breathing wave noise. Comparing hydrophone signal before and after noise cancelling.

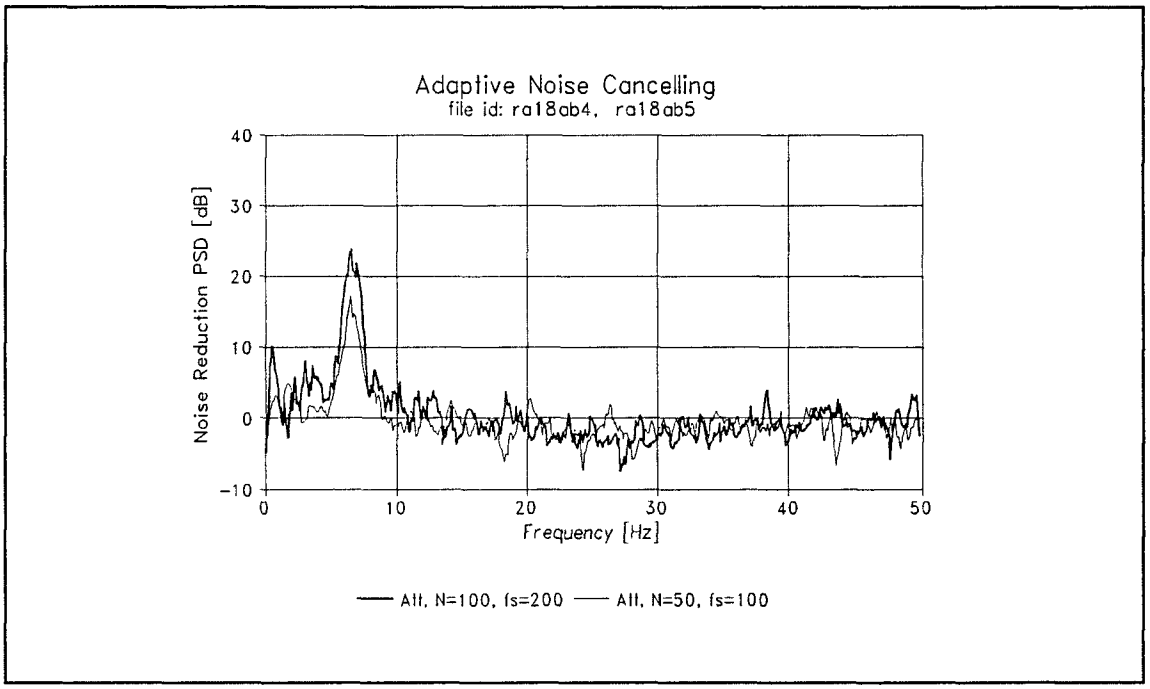

Figure 10.18 Data from sea test "Rauberg". Comparing noise reduction [dB] for two different settings of: N Number coefficients and sampling frequency.

Adaptive noise cancelling on measurements from test on M/F Rauberg:

The result of adaptive noise cancelling on the data from the "Rauberg" test can be seen in fig.10.17 and fig.10.18. Fig.10.17 is showing the power spectrum density for the noise recording before and after adaptive noise cancelling. The noise reduction is more than 20 dB for the strongest noise components around 6 Hz. The length of the adaptive filter is 100 coefficients and the sampling frequency was 200 Hz. The normalized adaption factor is 0.01 in all these measurements.

In order to minimize necessary calculation efforts, its of interest to see how much noise reduction can be gained with shorter filter and lower sampling frequency. The noise reduction in [dB] as a function of frequency for two different settings of the adaptive filter can be seen in fig.10.18. The bold solid curve shows damping achieved for the setting as above in fig.10.17. The thin solid curve shows the results of noise cancelling with N=50 filter coefficients and sampling frequency of 100 Hz. Some reduction in performance for the adaptive processor can be seen. The attenuation around 6 Hz is going down from 20 dB to 15 dB, but the noise cancelling effect is still very good.

The above experiments have shown that the adaptive noise cancelling system has a great potential for removing noise due to breathing waves.

Test of New Accelerometer Module:

A digital accelerometer unit has been developed and built according to specifications based on the experiments in the present project. A servo- accelerometer of type Sundstrand QA-700 has been built into a streamer digitalization module by Fjord's sister-company Getech. The accelerometer unit has been designed to integrate the signal one time. This means that the unit is actually measuring velocity. The reason for integration of the accelerometer signal was explained in the beginning of section 10.0.

Some measurements with the new accelerometer module on the seismic vessel "Geco Sapphire" are enclosed in appendix J1. The signal from hydrophone group trace 2 is labeled channel: seis,394, and the accelerometer signal is labeled channel: seis,385. Note the good coherence between the two signals. This looks very promising for industrialization of the adaptive noise cancelling system.

11.0 CONCLUSIONS

This work has been focused on improvement of Signal to Noise ratio in seismic data acquisition by reduction of self-generated acoustic noise in the seismic hydrophone array.

The major noise sources have been identified. This work deals mainly with the reduction of noise due to the breathing wave mechanism, which is the dominant source of noise in liquid-filled hydrophone arrays (streamer).

Two methods of achieving this goal have been developed:

1) Reduction of noise by passive design of the hydrophone array based on modelling.

Analytical expressions for breathing wave propagation containing design parameters have been found. It is then possible to analyze the noise damping properties in a specific design and compare to other designs. Furthermore the model can be used deductively to optimize design. The model can also be used in noise reduction by signal processing.

2) Reduction of noise in the seismic data by adaptive noise cancelling.

A system for adaptive noise cancelling in seismic hydrophone arrays has been developed in this project. The signal from a reference sensor essentially only sensitive to the source of noise, is used as an input to an adaptive processor. A normalized LMS algorithm adapts the filter weights to optimum performance. Only the noise components in the seismic signal that are correlated with the reference signal are removed.

A theoretical model for propagation of breathing waves has been developed. Experiments have been done to measure the viscoelastic properties of the tube wall. A frequency dependent complex Young's modulus was found from experiments with the tube material. An analytical expression for the dispersion relation and frequency dependent damping, containing material properties and other parameters in the design has been found. By using the dispersion relation and the damping function in real hydrophone array configurations, it was possible to predict transfer functions between sensors/hydrophones in the array. The predicted transfer functions by modelling have been compared to measured transfer functions. The comparison confirmed that the model gives a realistic description of the breathing wave mode in the seismic hydrophone array.

The background theory for viscoelastic behavior of streamer skin was described in chapter 2. The physical properties like the time, frequency and temperature dependence show that materials can be selected to increase the loss factor for noise due to the breathing wave mode.

Three different methods for measuring the viscoelastic behavior of streamer skin (tube) were described in chapter 3. The methods were: i) ultrasonic pulse echo, ii) resonance and iii) simple extension. The last method was found to be the best method in this application.
A realistic complex frequency dependent Young's modulus was found for the tube wall.

An introduction to the flow noise mechanism was included in chapter 4. The effect of flow noise decrease in an exponentially like way with distance from the turbulent layer. It was seen that smaller hydrophone size compared to the radius of the tube, should result in a lower flow noise level. Smaller elements should be arranged with spacing, with regards to reduction of signal from turbulent eddies convecting along the surface of the array.

In chapter 5, a model for the breathing wave mode was developed based on ref.[1]. The measured Young's modulus for the tube wall, together with geometry of the design and properties of the oil, were put into the analytical expressions for the phase speed and attenuation. This was further used in a macro model with configuration of sources and receivers according to the physical positions in the hydrophone array. It was then possible to predict transfer functions between positions in the array.

The results of modelling in chapter 5 were compared to measurements of transfer functions in chapter 6. Different setups for generation of breathing waves in a 12 meter experimental streamer section were tried. It was found that the best way to do this was by hanging the section vertically and generating the waves with a vibrator from below. The measured transfer functions were compared to the predicted(model) and a good match was found. This shows that the model is a good tool for description of the breathing wave mode in the section.

The 12 meter section was also towed in a water tank at DMI's ship laboratory in Denmark. We found that it was not easy to simulate towing in sea-conditions with such a short array. The flow conditions and imperfect termination in both ends of the section must be taken into consideration. It was however possible generate the breathing waves at low frequency, but the measurements were not of the same high quality as with controllable excitation by means of the vibrator in air.

The background theory for adaptive noise cancelling is described in chapter 8. The theory leads up to the normalized LMS with recursive power estimate, which is easy to implement on a computer. It was shown that there is a trade-off between misadjustment and speed of adaption. The power inversion principle was described, which says that the signal to noise ratio at the output is the reciprocal of the signal to noise ratio at the reference. It was also shown that the adaptive noise cancelling method can still work with a small signal component in the reference input.

In chapter 9, it was shown how the adaptive noise cancelling method is implemented in a seismic hydrophone array. A PC system board with A/D, D/A and digital processor DSP32C have been used to show the effect of adaptive noise cancelling in real time.

In an industrial application, it is however not necessary to do this in real time. The reference noise signals can be recorded on separate channels and the adaptive noise cancelling can be done as a preprocessing task.

The experiments with the adaptive noise cancelling system in chapter 10 shows that the system can give typically 10 dB improvement in signal to noise ratio. The system has been tested with data from different experiments: i) generation of breathing waves in the 12 meter section with a vibrator in the vertical setup, ii) same setup, plus external source to simulate primary signal and iii) old recordings from previous sea tests.

The results of the experiments show clearly that the adaptive noise cancelling system has the desired effect. The noise signal is strongly reduced without affecting the primary signal. For the strongest noise components in the power spectrum density presentation, a noise reduction of up to 20 dB was seen in the experiments.

Reference List

1	G.W.Morgan & J.P.Keily	Wave propagation in a viscous liquid contained in a flexible tube	J.Acoust.Soc.Am. 1954,vol26,pg323
2	J.C.F.Chow & J.T.Apter	Wave propagation in a viscous incomp. fluid contained in flexible viscoelastic tubes	J.Acoust.Soc.Am. 1967,vol44,pg437
3	S.I.Rubinow & J.B.Keller	Wave propagation in a fluid-filled tube	J.Acoust.Soc.Am 1971,vol50,pg198
4	L.Bjørnø	Finite-amplitude wave propagation in fluid-filled tubes. In: Finite-amplitude wave effects in fluids.	IPC Science and Technology Press Ltd.,London 1974
5	B.F.Giles & D.R.Steetle	Streamer noise reduction with manufacturing techniques	First Break 1989,vol7,no7
6	S.H.Francis M.Slazak J.G.Berryman	Response of elastic cylinder to convective flow noise I. Homogeneous, layered cylinders	J.Acoust.Soc.Am. 1984,vol75,pg166
7	E.J.Skudrzyk & G.P.Haddle	Noise production in a turbulent boundary layer by smooth an rough surfaces	J.Acoust.Soc.Am. 1960,vol32,pg19
8	A.J.Shashaty	The effective lengths for flow noise of hydrophones in a ship-towed linear array	J.Acoust.soc.Am. 1982,vol71,pg886
9	Bruel & Kjær	Measurements of the Complex Modulus of Elasticity.	B&K Application Notes # 17-051
10	BASF	Ellastollan Materials Properties	Technical Info.
11	GECO	Stad Girl Tests	Geco Report 79. 1986
12	H.F.Weichart	Acoustic waves along oilfilled streamer cables	Geoph.Prospecting 1973,vol21,pg281

Reference List

[13] Landau & Lifshittz. Theory of Elasticity. Pergamon 1959.

[14] J.I.Kroschwitz. Encyclopedia of Polymer science and Engineering. Vol. 17, 1989. John Wiley & Sons, ISBN 0-471-81181-5

[15] C.Hepburn. Polyurethane Elastomers. Applied Science Publ. 1982.

[16] F.J. Fahy. Sound and Structural vibration. Academic Press 1985.

[17] H.J.McSkimin, Ultrasonic Methods for measuring the mechanical properties of liquids and solids.

[18] B. Vestergaard. Identifikation af modeller for kompleks elasticitetsmodul af viskoelastiske materialer. DTH 1991.

[19] J.D.Ferry. Viscoelastic properties of polymers. 2.edition, J.Wiley 1970.

[20] A.P.Dowling/J.E.F.Williams. Sound and sources of sound. J.Wiley 1982.

[21] P.M.Morse & K.U.Ingard. Theoretical Acoustics. McGraw-Hill 1968

[22] Morse & Feshback. Methods of theoretical physics, part.II

[23] A.D.Pierce. Acoustics, published by JASA 1989. ISBN 0-88318-612-8

[24] S.Haykin. Array signal processing. Prentice-Hall 1984.

[25] S.Haykin. Adaptive Filter theory. Prentice-Hall 1991.

[26] L.E.Kinsler & A.R.Frey. Fundamentals of Acoustics. third edition J.Wiley 1982.

[27] L.Hatton/M.H.Worthington/J.Makin Seismic Data Processing. Blackwell Scientific Publications 1986. ISBN 0-632-01374-5.

[28] Peder Christiansen, Aktiv Støybekæmpelse i førerkabin på et lokomotiv, studienummer: C 858102, Lab. for Industriel Akustik, DTH 1991

[29] B.Widrow/S.D.Stearns, Adaptive Signal Processing, Prentice Hall 1985.

Reference List

[30] J.R.Treichler/C.R.Johnson/M.G.Larimore, Theory and Design of Adaptive Filters, J.Wiley & Sons 1987.

[31] Lougborough Sound Images, DSP32C PC System Board User manual, 1989.

[32] C.Bjelland, Riblets on Streamer Skin, Fjord Instruments, May 11, 1991.

[33] C.Bjelland, "Streamerskin", Patent application: Norsk nr 911376 av 9.april 1991. Commercial rights by Geco a/s.

[34] C.Bjelland/J.Å.Langeland, "Støykansellering av pustebølger", Patent application: Norsk nr 920922 av 9.mars 1992. Commercial rights by Geco a/s.

[35] C.Bjelland/J.Å.Langeland, "Turbulensstøykansellering", Patent application: Norsk nr 920921 av 9.mars 1992. Commercial rights by Geco a/s.

[36] K.F.Graff, "Wave motion in elastic solids", Clarendon Press - Oxford 1975

Appendix A1: Traceplot Stad Girl

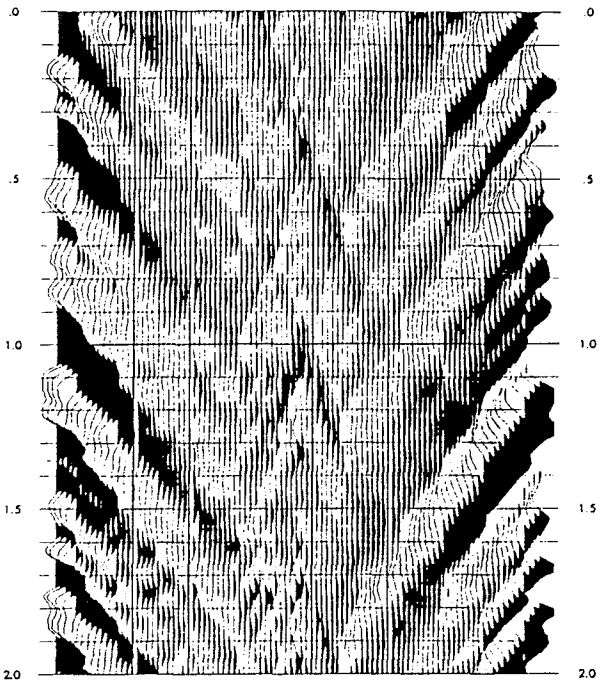

Fig. 4.6 Traceplot of special single hydr. section

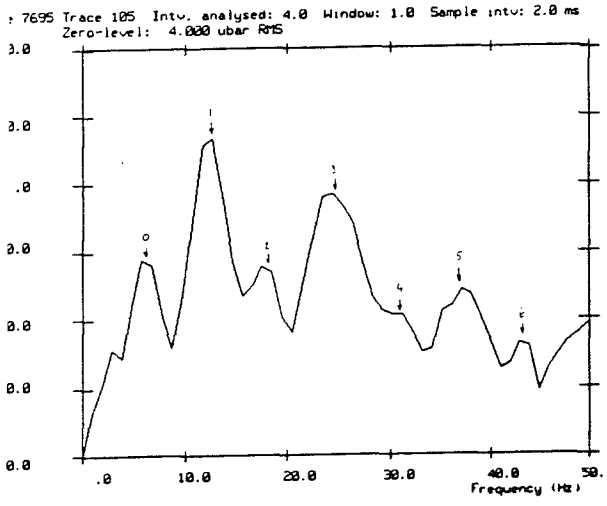

Fig. 3.24 50 m wide no fairing on lead-in. 5 knots

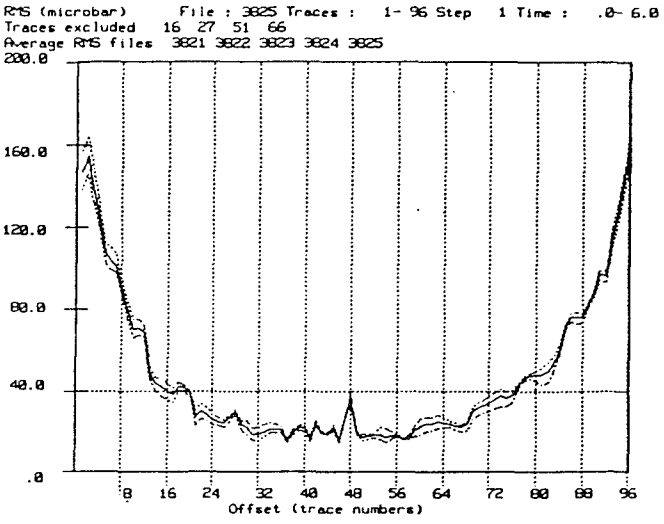

Fig. 4.7 RMS as function of offset from single hydr. section

Appendix B1: The Strain Tensor

The state of deformation at a given point in a viscoelastic body is given by the strain tensor ref.[13].

$$u_{ik}=\frac{1}{2}\left(\frac{\partial u_i}{\partial x_k}+\frac{\partial u_k}{\partial x_i}+\frac{\partial u_l}{\partial x_i}\cdot\frac{\partial u_l}{\partial x_k}\right) \tag{1}$$

In most cases occurring in practice, the strains are small. This means that change in any distance within the body is small to the distance itself. The last term in equation (1) can therefore be neglected.

$$u_{ik}=\frac{1}{2}\left(\frac{\partial u_i}{\partial x_k}+\frac{\partial u_k}{\partial x_i}\right) \tag{2}$$

This is the strain tensor for small deformations. The rate of strain tensor is similar, replacing displacement with velocity of displacement.

$$\textit{velocity of displacement: } v_i = \frac{\partial u_i}{\partial t} \tag{3}$$

Some treatises do not include the factor 1/2 in equation (2). This is to get a more practical shear strain.

Appendix B2: The Stress Tensor

The stress is associated with strain and its time dependence. The components in the stress tensor is ref.[13]:

$$\sigma_{ij} = \begin{pmatrix} \sigma_{11} & \sigma_{12} & \sigma_{13} \\ \sigma_{21} & \sigma_{22} & \sigma_{23} \\ \sigma_{31} & \sigma_{32} & \sigma_{33} \end{pmatrix} \quad (1)$$

Where σ_{ij} is the component parallel to the j direction of the force per unit area acting on the face of a cubical element which is perpendicular to the i direction.

For uniform (homogeneous) deformation the stress and strain components do not vary with position. A type of uniform deformation used in many experiments is the simple shear. The two opposite faces (13 plane) of a cubical element are displaced by sliding in the 1 direction. The only nonzero elements in the strain tensor is $u_{12} = u_{21}$. The only nonzero elements in the stress tensor is σ_{12} and σ_{21}. In the case of additional hydrostatic pressure the diagonal is nonzero. The strain u_{21} and the stress σ_{21} is a function of time. They are related by a constitutive equation for linear viscoelasticity, which for simple shear has a simple form. The equation is based on the principle that the effects of sequential changes in strain are additive:

$$\sigma_{21}(t) = \int_{-\infty}^{t} G(t-t')\dot{u}_{21}(t')dt' \quad (2)$$

G(t-t') is called the shear rate. An alternative constitutive equation can be written to express the strain in terms of the history of stress:

$$u_{21}(t) = \int_{-\infty}^{t} J(t-t')\dot{\sigma}_{21}(t')dt' \quad (3)$$

J(t-t') is called the creep compliance. From knowledge of shear relaxation modulus or creep compliance function of a material, its stress-strain relations for any kind of experiment in shear can be predicted.

Appendix B3: Stress-Relaxation Experiment, Creep Experiment

Stress-Relaxation Experiment:

Assumed shear strain imposed suddenly at time t=0 and held constant at value u_0. The stress $\sigma(t)$ decreases with time and for long times:

$$\sigma_{21}(t)=u_{21}G(t) \tag{1}$$

The physical meaning of relaxation modulus G(t) is apparent from this experiment. The ratio of stress to strain is called a modulus. For a perfectly elastic solid the equilibrium shear modulus G is defined σ_{21}/u_{21}. G(t) is its time dependent analog.

Creep Experiment:

Assume that the shear stress is applied suddenly at time t=0 and held constant at value σ_0. The shear strain is then:

$$u_{21}(t)=\sigma_{21}J(t) \tag{2}$$

The creep compliance J(t) has dimension of reciprocal modulus and is a monotonically increasing function of time. For a perfectly elastic solid J=1/G. This is not the case with viscoelastic materials because of different time patterns.

Appendix B4: Mechanical Models for Viscoelasticity

It can be instructive to study linear viscoelasticity from a one-dimensional viewpoint through mechanical models. The elements in such a mechanical model are massless springs with a spring constant G analogous to a shear modulus, and the viscous dashpot with viscosity constant η. The force σ(stress) across the spring is related to its elongation ϵ(strain): $\sigma=G\epsilon$. For the dashpot we have: $\sigma=\eta d\epsilon/dt$.

A series combination of a spring and a dashpot is called a Maxwell model and the parallel combination is called a Kelvin or Voigt model.

The stress-strain relation for the Maxwell model:

$$\frac{\dot{\sigma}}{G}+\frac{\sigma}{\eta}=\dot{\epsilon} \tag{1}$$

The stress-strain relation for the Kelvin model:

$$\sigma = G\epsilon + \eta\dot{\epsilon} \tag{2}$$

These simple models can not completely describe the behavior of real materials. More complicated models can be made up as combinations of simple Maxwell and Voigt models. For example a standard linear solid model, which is a Kelvin model with an additional spring in series. A sequence of Maxwell units in parallel is called a generalized Maxwell model. The total stress is the resultant of the stress across each unit. The contribution of the i'th element to the modulus is $G_i(t)$.

$$G_i(t)=G_i e^{-\frac{t}{\tau_i}} \quad , \tau_i \doteq \frac{\eta_i}{G_i} \tag{3}$$

The time constant τ_i is the relaxation time. Then the relaxation modulus is:

$$G(t)= \sum_i G_i e^{-\frac{t}{\tau_i}} \tag{4}$$

These one dimensional models are mainly guidance for qualitative thinking.

Appendix B5: Material Data Elastollan 1185

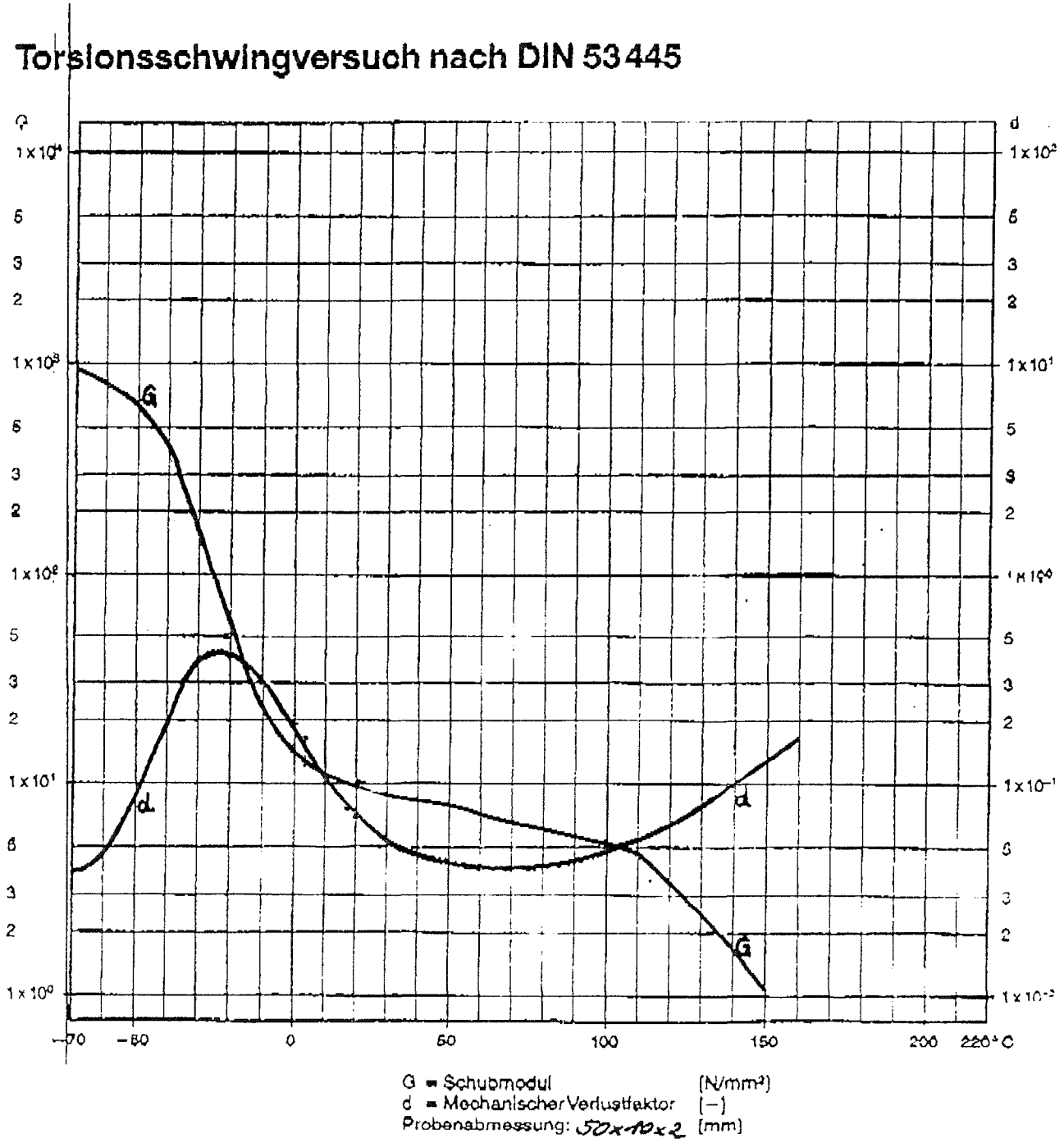

Appendix C1: Calculation Ultrasonic method, file: Ultra2m3

file:ultra2M3 rev: 17.09.91.cb

Calculation of Complex Young's modulus from ultrasonic measurements of speed and damping.

Density (kg/m^3): $\rho := 1100$

Poisson's ratio: $\sigma := 0.44$

Thickness (m): $d := 0.003$

Two-way travel. time (s): $t := 3.64 \cdot 10^{-6}$

Speed (m/s): $c := \frac{2 \cdot d}{t}$ $c = 1.648 \cdot 10^{3}$

Peak 1.refl (mV): $p1 := 646$ measured with scope cursor

Peak 2.refl (mV): $p2 := 178$

frequency (rad/s): $\omega := 2 \cdot \pi \cdot 2.25 \cdot 10^{6}$

Damping (1/m): $A := \left[\frac{\ln\left[\frac{p1}{p2}\right]}{2 \cdot d} \right]$ $A = 214.836$

Damping (dB/cm): $D := 20 \cdot \log\left[e^{-(0.01 \cdot A)}\right]$ $D = -18.66$

Damping 2d (dB): $20 \cdot \log\left[e^{-(2 \cdot d \cdot A)}\right] = -11.196$

Calc.fact: $Fa := \frac{\rho \cdot c^2}{\left[1 + \left[A \cdot \frac{c}{\omega}\right]^2\right]^2}$

Imag Plane Wave Modulus (N/m^2): $M'' := 2 \cdot Fa \cdot A \cdot \frac{c}{\omega}$ $M'' = 1.495 \cdot 10^8$

Real Plane Wave Modulus (N/m^2): $M' := Fa \cdot \left[1 - \left[A \cdot \frac{c}{\omega}\right]^2\right]$ $M' = 2.983 \cdot 10^9$

Imag Young's Modulus N/m^2: $E'' := \frac{M'' \cdot \left[1 - \sigma - 2 \cdot \sigma^2\right]}{1 - \sigma}$ $E'' = 4.615 \cdot 10^7$

Real Young's Modulus N/m^2: $E' := \frac{M' \cdot \left[1 - \sigma - 2 \cdot \sigma^2\right]}{1 - \sigma}$ $E' = 9.205 \cdot 10^8$

Loss factor: $\Gamma := \frac{E''}{E'}$ $\Gamma = 0.05$

Appendix C2: Calculation Resonance method, file: Comp6m3

file: Comp6m3 date:25.03.93CB

Beregning av complex modulus basert på målinger med B&K complex modulus apparatus type 3930

Density (kg/m^3): $\rho := 1100$

Length (m): $l := 0.180$

Thickness (m): $h := 0.003$

Clamped bar coefficients: $k_1 := 22.4$ $k_2 := 61.7$ $k_3 := 121$ $k_4 := 200$

Frequency peaks at f(Hz): $f_1 := 37$ $f_2 := 81$ $f_3 := 135.5$ $f_4 := 205$

+-3dB δf (Hz): $\delta_1 := 2$ $\delta_2 := 5.5$ $\delta_3 := 13.5$ $\delta_4 := 26.5$

$f_5 := 295$ $\delta_5 := 52$ $k_5 := 299$

$i := 1 \ldots 5$

Youngs mod (N/m^2): $E_i := 48 \cdot \pi^2 \cdot \rho \cdot \left[\frac{2}{l} \cdot \frac{f_i}{h} \cdot \frac{1}{k_i} \right]^2$

loss factor: $d_i := \frac{\delta_i}{f_i}$

f i
37
81
135.5
205
295

E i
$1.658 \cdot 10^8$
$1.048 \cdot 10^8$
$7.622 \cdot 10^7$
$6.386 \cdot 10^7$
$5.917 \cdot 10^7$

d i
0.054
0.068
0.1
0.129
0.176

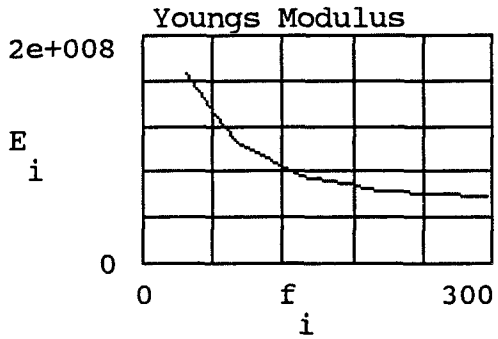

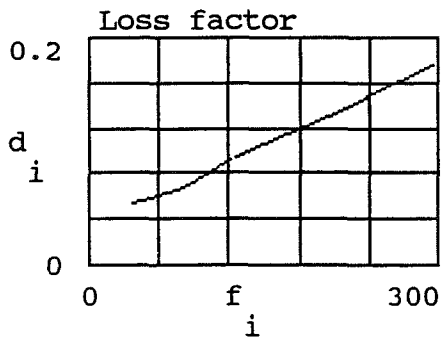

Appendix C3: Calculation Resonance method, file: Comp6y8

file: Comp6y8 date:25.03.93CB

Beregning av complex modulus basert på målinger med B&K complex modulus apparatus type 3930

Density (kg/m^3): $\rho := 1100$

Length (m): $l := 0.180$

Thickness (m): $h := 0.003$

Clamped bar coefficients: $k_1 := 22.4$ $k_2 := 61.7$ $k_3 := 121$ $k_4 := 200$

Frequency peaks at f(Hz): $f_1 := 0$ $f_2 := 37$ $f_3 := 81$ $f_4 := 135.5$

+-3dB δf (Hz): $\delta_1 := 0$ $\delta_2 := 2$ $\delta_3 := 5.5$ $\delta_4 := 13.5$

$i := 2..6$ $f_5 := 205$ $\delta_5 := 26.5$ $k_5 := 299$

$f_6 := 295$ $\delta_6 := 52$ $k_6 := 417$

Youngs mod (N/m^2): $E_i := 48 \cdot \pi^2 \cdot \rho \cdot \left[\frac{2 f_i}{l} \cdot \frac{l}{h} \cdot \frac{1}{k_i} \right]^2$

loss factor: $d_i := \frac{\delta_i}{f_i}$

f i
37
81
135.5
205
295

E i
$2.186 \cdot 10^7$
$2.724 \cdot 10^7$
$2.79 \cdot 10^7$
$2.857 \cdot 10^7$
$3.042 \cdot 10^7$

d i
0.054
0.068
0.1
0.129
0.176

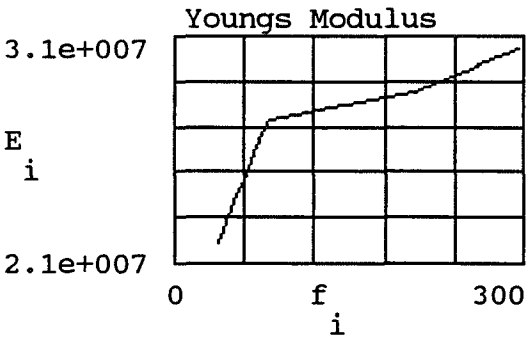

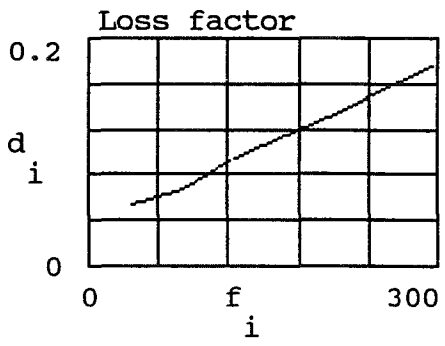

Appendix C4: Measurements Simple Extension method

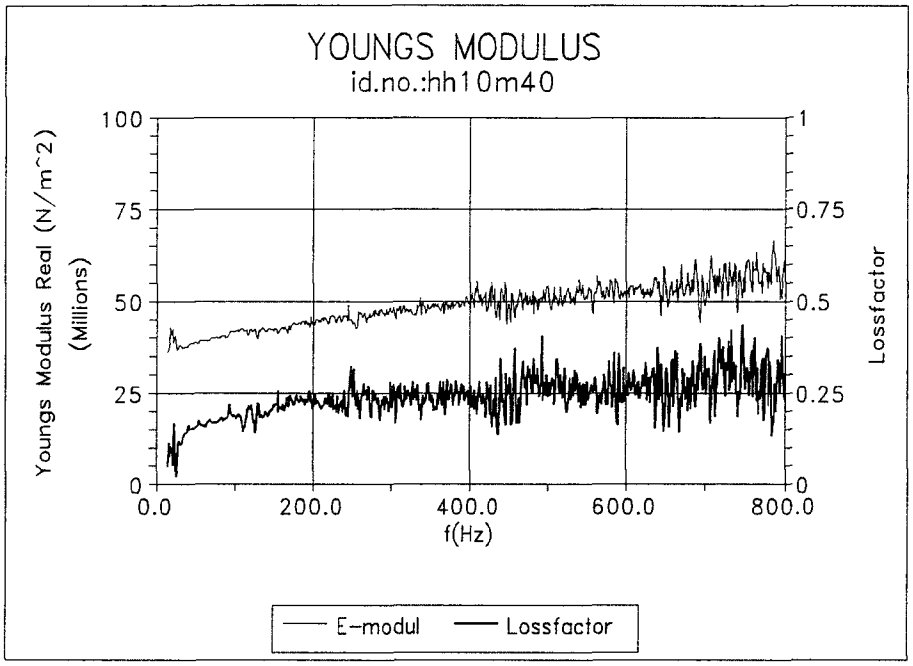

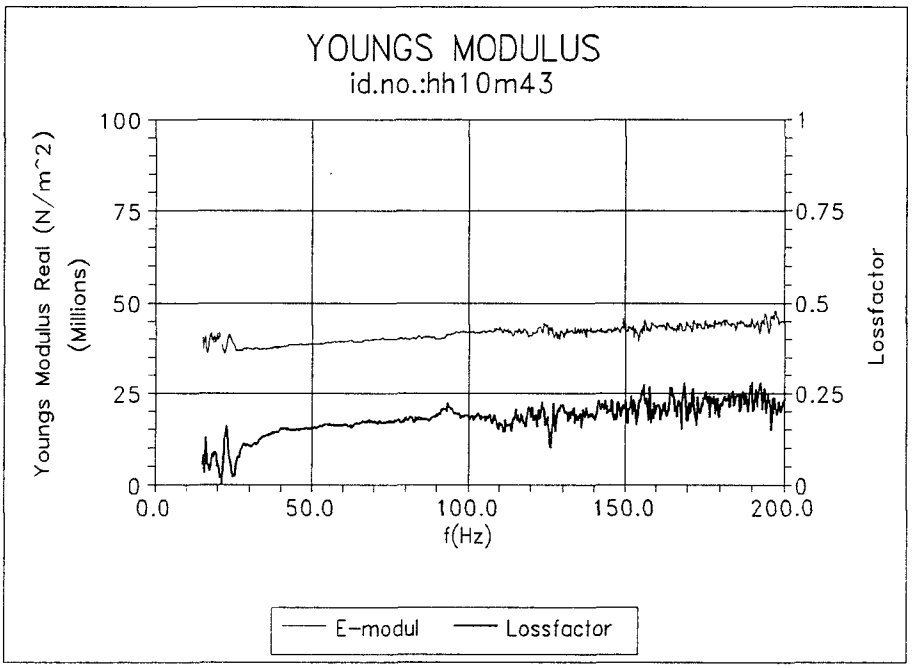

Appendix E1: Phase Speed and Damping for Breathing Wave Mode

file: MK85VE7.mcd date: 29.10.91 Cato Bjelland

Breathing waves in streamer sections:

Ref. Morgan & Kiely JASA vol26,may 1954

Skin material: Elastollan 1185A
Streamer oil: Exxon Isopar M

Density oil (kg/m^3): $\rho := 819$

Skin thikness (m): $h := 0.003$

Tube radius (m): $R := 0.034$

Viscosity (Pa*s): $\mu := 11.9 \cdot 10^{-3}$

Static Youngs modulus (N/m^2): $Es := 3 \cdot 10^{7}$

Poisson coef: $\sigma := 0.44$

$n := 2,4 \ldots 40$

Introducing frequency dependent complex Youngs modulus:
E(ω)=E'(ω)+jE''(ω) [N/mm^2]
Loss factor: d= E''/E'

ref: eh43i dh3tre
Polynomial Least-Squares Fit based on (BKVIB) measurements of complex E(ω):

Real Youngs: $E_n := Es \cdot n^0 + 1.42 \cdot 10^5 \cdot n^1 + \left[-8.72 \cdot 10^2\right] \cdot n^2 + 2.27 \cdot n^3$

Loss factor: $d_n := 1.5 \cdot 10^{-1} \cdot n^0 + 4.983 \cdot 10^{-4} \cdot n^1 - 3.597 \cdot 10^{-6} \cdot n^2 + 2.014 \cdot 10^{-8} \cdot n^3$

$\omega_n := 2 \cdot \pi \cdot n$

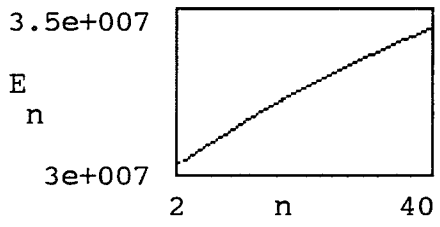

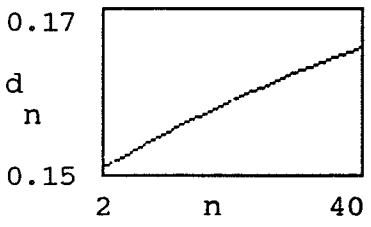

$$\delta_n := \left[\omega_n \cdot \frac{\rho}{\mu}\right]^{-\left[\frac{1}{2}\right]} \qquad \text{cond}_n := \frac{R}{\delta_n}$$

n	cond n	δ n
2	31.6	0.00108
4	44.7	0.00076
6	54.8	0.00062
8	63.2	0.00054
10	70.7	0.00048
12	77.5	0.00044
14	83.7	0.00041
16	89.4	0.00038
18	94.9	0.00036
20	100	0.00034
22	104.9	0.00032
24	109.5	0.00031
26	114	0.0003
28	118.3	0.00029
30	122.5	0.00028
32	126.5	0.00027
34	130.4	0.00026
36	134.1	0.00025
38	137.8	0.00025
40	141.4	0.00024

$\delta_{10} \cdot 1000 = 0.481$ mm boundary layer at 10 Hz

Approx. When: $R/\delta >> 1$:

$$s_n := \left[\frac{h \cdot E_n}{2 \cdot \rho \cdot R}\right]^{\frac{1}{2}} \cdot \left[1 - \left[1 - \sigma + \frac{\sigma^2}{4}\right] \cdot \frac{1}{R} \cdot \left[\frac{\mu}{2 \cdot \rho \cdot \omega_n}\right]^{\frac{1}{2}}\right]$$

$$K_n := \omega_n \cdot \left[\frac{2 \cdot \rho \cdot R}{E_n \cdot h}\right]^{\frac{1}{2}} \cdot \left[2 \cdot R^{-1} \cdot \left[\frac{\mu}{2 \cdot \rho \cdot \omega_n}\right]^{\frac{1}{2}} \cdot \left[1 - \sigma + \frac{\sigma^2}{4}\right] + [d_n]\right]$$

$$D_n := 20 \cdot \log\left[e^{-K_n}\right]$$

$$tub := \left[\frac{h \cdot Es}{2 \cdot \rho \cdot R}\right]^{\frac{1}{2}} \qquad tub = 40.2 \quad m/s$$

Skin material: Elastollan 1185A
Streamer oil: Exxon Isopar M

file:mk885ve7s

n	K n	D n	s n	cond n
2	0.055	-0.482	39.84	31.62
4	0.106	-0.921	40.18	44.72
6	0.156	-1.355	40.43	54.77
8	0.206	-1.786	40.64	63.24
10	0.255	-2.216	40.83	70.7
12	0.305	-2.645	41.02	77.45
14	0.354	-3.075	41.19	83.66
16	0.403	-3.504	41.36	89.43
18	0.453	-3.934	41.51	94.86
20	0.502	-4.363	41.67	99.99
22	0.552	-4.794	41.81	104.87
24	0.602	-5.225	41.96	109.53
26	0.651	-5.656	42.09	114.01
28	0.701	-6.088	42.23	118.31
30	0.751	-6.521	42.35	122.46
32	0.801	-6.954	42.48	126.48
34	0.851	-7.388	42.6	130.37
36	0.901	-7.823	42.71	134.15
38	0.951	-8.259	42.83	137.83
40	1.001	-8.696	42.93	141.41

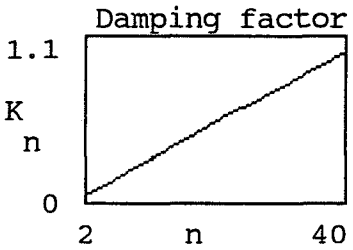

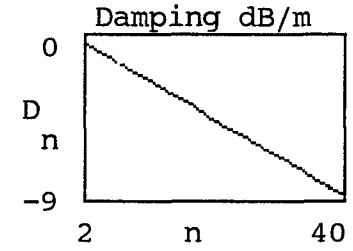

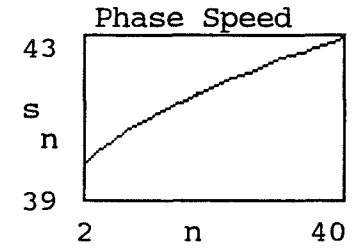

Where: n is frequency, K is damping factor,
s is phase speed, cond is conditon test

$$\alpha stad := -\left[\frac{\ln(0.5)}{3}\right]$$

$$20 \cdot \log\left[e^{-\alpha stad}\right] = -2.007 \quad dB/m$$

$m := 1 \,..\, 4$ $\quad T_1 := 2 \quad T_2 := 2.5 \quad T_3 := 4.5 \quad T_4 := 6$

$$E_m := \frac{T_m}{0.2}$$

Material:	20% T-mod: T_m	E-mod= T-mod/0.2: E_m
1180A:	2	10
1185A:	2.5	12.5

Appendix E2: Transfer Function for Breathing Wave Mode in Streamer Section

File: mcad hn21d. rev. date: 20/5 1992 CB.

Theoretical model for breathing wave transmission in streamer section. Based on measurements of complex frequency dependent viscoleastic properties and solution of hydrodynamic/elastic equations for wave propagation in viscoelastic tube. Ref. model: MK85VE7.

A := READPRN(dbulge7) data for c(ω) and k(w)=k1(ω)+jk2(ω)

$\omega := A^{\langle 0 \rangle}$ $c := A^{\langle 1 \rangle}$ $d := A^{\langle 2 \rangle}$

N := length(ω) number of data points: N = 51

n := 1 ..N - 1

N-3 From Tail Configuration:

i := 0 ..10 $x_0 := 0$ t := 0

$x_1 := 0.25$ $x_2 := x_1 + 0.05$

$x_3 := x_2 + 0.52$ $x_4 := x_3 + 0.52$

$x_5 := x_4 + 0.52$ $x_6 := x_5 + 0.52$

$x_7 := x_6 + 0.52$ $x_8 := x_7 + 0.52$

$x_9 := x_8 + 0.52$ $x_{10} := x_9 + 0.52$ Lb := 12 $ks_n := \frac{\omega_n}{1500}$

A := 1 α := 0.25 ß := 0.0033 $k_n := \frac{\omega_n}{c_n}$ $u_n := n$

$\epsilon := 10^{-8}$ B := 0.5 R := 0

Wave equations:

$p_{i,n} := A \cdot e^{-[d_n \cdot x_i]} \cdot e^{j \cdot [\omega_n \cdot t - k_n \cdot x_i]}$

$z_{i,n} := R \cdot e^{-(ß \cdot Lb)} \cdot e^{-[d_n \cdot |Lb - x_i|]} \cdot e^{j \cdot [\omega_n \cdot t + k_n \cdot [x_i - Lb] - [ks_n \cdot Lb]]}$

file: hn21d date: 20/5-92

$$pr_{i,n} := p_{i,n} + r_{i,n}$$

$$h_{4,n} := \frac{pr_{4,n}}{pr_{2,n} + \epsilon}$$

$$H_n := 20 \cdot \log\left[\left|h_{4,n}\right|\right]$$

$$F_n := \frac{180}{\pi} \cdot \arg\left[h_{4,n}\right]$$

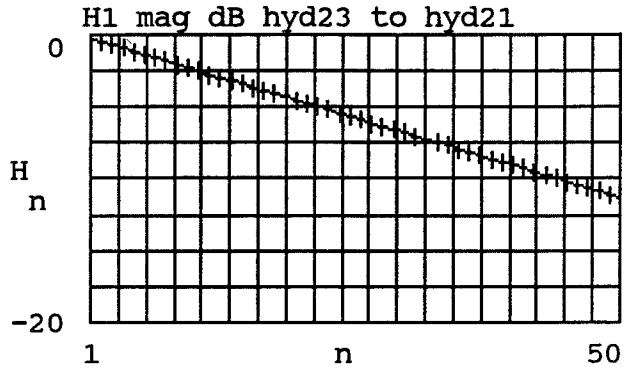

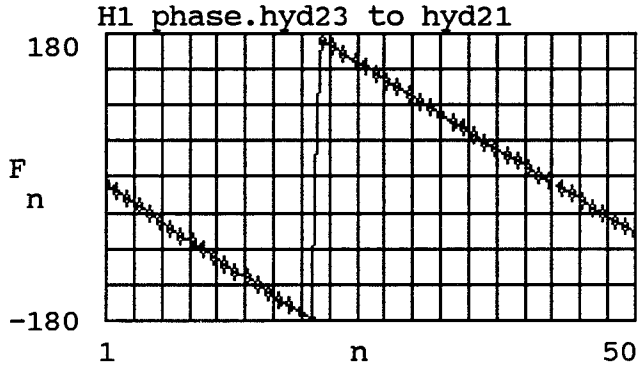

acceleration:

$$a_{i,n} := j \cdot \omega_n \cdot B \cdot p_{i,n}$$

WRITEPRN(H1h23h21) := augment(u,augment(H,F)) ▫

mi := 1 ..4

$$G_n := \frac{\sum_{mi} pr_{mi,n}}{pr_{0,n} + \epsilon}$$

$$Ba_n := 20 \cdot \log\left[\left|G_n\right|\right]$$

$$Fa_n := \frac{180}{\pi} \cdot \arg\left[G_n\right]$$

file: hn21d date: 20/5-92

Transfer function acm. to
hyd gr.(H24,H23,H22,H21):

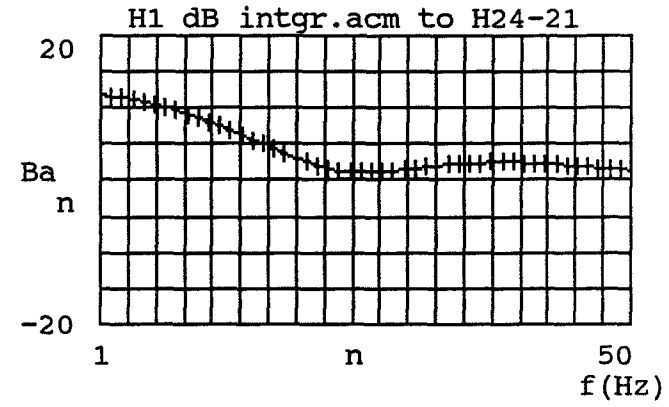

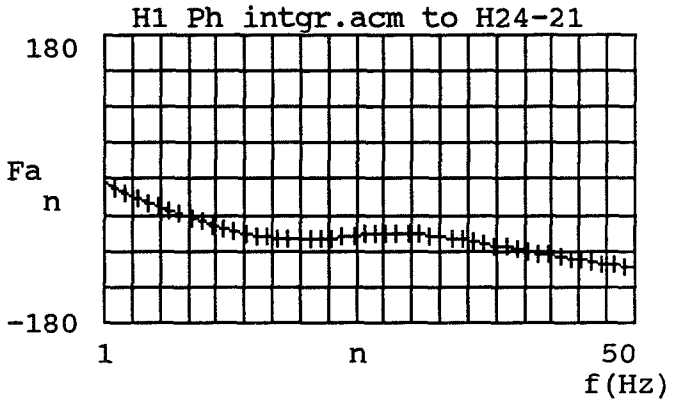

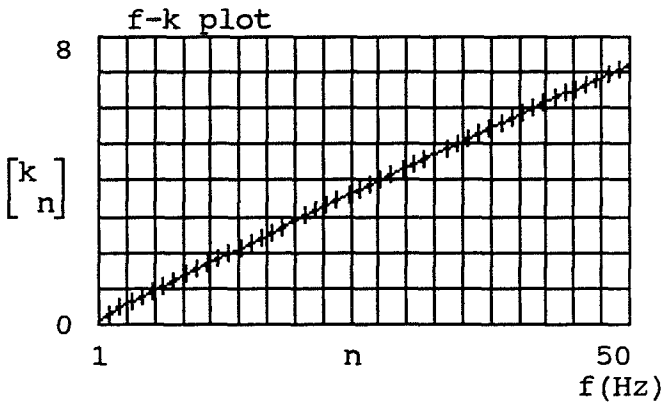

Appendix F1: Drawings for 12 Meter Experimental Section

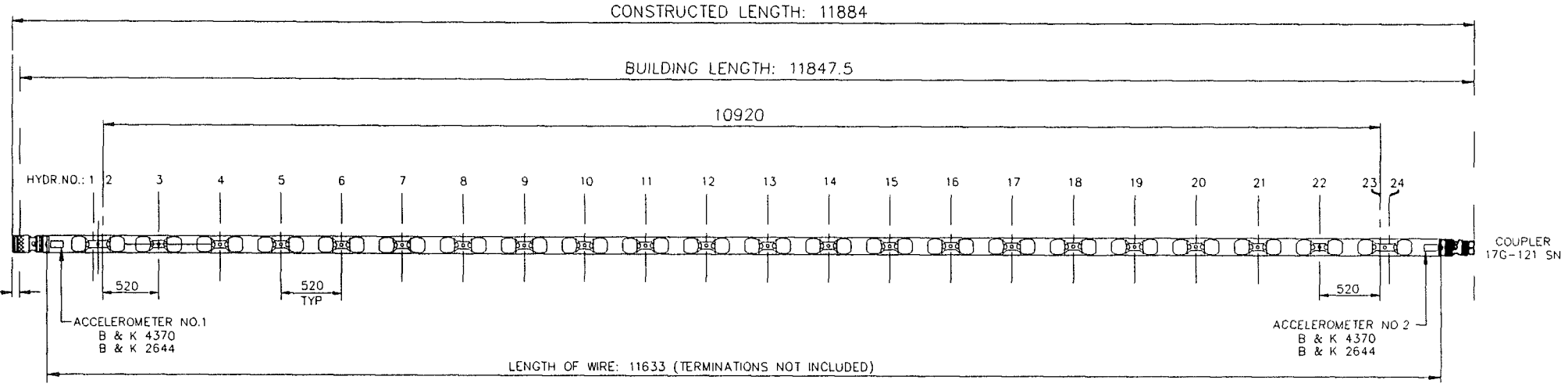

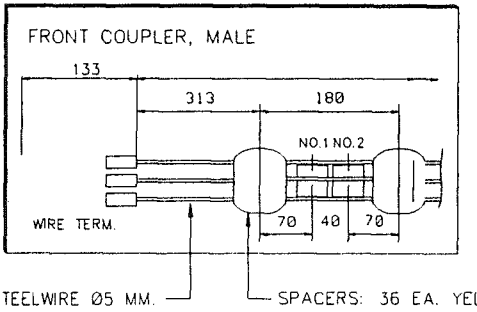

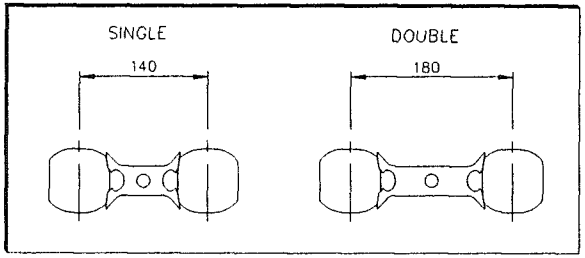

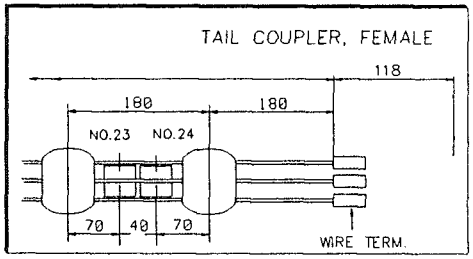

Rev	Date.	Reason for issue	ECO	Drn	Chk	Appr
P1	150193	AS BUILT		E.K	OAS	C.B

SCALE: NA

GENERAL TOLERANCE: NA

UNITS: mm

MATERIAL: NA

FORMAT: A3

Drwg title: 12m EXP. ACTIVE SECTION

Part no.

Ref. drwg. FI-1/2 375

Part list

Replacing

Schlumberger GECO-PRAKLA
Fjord Instruments A/S

Drwg.no. FI-113-62

Rev. P1

Sheet 1 of 1

Project ID:

121 PN Front connector

Function	Pins +	Pins -	Colour code +	Colour code -
HYDROPHONE NO.1	19	21	WH-BL, YE JAC.	
HYDROPHONE NO.2	64	88	RE-GN, GN JAC.	
HYDROPHONE NO.3	20	39	BR-BL	
HYDROPHONE NO.4	87	-105	YE-BL	
HYDROPHONE NO.5	38	63	GN-BL	
HYDROPHONE NO.6	86	-104	GY-BL	
HYDROPHONE NO.7	37	62	OR-BL	
HYDROPHONE NO.8	103	-115	RE-BL	
HYDROPHONE NO.9	102	-114	PI-BL	
HYDROPHONE NO.10	60	84	BR-BL	
HYDROPHONE NO.11	83	-101	YE-BL	
HYDROPHONE NO.12	36	59	GN-BL	
HYDROPHONE NO.13	58	82	GY-BL	
HYDROPHONE NO.14	18	35	OR-BL	
HYDROPHONE NO.15	34	57	RE-BL	
HYDROPHONE NO.16	6	17	PI-BL	
HYDROPHONE NO.17	76	97	BR-BL	
HYDROPHONE NO.18	96	-111	YE-BL	
HYDROPHONE NO.19	95	-110	GN-BL	
HYDROPHONE NO.20	13	28	GY-BL	
HYDROPHONE NO.21	48	73	OR-BL	
HYDROPHONE NO.22	72	94	RE-BL	
HYDROPHONE NO.23	93	-109	PI-BL	
HYDROPHONE NO.24	46	71	VI-BL	
	NOT CONNECTED		WH-BL	
	NOT CONNECTED		YE-BR	
	NOT CONNECTED		BK-BL	
GND. HYDR.1-24	1			
	4		NOT CONNECTED	
ACCELEROMETER NO.1	92	-108	YE-BR	
ACCELEROMETER NO.2	45	70	GN-BR	
CHASSIS GROUND	40	65		
	NOT CONNECTED		BR-BL	
	NOT CONNECTED		YE-BL	
	NOT CONNECTED		GN-BL	
	NOT CONNECTED		GY-BL	
	NOT CONNECTED		OR-BL	
	NOT CONNECTED		RE-BL	
	NOT CONNECTED		PI-BL	
	NOT CONNECTED		VI-BL	
	NOT CONNECTED		WH-BL	
	NOT CONNECTED		BK-BL	
	NOT CONNECTED		GY-BR	
	NOT CONNECTED		OR-BR	
	NOT CONNECTED		RE-BR	
	NOT CONNECTED		PI-BR	
	NOT CONNECTED		VI-BR	
	NOT CONNECTED		WH-BR	
	NOT CONNECTED		BK-BR	
	NOT CONNECTED		GN-YE	
	NOT CONNECTED		GY-YE	
	NOT CONNECTED		OR-YE	
	NOT CONNECTED		RE-YE	
	NOT CONNECTED		PI-YE	
	NOT CONNECTED		RE+BK BL JAC.	
	NOT CONNECTED			
	NOT CONNECTED			
	NOT CONNECTED			
	NOT CONNECTED			
	NOT CONNECTED			

JACKET: ORANGE JAC. (H1–H8), BLACK JACKET (H9–H16), BLUE JACKET (H17–H24)

121 PN Tail connector (NOT CONNECTED)

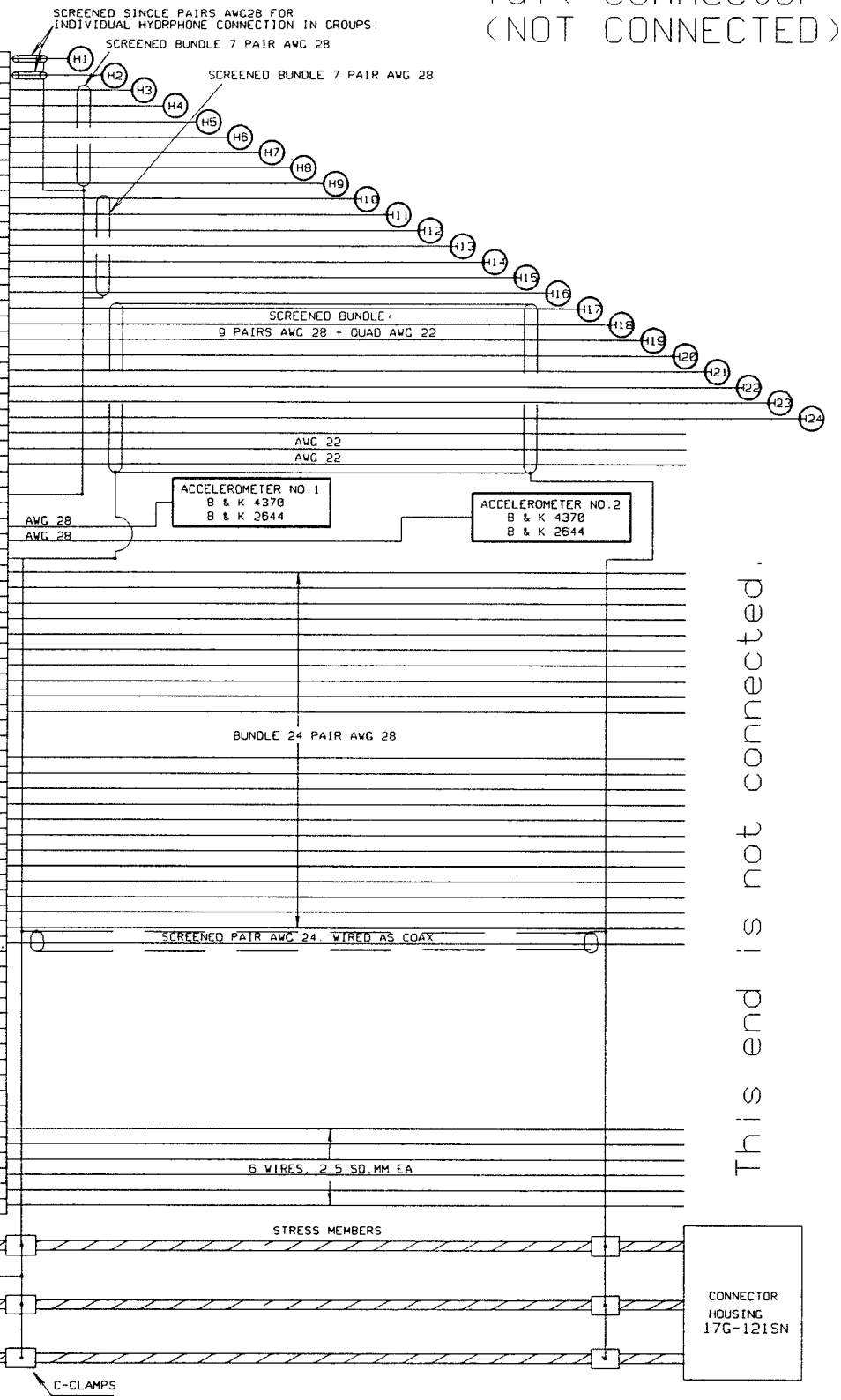

This end is not connected.

BK-BLACK
BL-BLUE
BR-BROWN
GN-GREEN
GY-GREY
OR-ORANGE
PI-PINK
RE-RED
VI-VIOLET
WH-WHITE
YE-YELLOW

NOTE:
* CAL.LINE BOTH CONDUCTORS WIRED TO PIN 16. SCREEN TO CH.GND. 40-65
** ONE SINGLE PAIR AWG 22

ev	Date	Reason for issue	ECO	Drn	Chk	Appr
1	150193	AS BUILT		E.K	OAS	C.B

SCALE: NA
GENERAL TOLERANCE: NA
UNITS:
MATERIAL: NA
FORMAT: A4

Drwg title: WIRING DIAGRAM FOR 12 m EXP.ACTIVE SECTION

Part no.
Ref. drwg. FI-113-62
Part list
Replacing

Schlumberger GECO-PRAKLA
Fjord Instruments A/S

Drwg.no. FI-1/2 375
Rev. P1
Sheet 1 of 1
Project ID:

OPEN END

121 SN

Tail connector

Colour code + −	Pins +	−	Function
BR-BL	19	21	HYDROPHONE NO.1
YE-BL	64	88	HYDROPHONE NO.2
GN-BL	20	39	HYDROPHONE NO.3
GY-BL	87	105	HYDROPHONE NO.4
OR-BL	38	63	HYDROPHONE NO.5
RE-BL	86	104	HYDROPHONE NO.6
PI-BL	37	62	HYDROPHONE NO.7
VI-BL	103	115	HYDROPHONE NO.8
WH-BL	102	114	HYDROPHONE NO.9
GN-BL	60	84	HYDROPHONE NO.10
YE-BR	83	101	HYDROPHONE NO.11
GN-BR	36	59	HYDROPHONE NO.12
GY-BR	58	82	HYDROPHONE NO.13
OR-BR	18	35	HYDROPHONE NO.14
RE-BR	34	57	HYDROPHONE NO.15
PI-BR	6	17	HYDROPHONE NO.16
VI-BR	76	97	HYDROPHONE NO.17
WH-BR	96	111	HYDROPHONE NO.18
BK-YE	95	110	HYDROPHONE NO.19
GN-YE	13	28	HYDROPHONE NO.20
GY-YE	48	73	HYDROPHONE NO.21
OR-YE	72	94	HYDROPHONE NO.22
RE-YE	93	109	HYDROPHONE NO.23
RE-YE	46	71	HYDROPHONE NO.24
BK-BR	92	108	ACCELEROMETER NO.1
PI-YE	45	70	ACCELEROMETER NO.2

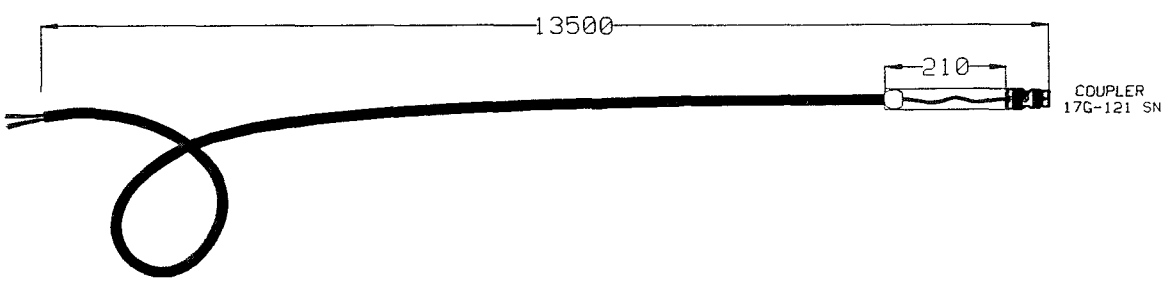

BK-BLACK
BL-BLUE
BR-BROWN
GN-GREEN
GY-GREY
OR-ORANGE
PI-PINK
RE-RED
VI-VIOLET
WH-WHITE
YE-YELLOW

Rev	Date.	Reason for issue	ECO	Drn	Chk	Appr
P1	150193	AS BUILT		E.K	OAS	C.B

SCALE: NA

GENERAL TOLERANCE: NA

MATERIAL:

UNITS:

FORMAT: A4

Drwg title:
WIRING DIAGRAM LEAD-IN
(FOR EXP. ACTIVE SECTION)

Part no. | Ref. drwg.

Part list | Replacing

Schlumberger GECO-PRAKLA
Fjord Instruments A/S

Drwg.no. FI-1/2 376

Rev. P1

Sheet 1 of 1

Project ID:

Appendix F2: Pictures from Experiments with 12 Meter Section

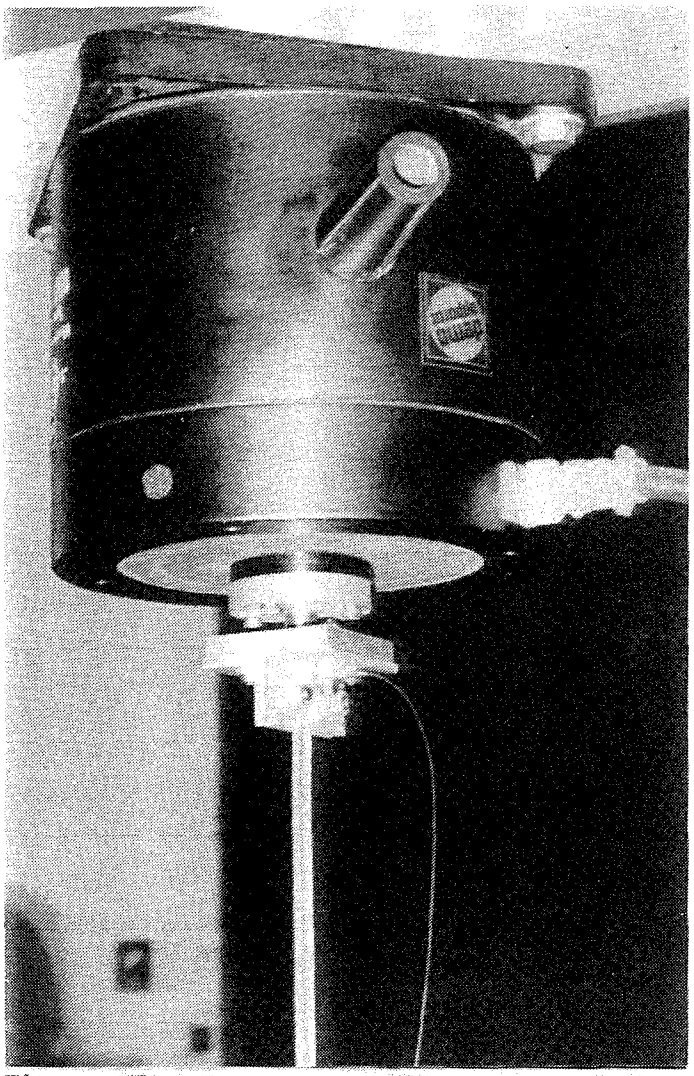

Picture F1 Measurement of Young's modulus. Segment of tube wall hanging from vibrator.

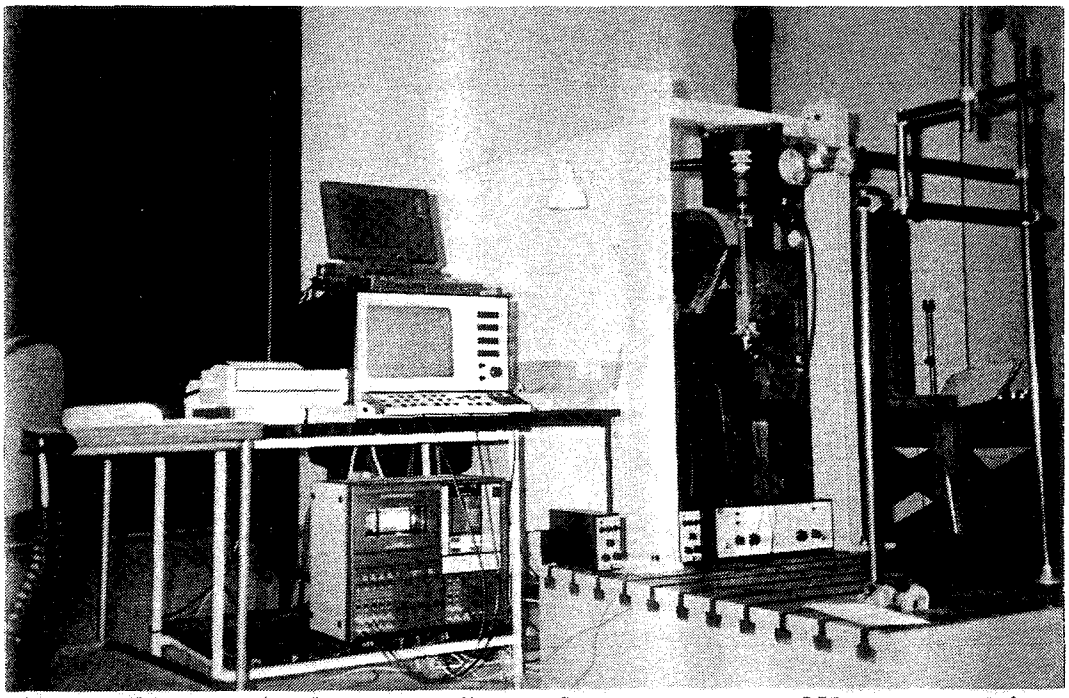

Picture F2 Setup with frame and vibrator for measurement of Young's modulus.

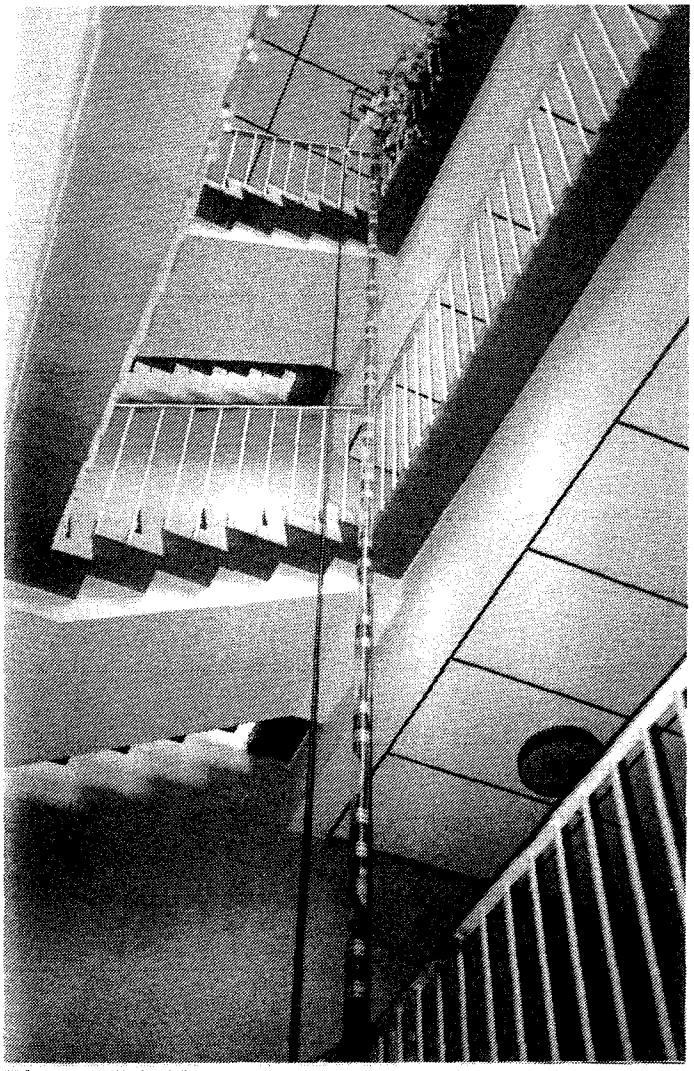

Picture F3 12 meter streamer section hanging from 4. floor in stairways at DTH.

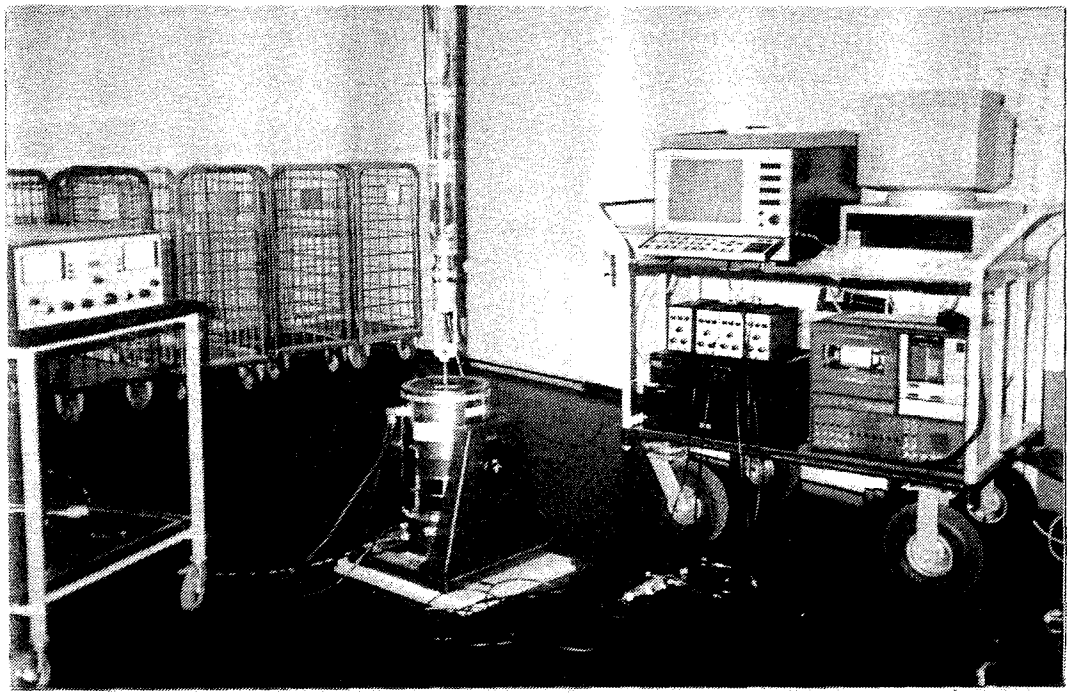

Picture F4 Connection to vibrator in basement.

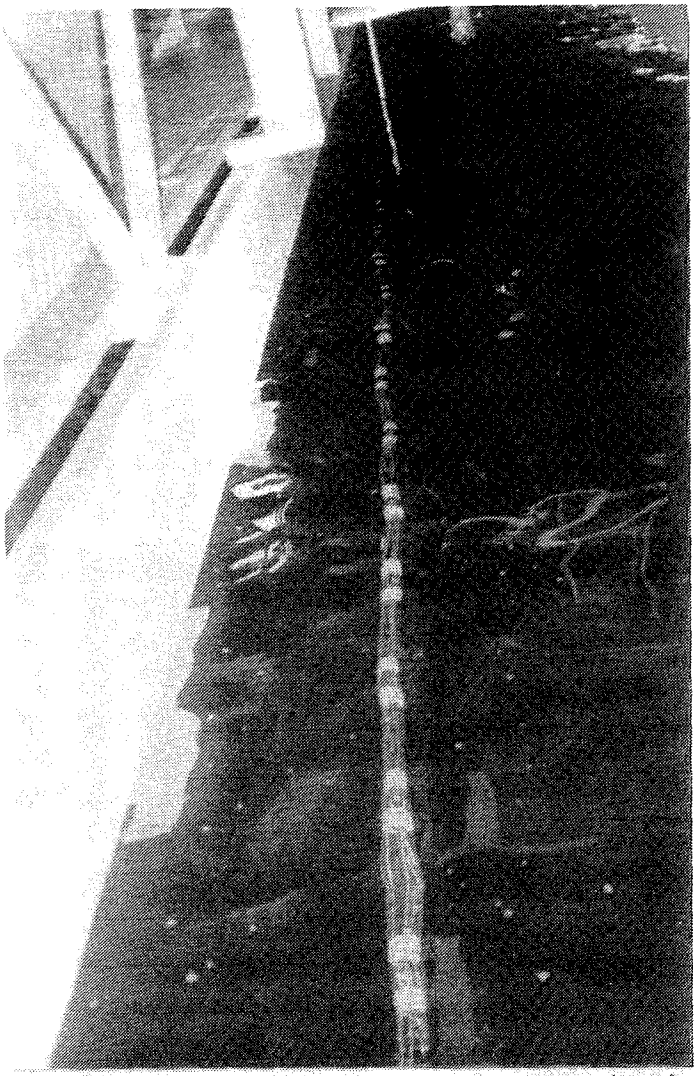

Picture F5 Towing 12 meter streamer section in water tank at the Shiplaboratory DMI.

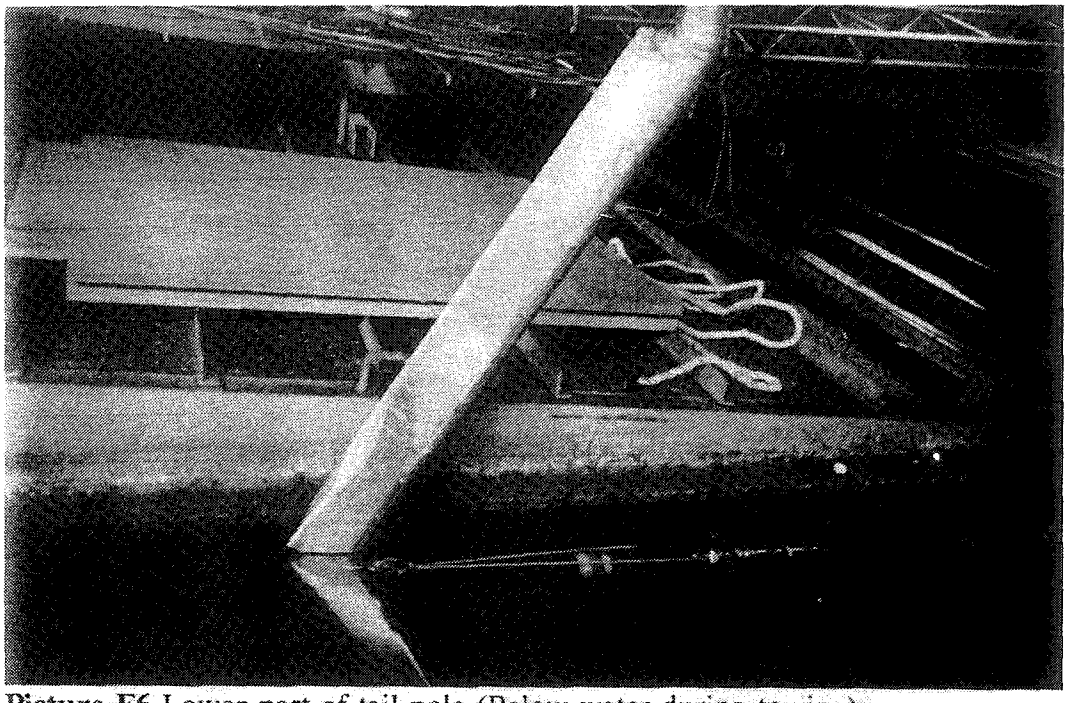

Picture F6 Lower part of tail pole (Below water during towing).

Appendix F3: Auto Spectrum PSD

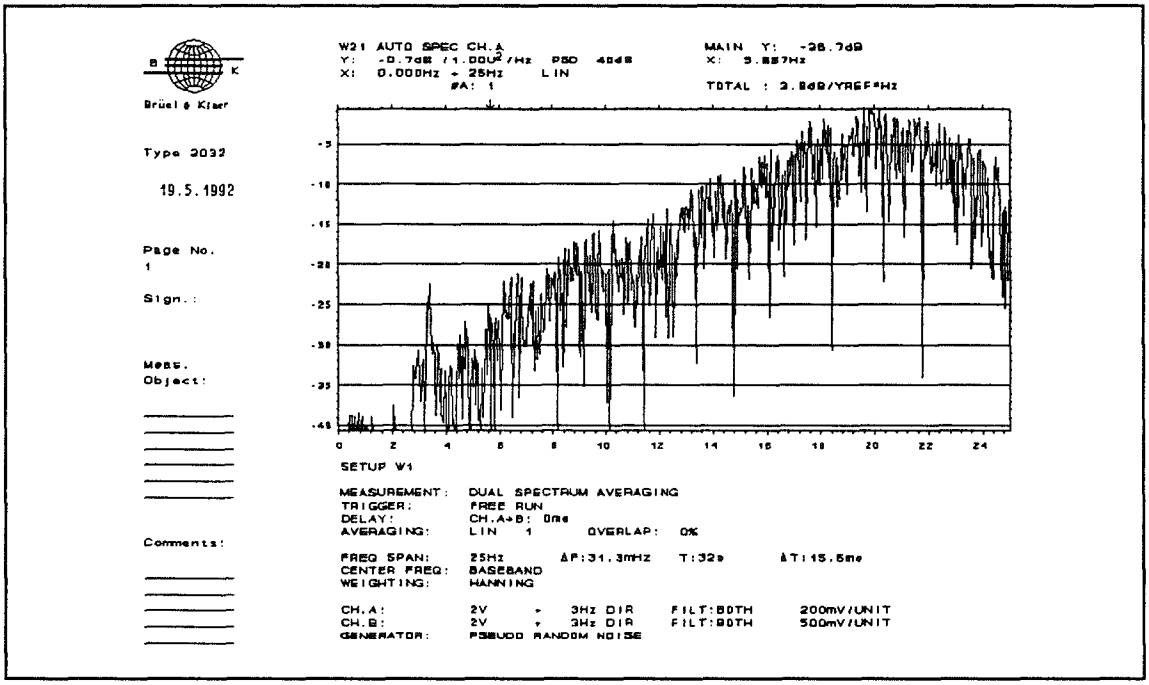

Figure 1 Auto Spectrum PSD Accelerometer on connector at vibrator piston

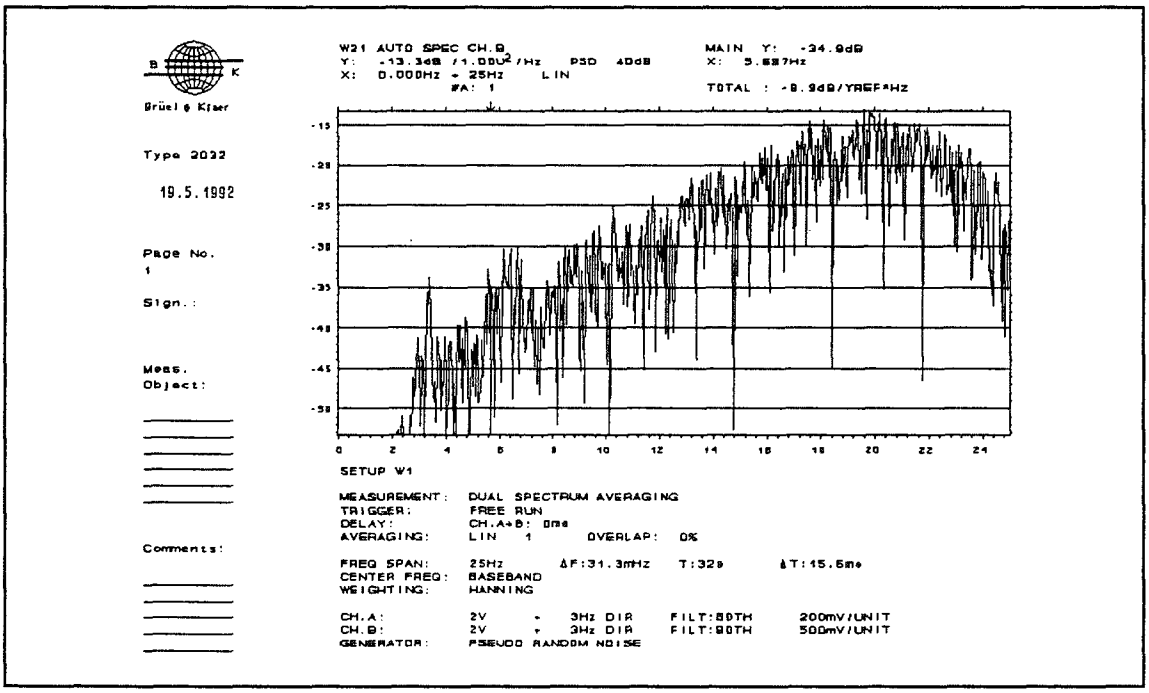

Figure 2 Auto Spectrum PSD Hydrophone H21

Appendix F4: Coherence

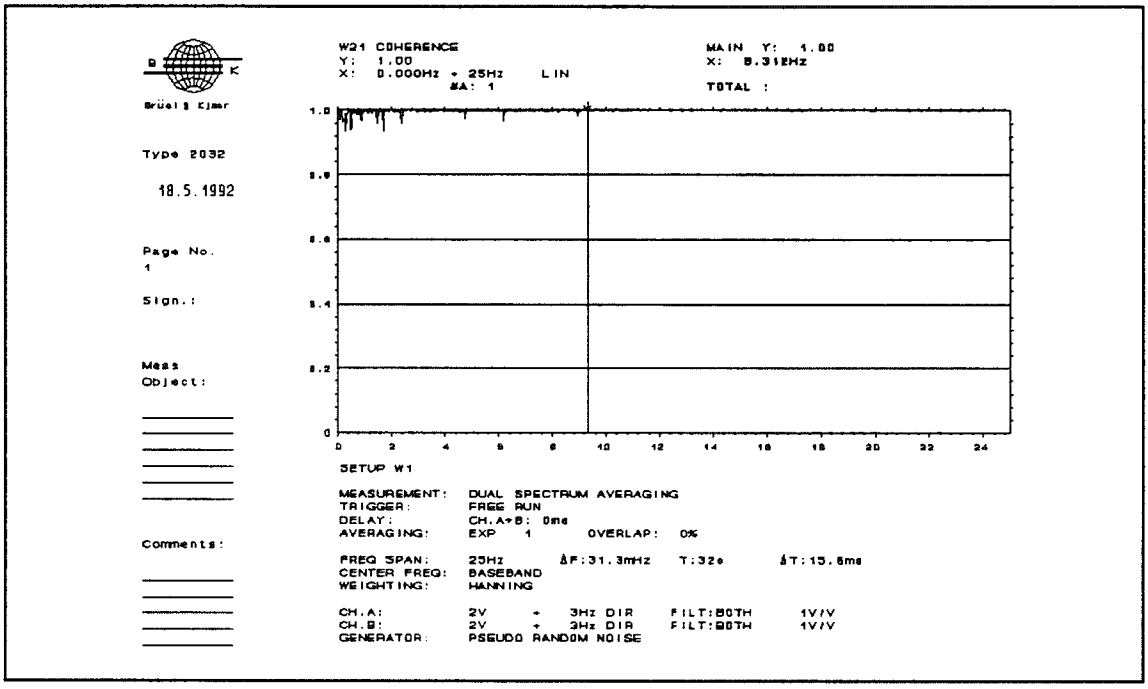

Figure 1 Coherence between Accelerometer and Hydrophone H21.

Appendix H1: Signal to Noise and Distortion for Adaptive Processor

Periodic or stationary random signals can be described in terms of correlation functions. The functions are defined for single-input linear combiner:

$$\textit{Cross-correlation: } \phi_{xy}(n) = E[x_k y_{k+n}] , \quad -\infty < n < \infty \tag{1}$$

$$\textit{Autocorrelation: } \phi_{xx}(n) = E[x_k x_{k+n}] , \quad -\infty < n < \infty \tag{2}$$

The discrete power spectrum is defined as the z-transform:

$$\textit{Cross-power spectrum: } \Phi_{xy} = \sum_{n=-\infty}^{\infty} \phi_{xy}(n) z^{-n} \tag{3}$$

$$\textit{Auto-power spectrum: } \Phi_{xx} = \sum_{n=-\infty}^{\infty} \phi_{xx}(n) z^{-n} \tag{4}$$

The power spectrum in terms of frequency, is obtained if z is replaced with $z=e^{j\omega}$. This is essentially the discrete Fourier transform.

Supposing $[y_k]$ and $[x_k]$ is related through a linear transfer function H(z)

If x,y and d are stationary signals and Y(z)=H(z)X(z) we have the following relations:

$$\Phi_{yx}(z) = \Phi_{xy}(z^{-1}) \tag{5}$$

where z^{-1} is the conjugate of z

$$\Phi_{xy}(z) = H(z)\Phi_{xx}(z) \tag{6}$$

$$\Phi_{dy}(z) = H(z)\,\Phi_{dx}(z) \tag{7}$$

$$\Phi_{yy}(z) = |H(z)|^2\,\Phi_{dx}(z) \tag{8}$$

The spectrum of the input to the adaptive filter in fig.8.3 is:

$$\Phi_{xx}(z) = \Phi_{ss}(z)\,|J(z)|^2 + \Phi_{nn}(z)\,|H(z)|^2 \tag{9}$$

The cross spectrum between the input x_k and desired responce d_k is:

$$\Phi_{xd}(z) = \Phi_{ss}(z)\,J(z^{-1}) + \Phi_{nn}(z)\,H(z^{-1}) \tag{10}$$

The Wiener transfer function for the adaptive filter is:

$$W^*(z) = \frac{\Phi_{xd}(z)}{\Phi_{xx}(z)} \tag{11}$$

The spectrum of the signal component in the output:

$$\Phi_{ss_{out}}(z) = \Phi_{ss}(z)\,|1 - J(z)W^*(z)|^2 = \Phi_{ss}(z)\left|\frac{[H(z) - J(z)]\,\Phi_{nn}(z)H(z^{-1})}{\Phi_{ss}(z)\,|J(z)|^2 + \Phi_{nn}(z)\,|H(z)|^2}\right|^2 \tag{12}$$

The spectrum of the noise component in the output:

$$\Phi_{nn_{out}}(z) = \Phi_{nn}(z)\,|1 - H(z)W^*(z)|^2 = \Phi_{nn}(z)\left|\frac{[J(z) - H(z)]\,\Phi_{ss}(z)J(z^{-1})}{\Phi_{ss}(z)\,|J(z)|^2 + \Phi_{nn}(z)\,|H(z)|^2}\right|^2 \tag{13}$$

The output signal to noise density ratio is:

$$\rho_{out}(z) = \frac{\Phi_{nn}(z)\,|H(z)|^2}{\Phi_{ss}(z)\,|J(z)|^2} \tag{14}$$

The signal to noise density ratio at the reference can be seen from fig.8.3 to be:

$$\rho_{ref}(z) = \frac{\Phi_{ss}(z)\,|J(z)|^2}{\Phi_{nn}(z)\,|H(z)|^2} \tag{15}$$

The output signal to noise density ratio is then:

$$\rho_{out}(z) = \frac{1}{\rho_{ref}(z)} \tag{16}$$

Under the assumtions: unconstrained adaptive solution, and noise in the primary and the reference input are mutually correlated.

The signal to noise density ratio at the output of the noise canceller is simply the resiprocal of the signal to noise density ratio at the reference input for all frequencies. **This is called power inversion.**

Signal distortion at the output of the noise canceller

When some signal component is present in the reference signal distortion will occur. The transfer function trough the filter is (ref fig.8.3) when |J(z)| is small:

$$-J(z)W^*(z) \approx \frac{J(z)}{H(z)} \tag{17}$$

The spectrum of the signal component trough the filter is:

$$\Phi_{ss_{dist}}(z) \approx \Phi_{ss}(z)\left|\frac{J(z)}{H(z)}\right|^2 \tag{18}$$

The signal distortion is defined as a dimensionless ratio:

$$D(z) \approx \frac{\Phi_{ss_{dist}}(z)}{\Phi_{ss}(z)} \approx \left|\frac{J(z)}{H(z)}\right|^2 \tag{19}$$

The signal to noise density ratio at the primary input is defined:

$$\rho_{pri}(z) \triangleq \frac{\Phi_{ss}(z)}{\Phi_{nn}(z)} \tag{20}$$

Using the equation for signal to noise density at the reference input:

$$D(z) \approx \frac{\rho_{ref}(z)}{\rho_{pri}(z)} \tag{21}$$

This result shows that signal distortion is low for high signal to noise ratio at the primary and low signal to noise ratio at the reference input.

The spectrum of the output noise:

The noise n_k propagates to the output with a transfer function when $|J(z)|$ is small compared to $|H(z)|$:

$$1-H(z)W^*(z) \approx \frac{-\Phi_{ss}(z)J(z^{-1})}{\Phi_{nn}(z)H(z^{-1})} \tag{22}$$

The output noise from fig.8.3

$$\Phi_{output\ noise} \approx \Phi_{nn}(z)|1-H(z)W^*(z)|^2 \tag{23}$$

This gives in terms of signal to noise ratio at the reference input:

$$\Phi_{output\ noise} \approx \Phi_{nn}(z)|\rho_{ref}(z)|\,|\rho_{pri}(z)| \tag{24}$$

This result shows that the output noise spectrum is proportional to the input noise spectrum. The second factor indicates low output noise spectrum for low signal to noise at the reference. The last factor shows that low signal level on the primary gives the best result.

The above results shows that the adaptive noise cancelling system can still work with a small signal component in the reference input.

Appendix I1: Program Listing

```
/*********************************************************************/
/*    Adaptive Processor                                             */
/*    Rev. date:2/6, 1992, C. Bjelland. (ref:Filt-X, P.Christiansen)*/
/*    A : Reference Signal                                           */
/*    B : Input Signal                                               */
/*                                                                   */
/*********************************************************************/
/*  inkluderet :
      sampling.c
      intbeh.asm
      filxlea3.asm
      algoritmer.lms
      libap.h  */
int      ttest;
int     aendring;
int     maxout;
float   maxtal;  /* udgangsstyrke af støjsignal til initialsering */
float   alfafaktor,alfa,ny_x;
int     samp_frek = 200;
float   maxtal2; /* udgangsstyrke af støjsignal under drift */
float   dummy1;
float   dumfak = 1;
float   dumfak2 = 1;
float   gemfrasidst;
int     algoritme;
int     minuslyd=0;
int      findH;
int     status;
int     antal_koeff; /*  antal koefficienter i ht estimat filter  */
/*** variable til lms-algoriter  ***/
float phi,gamma,my;
int     nopause;
/*   variable til fejlregistrering   */
#define maxantal_maalinger 1010
int     antal_maalinger = 1;      /*  hvor mange fejl der taelles op i hver fejlicyklus  */
float   fejlicyklus[maxantal_maalinger];
int     cyklustaeller;
int     cyklus;
float   *ptr;
```

```
#define max_ant_koeff 1010       /* max ca 1800 med dspmap */
float   a_est[max_ant_koeff];
float normfaktor_1 = 3.0 / 32767.0;
float normfaktor = 32767.0 / 3.0;

float   hydrofon=0.0;
short   inA, inB, outA, fyld, outB;
float   fejl;
int     ii;
int     intbetjent;
int     anc;
/**** VARIABLE TIL FIR-FILTER ****/
float   ys;
float   z,u;
float   x[ max_ant_koeff ];
float   faktor;
float   nyfilt_x;
/*** variable til 2. fir filter  ****/
float   beta = 1.0,alfa2,sigma = 1.0;
float FIRkoeff[max_ant_koeff];
float accsignal[ max_ant_koeff ];
float accelerometer;

short palle=8000;
int ib;
/***********/
#define canA 0x200000
#define canB 0x200004

#include <inclu.pc>
#include <sampling.c>
#include "intbeh.asm"
#include "filxlea3.asm"
#include "algoritmer.lms"
#include <libap.h>
```

```
/*********************************************************************/
/************************ INTERRUPT ********************************/
/*********************************************************************/

void interrupt()
{
asm(".global interrupt2");
asm("interrupt2:");

gemregistre();

int2off();

/*  Get measurements from A/D Converter */
inA = get_mem16(canA);   /*   A: Reference Signal (accelerometer)    */
inB = get_mem16(canB);   /*   B: Signal (desired signal + noise )  */

/*  konvertering 1.00 = 1 V.  */
hydrofon = ( ( float ) inA ) * normfaktor_1 * dumfak2 ;
accelerometer = ( ( float ) inB ) * normfaktor_1 * dumfak ;

intbetjent = 1;  /* sættes for at vise at interruptet er betjent */

hentregistre();
asm(" ireturn ");
}

/*********************************************************************/
/********************* INTERRUPT SLUT*********************************/
/*********************************************************************/
```

```
/*** initialising FIR filter ***/

void initFIR()
{

initpcw();
set_samp_frek(samp_frek);

/* nulstilling af indgangssignal og FIR filter koefficienter for ht_est */
for ( ii = 0; ii < antal_koeff; ii++ ) { x[ii] = 0.0;FIRkoeff[ii] = 0.0;}

sigma = 1.0;
alfa2 = alfafaktor / antal_koeff;
intbetjent = 1;
}

void initfilter()
{
set_samp_frek();
cyklustaeller=0;cyklus=0;
for (ii=0;ii<maxantal_maalinger;ii++)
  {fejlicyklus[ii]=0;};
nopause = 1;
for (ii=0;ii<antal_koeff;ii++)
  {x[ii]=0;FIRkoeff[ii]=0;accsignal[ii]=0;};
alfa2 = alfafaktor / antal_koeff;
intbetjent = 0;
}
```

```
/*************************************************************************/
/*************************************************************************/
/******   MAIN() ******/
main()
{

algoritme = 2;
antal_koeff = 1000;
outB = 8000;
gemfrasidst = 0.999980;
alfafaktor = 0.005;
maxout = 12000;

/* initFIR();*/

initpcw();
accelerometer = 0;
set_samp_frek(samp_frek);
for ( ii = 0; ii < antal_koeff; ii++ )
  {
  x[ ii ] = 0.0;
  }
sigma = 1.0;
alfa2 = alfafaktor / antal_koeff;
intbetjent = 0;
minuslyd = 0; status = 1; findH = 0;
aendring = 0;
int2on();
status=0;
goto igen;

        /*   filter beregninger     */
filter:  /* indgangsfiltrering ( highpass ) */
```

```
/* TRANSVERSAL FIR-FILTER MED LEAST MEAN SQUARE ALGORITME */

firogopdat(antal_koeff,accelerometer,u,FIRkoeff,accsignal);

/*************** Udregning af fejl. ******************/
fejl = hydrofon-u;

sigma = ( 1.0 - alfa2 ) * sigma + accelerometer * accelerometer;
beta = 1.0 / sigma;

/******** Opdatering af filterkoefficienter. **********/

faktor = beta*fejl;    /* beta * fejl;  */
opdatkoeff(antal_koeff,faktor,FIRkoeff,accsignal);

/************* Udskrivning på kanal A og B. ************************/
outA = fejl * normfaktor;
if ( outA > maxout ) outA = maxout;
if ( outA < - maxout ) outA = - maxout;
palle = -palle;
outB = inA-4000;    /*fejl * normfaktor; ---------------------------------*/
filterslut:

/********   udregning af fejl pr cyklus   **************/
  fejlicyklus[cyklus] = fejlicyklus[cyklus] + fejl * fejl;
    if ( ++cyklustaeller == antal_maalinger )
      {
        cyklus++;
        cyklustaeller = 0;
        if (cyklus > maxantal_maalinger) {cyklus = maxantal_maalinger;};
      }
/*********************************************************/
/*  gem resultat til d/a */
put_mem16(canA, outA);
put_mem16(canB, outB);
int2on();

/*    filterberegninger slut   */

igen:

ttest++;
```

```
            /*    VENTER BARE PÅ ET INTERRUPT */
if ( intbetjent == 1 ) { intbetjent =0; goto filter; }
if ( aendring == 1 )
   {
   int2off();
   switch (status)
      {
      case 0: initFIR();break;
      case 2: initfilter();break;
      }
   aendring = 0;
   int2on();
   }
if ( aendring == 2)
   {
   switch (status)
      {
      case 0: /* færdig med at finde FIRkoeff */
                minuslyd = 1; status = 1; findH = 0; break;
      case 1: /* færdig med at køre stille */
                minuslyd = 0; initfilter(); status = 2; break;
      case 2: /* skal til at estimere ht igen */
                status = 0; initFIR(); break;
      }
   aendring = 0;
   int2on();
   }
if (aendring == 3)
   {
   switch (nopause)
      {
      case 0: /* der er nu pause og ønskes aktivitet */
            nopause = 1;break;
      case 1: nopause =0;break;
      }
   aendring = 0;
   }

goto igen;
}
```

```
/*            FILTCBEN.C          rev.8/7-92CB          */
/*************************************************************/
/*   The program can read and change parameters              */
/*   while running adaptive filter on the dsp board          */
/*   ref cato.c                                              */
/*************************************************************/
#include <stdio.h>
#include <conio.h>
#include <stdlib.h>
#include "dsp32.h"

#define FALSE 0
#define       TRUE 1

  FILE    *udfil;
  char filnavn[50];*ptr1;
  unsigned long ii;
  float    koefficient,tal;
  short    tast,tryk_tast;
  int      dum;
  unsigned short  board = 0x290;
  int    antal_koeff;
  int    maxout,sampfrek,status;
  float  maxouttest,maxtal2,fejlsum;
  float  alfafaktor,alfa2;
  float dumfak,dumfak2;
  int algoritme,antal_maalinger;
  unsigned long databaseseg = 0x8006b0;

main()
{
   dum=WarmSelect(board);
```

```
forfra:
   antal_koeff = GetInt24(databaseseg + 0x48);
   maxout      = GetInt24(databaseseg + 0xc);
   alfafaktor  = GetFloat(databaseseg + 0x14);
   sampfrek    = GetInt24(databaseseg + 0x20);
   status      = GetInt24(databaseseg + 0x44);
   maxtal2     = GetFloat(databaseseg + 0x24);
   antal_maalinger = GetInt24(databaseseg + 0x5c);
   alfa2 = GetFloat(databaseseg + 0x3004);
   dumfak  = GetFloat(databaseseg + 0x2c);
   dumfak2  = GetFloat(databaseseg + 0x30);
   algoritme = GetInt24(databaseseg + 0x38);
   printf("\n1. Change number of koeff. in FILTER, nu %d   ",
                                      antal_koeff );
   printf("\n2. Change dumfak %10.10f   ",dumfak);
   printf("\n3. Change sampling-frequency,nu %d   ",sampfrek);
   printf("\n4. Change alfafaktor %10.10f   ",alfafaktor);
   printf("\n7. Change dumfak2 %10.10f   ",dumfak2); */
   printf("\n9. Change alfa2 %10.10f   ",alfa2);
   printf("\na. Change algorithm# nu nr: %d",algoritme);
   printf("\np. PAUSE ON/OFF");
   printf("\nH. Get firfilter coefficients");
   printf("\nM. Change number of measurements in each sum. nu :%d",
                                   antal_maalinger);
   printf("\nU. Write error-sum to file");
   printf("\n0. reset, new start");
   if (status==0) printf("\n*** Initialiserer ht_estimat ***");
   if (status==1) printf("\n**** sover *****");
   if (status==2) printf("\n**** anc tilsluttet *****");
   printf("\nTRYK Q FOR Quit. " );

   tryk_tast = FALSE;

   do
     {
  tast = getch();
  switch( tast )
      {
```

```
case 'U':
   printf("Writing Error-sum");
 nytfejlfilnavn:
   printf("\nFile name for Error-sum ?");
   scanf("%s",filnavn);
   strcat(filnavn,".dat");
   udfil = fopen(filnavn,"wt");
   if (udfil == NULL) {printf("Fejl ved åbning af :%s",
                      filnavn) ; goto nytfejlfilnavn;}
   printf("Error-sum written to %s",filnavn);
{
for (ii=0;ii<200;ii++)
   {
   fejlsum=GetFloat(ii*4+databaseseg+0x60);
   tal=(float) antal_maalinger * ii;
   fprintf(udfil,"%8.0f ",tal);
   fprintf(udfil,"%f\n",fejlsum);
   }
}
   fclose(udfil);
 tryk_tast=TRUE;
 break;
case 'H':
   printf("Get filterkoefficients");
 nytfilnavn:
   printf("\nFilname for FIR-FILTER koefficients ?");
   scanf("%s",filnavn);
   strcat(filnavn,".dat");
   udfil = fopen(filnavn,"wt");
   if (udfil == NULL) {printf("Fejl ved åbning af :%s",
                           filnavn) ; goto nytfilnavn;}
   printf("coefficients written to %s",filnavn);
{
for (ii=0;ii<antal_koeff;ii++)
   {
   koefficient=GetFloat(ii*4+databaseseg+0x300c);
   fprintf(udfil,"%4d ",antal_koeff-ii);
   fprintf(udfil,"%f\n",koefficient);
   }
}
  fclose(udfil);
```

```
/*    nytfilnavn2:
     printf("\nFilnavn til Ht koefficenter ?");
       scanf("%s",filnavn);
       strcat(filnavn,".dat");
       udfil = fopen(filnavn,"wt");
       if (udfil == NULL) {printf("Fejl ved åbning af :%s",
                           filnavn) ; goto nytfilnavn;}
       printf("data gemmes i %s",filnavn);
       ptr1 = filnavn + strlen(filnavn)-4;
       strcpy(ptr1,".kof");
       udfil2= fopen(filnavn,"wt");*/

       tryk_tast= TRUE;
       break;

    case '1':
       printf("Number of coefficients:");
       dum = scanf("%hi",&antal_koeff);
       dum = PutInt16(databaseseg+0x48,antal_koeff);
       dum = PutInt16(databaseseg+0x4,1);
       tryk_tast = TRUE;
       break;

    case 'M':
       printf("Number of measurements in each sum:");
       dum = scanf("%hi",&antal_maalinger);
       dum = PutInt16(databaseseg+0x5c,antal_maalinger);
       dum = PutInt16(databaseseg+0x4,1);
       tryk_tast = TRUE;
       break;

    case '2':
       tryk_tast = TRUE;
       printf("dumfak :");
       dum = scanf("%hf",&dumfak);
       dum = PutFloat(databaseseg+0x2c,dumfak);
       break;
```

```
case '3':
   tryk_tast = TRUE;
   printf("Sampling frequency:");
   dum = scanf("%hi",&sampfrek);
   dum = PutInt16(databaseseg+0x20,sampfrek);
   dum = PutInt16(databaseseg+0x4,1);
   break;

case '4':
   tryk_tast = TRUE;
   printf("alfafaktor :");
   dum = scanf("%hf",&alfafaktor);
   dum = PutFloat(databaseseg+0x14,alfafaktor);
   break;

case '6':
   tryk_tast = TRUE;
   printf("maxout :");
   dum = scanf("%hi",&maxout);
   dum = PutInt16(databaseseg+0xc,maxout);
   break;

case 'a':
   tryk_tast = TRUE;
   printf("algoritme:");
   dum = scanf("%hi",&algoritme);
   dum = PutInt16(databaseseg+0x38,algoritme);
   break;

case '7':
   tryk_tast = TRUE;
   printf("dumfak2 :");
   dum = scanf("%hf",&dumfak2);
   dum = PutFloat(databaseseg+0x30,dumfak2);
   break;

case '9':
   tryk_tast = TRUE;
   printf("alfa2 :");
   dum = scanf("%hf",&alfa2);
   dum = PutFloat(databaseseg+0x304,alfa2);
   break;
```

```
  case '0':
    tryk_tast = TRUE;
    dum = PutInt16(databaseseg+0x4,1);
    break;

  case 's':
    tryk_tast = TRUE;
    dum = PutInt16(databaseseg+0x4,2);
    break;

  case 'p':
    tryk_tast = TRUE;
    dum = PutInt16(databaseseg+0x4,3);
    break;

  case 'q':
  case 'Q': goto slutslut;

      }
    } while( tryk_tast != TRUE );
  goto forfra;
slutslut: ;
}
```

Appendix J1: Measurements with New Accelerometer Unit

Online QC : TRACE-PLOT
SAPPHIRE E: 17:07:04 10 Jan 1993
Client/Job : CONOCO / 8320
Area/Line : BLK-48 / TEST
File : 314

Channels : SEIS,394
Time window: .000-5.000 sec
Filter out
No group summation
True amplitude

Schlumberger
GECO-PRAKLA

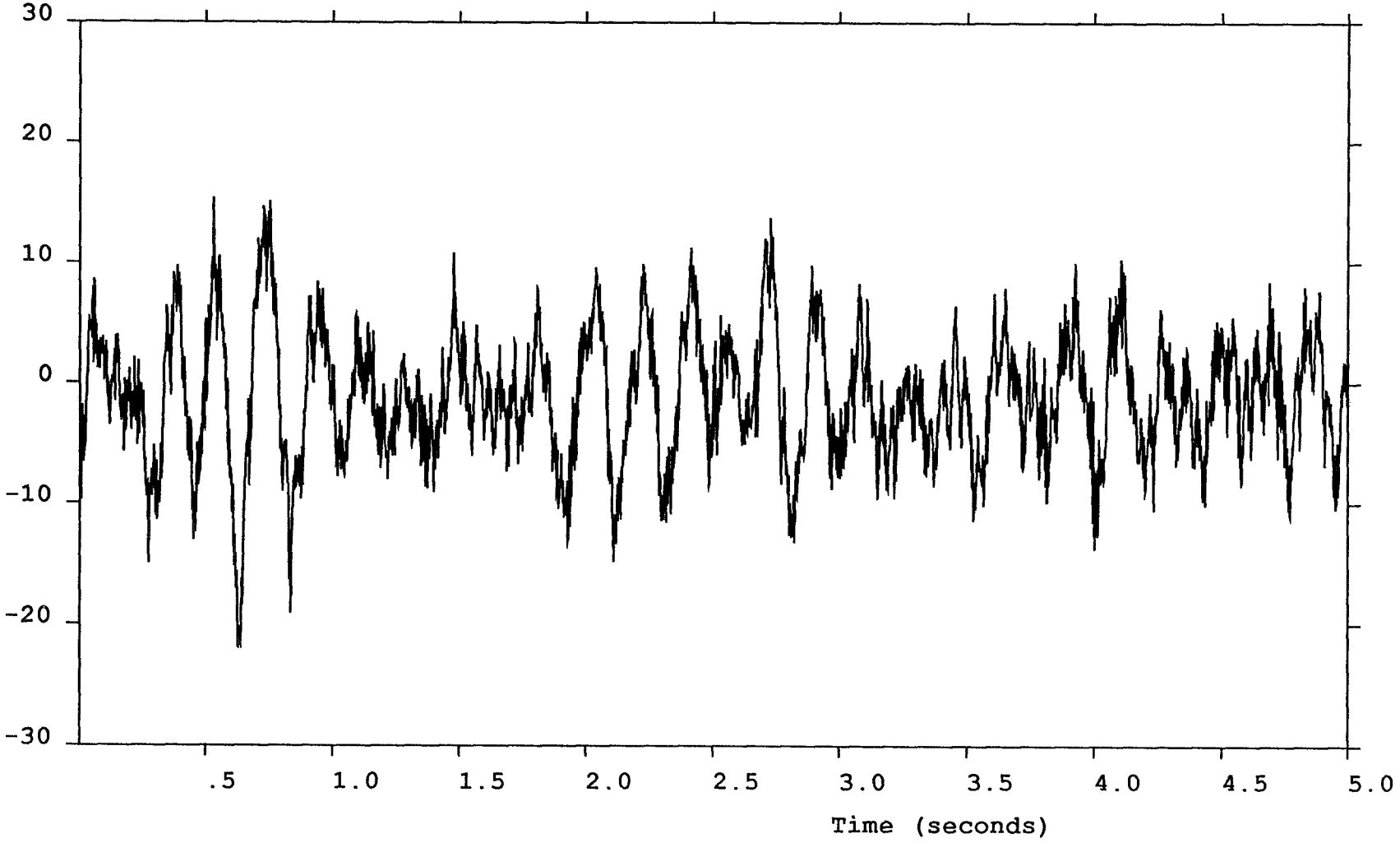

Online QC : TRACE-PLOT
SAPPHIRE E: 17:04:02 10 Jan 1993
Client/Job : CONOCO / 8320
Area/Line : BLK-48 / TEST
File : 314

Channels : SEIS,385
Time window: .000-5.000 sec
Filter out
No group summation
True amplitude

Schlumberger
GECO-PRAKLA